Rhythms and Wave Propagation in the Heart

DISSERTATION

zur Erlangung des akademischen Grades
doctor rerum naturalium
(dr. rer. nat.)
im Fach Physik

eingereicht an der
Mathematisch-Naturwissenschaftlichen Fakultät I
Humboldt-Universität zu Berlin

von
Herrn Dipl.-Phys. Christian Zemlin
geboren am 9.5.1972 in Hamburg

Präsident der Humboldt-Universität zu Berlin:
Prof. Dr. Mlynek

Dekan der Mathematisch-Naturwissenschaftlichen Fakultät I:
Prof. Dr. Bernhard Ronacher

Gutachter:

1. Prof. Dr. Hanspeter Herzel
2. Prof. Dr. Lutz Schimansky-Geier
3. Prof. Dr. Alexander Mikhailov

eingereicht am:	27. Februar 2002
Tag der mündlichen Prüfung:	26. Juni 2002

Abstract

In this thesis, we study heart rhythms at different levels, from single cells to the entire human atria. The main project of this thesis is the development of a realistic and efficient model of wave propagation in the human atria. We start by studying paced single cells and their loss of 1:1 rhythmicity for increasing frequency. We go on to study wave propagation in tissue with special electrophysiologic properties, related to chronical disease of the atria. Then we treat ionic models, which are a central part of our atrial model. We discuss a recently discovered mathematical degeneracy present in all models of cardiac cells that include intracellular ion concentrations and we explain why this degeneracy has only a negligible effect on wave propagation. We develop a method to reduce the complexity of ionic models while closely retaining their wave propagation properties. Then we apply this method to a realistic ionic model of the human atria and combine it with anatomical data to get the desired model. We use this model to explore possible mechanisms for the genesis of arrhythmias.

Keywords:
heart, arrhythmia, excitation, model

Zusammenfassung

In der vorliegenden Arbeit untersuchen wir verschiedene Aspekte von Herzrhythmen, von einzelnen Zellen bis zu den gesamten menschlichen Vorhöfen. Das Hauptprojekt ist die Entwicklung eines realistischen und effizienten Modells für die Erregungsausbreitung in den menschlichen Vorhöfen. Im ersten Kapitel untersuchen wir stimulierte Herzellen und den Verlust vom 1:1-Rhythmus für steigende Frequenzen. Weiter untersuchen wir Wellenausbreitung in Gewebe mit besonderen elektrophysiologischen Eigenschaften, die mit chronischen Erkrankungen der Vorhöfe in Verbindung stehen. Dann wenden wir uns Ionenmodellen zu, die ein zentraler Teil des Vorhofmodells sind. Wir untersuchen die Auswirkungen einer Verletzung der Ladungserhaltung, die in allen Ionenmodellen vorliegt, die die Konzentrationen der Ionen als Variablen enthalten, und erklären, warum diese Auswirkungen meist vernachlässigbar sind. Wir entwickeln weiter eine Methode, Ionenmodelle zu vereinfachen und dabei ihre für die Wellenausbreitung wichtigen Eigenschaften nur minimal zu verändern. Diese Methode wenden wir auf ein realistisches Ionenmodell für menschliches Vorhofgewebe an und kombinieren es mit anatomischen Daten, um das gewünschte realistische Vorhofmodell zu erhalten. Schließlich benutzen wir dieses Modell, um mögliche Mechanismen der Enstehung von Herzrhythmusstörungen zu untersuchen.

Schlagwörter:
Herz, Herzrhythmusstörungen, Modell, Erregung

Acknowledgments

Hanspeter Herzel and Sasha Panfilov are not only great supervisors but true friends, and I feel privileged to have worked with them for the past years. I hope and believe we will have many joint projects in the future.

The ITB is a wonderful institute with regard to how it is situated, but even more so with regard to the people working there and the spirit they create. I should mention so many people, but writing this the day before I leave Berlin, I can only thank a few: Jürgen, my long-time roommate for the friendly and open atmosphere in our room and the things we shared, Tim for deep discussions on everything from quantum mechanics to Schwarzenegger movies, and Arndt for the basketball, movies, and other things we did together. Nils for his everlasting good mood and his helpfulness and Branka her dynamic temperament, though she should have come more than three months before I leave. I profited deeply from the wide range of scientific opportunities at the ITB, like the winter and spring schools and the talks of countless guest, and also from the more social events like the ITB choir, the soccer games and our snowball fights.

Great thanks also to the Utrecht group for Theoretical Biology, my second home during my PhD time. Paulien Hogeweg made me feel as a welcome new member, and I met so many nice people that I cannot mention all of them here, either. The hospitality of my friends, Jelle, Stan, and then to an enormous extent Ilse, has been so abundant that I am not sure if I can ever return it to them, though I'll try to.

I am grateful that I had the chance to visit many other institutions during my PhD time. I spent a month in the group of Prof. Keener at the University of Salt Lake City, Utah (USA) and was impressed by their way of doing and discussing mathematical biology. In Ghent, Belgium I visited Oliver Bernus, also a PhD student of Sasha Panfilov, to whom I am also grateful for the many discussions we had. I was invited to the Amsterdam Medical Center

by Ronald Wilders, who also helped me at many points in my work. The heart modeling group in Karlsruhe with Frank Sachse and Gunnar Seeman also invited impressed me above all with their superb computer programs and facilities. In Freiburg I got some important help from the group around Prof. Dziuk working with finite elements on curved surfaces. Here in Berlin, I thank Ralf Mrowka from the Institute of Physiology of the Humboldt-University for enriching discussions. Johannes Schmidt-Ehrenberg helped me with visualization and his great programming skills.

Finally, I would like to thank my friends and my family, especially my brother Wolfgang, my sisters Eva and Johanna, and my parents. They gave me all the support, comfort, and encouragement that I needed for, this time in a quite different sense, my heart.

Contents

Chapter 1

Modeling the Heart - An Introduction

Cardiac arrhythmias are a leading cause of death in the industrialized world [90]. Consequently, physicians and physiologists have done intensive research on their causes in the past decades. The results of this research can now be combined with methods from mathematics and physics and today's computer power. This can lead to *quantitative* models of the heart, that open the door to a much more detailed diagnosis and therapy of heart diseases. The present thesis focuses on modeling the genesis of arrhythmias.

Modeling the heart is a daunting task but at the same time a promising means of overcoming heart disease. The heart consist of several billion coupled cells in a complicated geometry. Each cell can be electrically excited and subsequently contracts due to complex biochemical processes. Due to cell coupling, excitation can propagate in the heart, and the resulting excitation sequence is the basis of all cardiac activity. Timing is crucial so there are many special anatomical structures to tune the process of excitation propagation. On the level of the whole heart, excitation propagation interacts with muscle mechanics and the fluid dynamics of the blood flow. Whole heart modeling is therefore full of challenges and it will be a long time until a truly satisfying model combining all relevant aspects of the heart is constructed. Yet there is much to be gained, as computer models are an indispensable tool for getting a fundamental and quantitative understanding of how the heart works. They also provide a framework in which prospective therapeutic methods can be tested. At the moment, electrical, mechanical, and fluid dynamical aspects of the heart are usually modeled separately in order to limit the complexity. This thesis considers the heart and its cells as electrically excitable, but there is no movement of the heart and no flow of blood.

The smallest units of the heart that exhibits excitability and subsequent contraction are single heart cells. It is vital to understand the behavior of these building blocks in order to understand arrhythmias of the whole heart. Heart cells have been characterized in great detail, and the rhythms they exhibit have been studied using a wide range of stimulation protocols. However, even a complete understanding of single heart cells would not suffice to explain the heart's rhythm. The heart's rhythm really is, after all, the contraction pattern, which is anticipated by the excitation pattern, and this strongly depends how the cells are organized spatially.

Excitation patterns in the heart can be studied in realistic models or in simplified models that capture the heart's properties most relevant to wave propagation. With some model reduction, it can be seen that the mechanisms at the root of wave propagation are at work not only in the heart but in a larger class of media are called *excitable*. Excitable media provide the framework for our study and for modeling excitation propagation in the heart. Certain excitation patterns, e.g. spiral waves, have been found in many excitable media and their dynamics have been understood theoretically to some degree. Much of heart modeling is concerned with finding out which of these patterns exist in the heart as well and how their dynamics work there.

In this thesis, we will study heart rhythms at different levels, from single cells to the entire human atria. The main project of this thesis is the development of a realistic and efficient model of wave propagation in the human atria. We start by studying paced single cells and their loss of 1:1 rhythmicity for increasing frequency. We go on to study wave propagation in tissue with special electrophysiologic properties, related to chronical disease of the atria. Then we treat ionic models, which are a central part of our atrial model. We discuss a recently discovered mathematical degeneracy present in all models of cardiac cells that include intracellular ion concentrations and we explain why this degeneracy has only a negligible effect on wave propagation. We develop a method to reduce the complexity of ionic models while closely retaining their wave propagation properties. Then we apply this method to a realistic ionic model of the human atria and combine it with anatomical data to get the desired model. We use this model to explore possible mechanisms for the genesis of arrhythmias.

1.1 Heart Physiology

Following is a brief introduction to heart physiology. For more comprehensive treatments, consult standard textbooks, e. g. [114, 9].

The heart pumps blood to keep up a circulation. It consists of a right and a left half. The left half pumps blood rich in oxygen into the body. The oxygen is consumed and the blood is transported through the veins to the right half of the heart. From there it is pumped to the lungs where it is loaded with oxygen and finally carried back to the left half of the heart. Although both halves of the heart are integrated into a single organ, they pump at different points of the circulation. The structure of the circulation is therefore best revealed in a diagram with the halves of the heart separated (see Fig. 1.1) As the flow resistance of the body is greater than that of the lungs, the left half of the heart does more work and is more muscular.

Fig. 1.2 shows a sketch of the heart. Each half is separated into an atrium and a ventricle. The blood arrives from the body in the atria. When the heart contracts, the atria contract first, transferring the blood to the ventricles and ensuring their complete filling. Only after a delay of several hundred milliseconds do the ventricles contract and pump the blood to body and lungs. Between the atria and the ventricles, there are the atrioventricular valves that keep the blood from flowing back into the atria, In the same way, the semilunar valves between ventricles and arteries keep the blood from flowing back into the heart.

The cardiac contraction is preceded by electrical excitation, and the propagation of electrical excitation is really the mechanism initiating the action of the heart. Almost every heart cell (see Fig. 1.3) has a rest state in which it stays until it receives a supercritical electrical stimulus from a neighboring cell and a supercritical stimulus elicits an action potential (see Fig. 1.3). In this process, a number of ionic currents over the cell membrane are activated and the contraction is initiated. There are connections to neighboring cells, called gap junctions, and via them, excitation is propagated. With this mechanism for propagation, all that is needed for the heart to beat regularly is a pacemaker.

This pacemaker is the sinus node (see Fig. 1.4), a group of cells in the right atrium that oscillates spontaneously between rest state and excited state. Due to cell coupling, each excitation of the sinus node leads to a ring-shaped excitation front that quickly traverses the atria. Excitation does not spread from the atria to the ventricles, because they are electrically insulated. Only

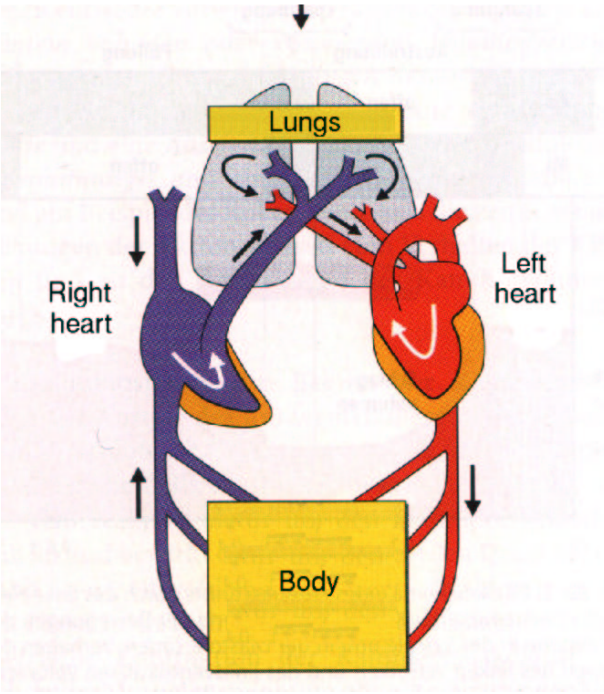

Figure 1.1: *The blood circulation through the human body. The two halves of the heart are drawn in separate locations to indicate that they are pumping at different places in the circulatory cycle. High-oxygen blood is shown in red, low-oxygen blood in blue.*

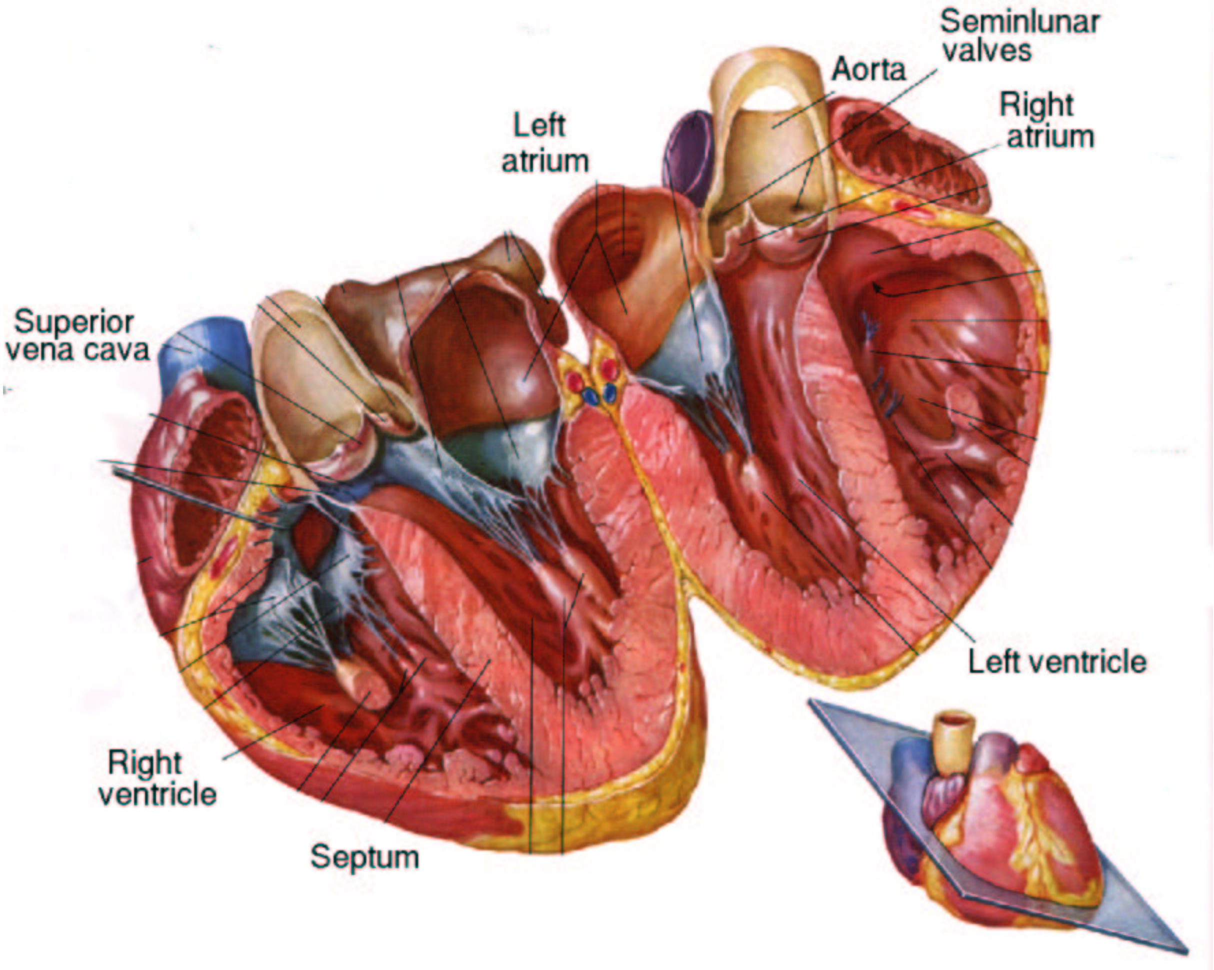

Figure 1.2: *Drawing of a section through the heart. Small subfigure to the lower left indicates the position of the section plane.*

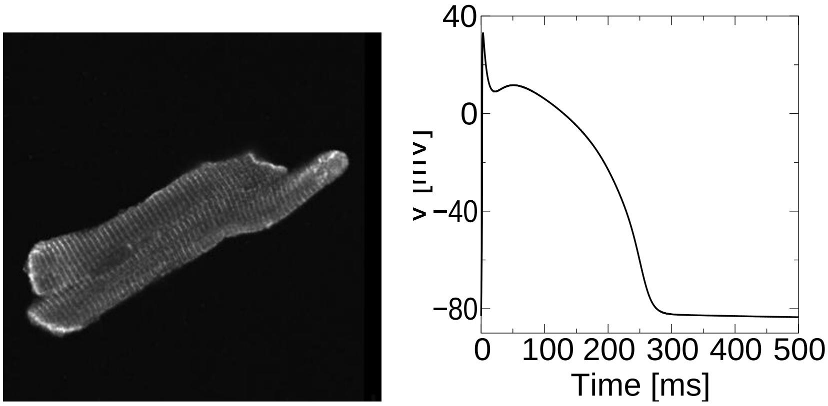

Figure 1.3: *Cardiac cells and their action potential.* **Left:** *Two cardiac cells as seen under an optical microscope. Their length is about 100µm, the diameter about 10µm.* **Right:** *the action potential as computed from the Beeler-Reuter model of cardiac cells [7].*

at one point, at the atrioventricular node, does conduction to the ventricles occur. Afterwards, the ventricles are traversed by excitation.

Excitation propagation in heart tissue is anisotropic. The heart cells have an oblong shape (see Fig. 1.3), and due to gap junction distribution, propagation speed is roughly three times faster in the direction of the cell's main axis (called local fiber orientation) than orthogonal to it. On top of this, there are specialized structures in both the atria and the ventricles that conduct excitation even faster (see Fig. 1.4). The purpose of these structures is to ensure a rather simultaneous excitation of the whole atria or ventricles, respectively, so that contraction will be simultaneous and therefore efficient. In the atria, the most prominent fast conducting structure is the *crista terminalis*, a ridge leading from the entry point of the upper vena cava to the entry point of the lower vena cava. Very similar are the *pectinate muscles* that run orthogonally from the crista terminalis into the right atrium. In the ventricles, there is an even more elaborate network of special pathways beginning at the bundle of His, branching into left and right branch and ending in the Purkinje fibers.

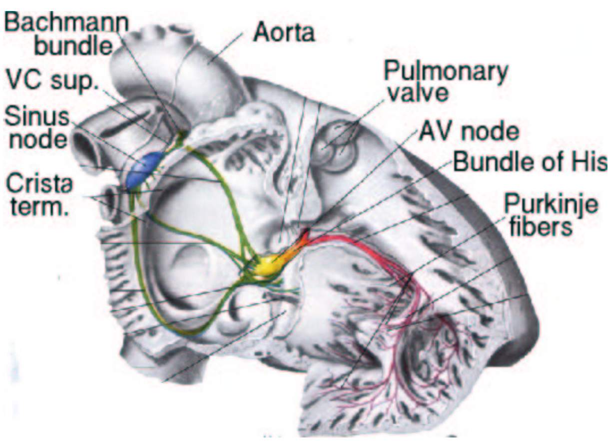

Figure 1.4: *The conduction system of the heart. Excitations are generated by the sinus node in the right atrium (blue). In the whole heart, excitations are propagated by all cells. Conduction is faster, however, in the special conduction pathways of the atria (green) and the ventricles (red). The only point at which electrical signals can pass from the atria to the ventricles is the AV node (yellow).*

1.2 Ionic Models of Heart Cells

In 1952, Hodgkin and Huxley in their seminal paper [55] gave the first quantitative model of the ionic mechanisms during an action potential. While they were studying the giant squid axon, i. e. a nerve cell, the model structure they propose has been universally accepted for heart cells, too. They viewed the cell as a capacitor, whose leads correspond to the inside and the outside of the cell (see Fig. 1.5). They identified two variable ionic currents through ionic channels in the cell membrane and represented in their model by variable conductances. To quantitatively characterize the variability of the currents, they introduced gating variables that enter multiplicatively in the ionic current. For example, the sodium current in their model is:

$$I_{Na} = g_{Na} \cdot m^3 \cdot h \cdot j \cdot (V - E_{Na}), \tag{1.1}$$

where m, h, and j are gating variables, V is the current transmembrane voltage and E_{Na} is the transmembrane potential at which there would not be any diffusive flow of sodium across the membrane.

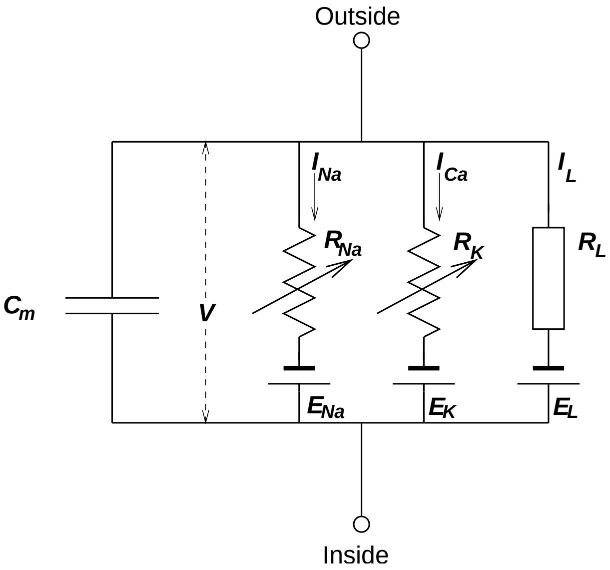

Figure 1.5: *The Structure of the Hodgkin-Huxley model. The inside and outside of the cell are modeled as two leads of capacitor, ion channels are represented by variable resistors. The Nernst potential is for each current implemented by a an additional voltage source.*

The dynamics of each gating variable can be described by two voltage-dependent functions: the steady-state function $y_\infty(V)$ (for any gating variable y), that describes towards which asymptotic value y is relaxing at the given V, and τ_y, saying with which time constant y relaxes. Mathematically:

$$\frac{dy}{dt} = (y_\infty(V) - y)/\tau_y(V). \tag{1.2}$$

This basic structure introduced by Hodgkin and Huxley model has been retained in all later ionic models of both nerve and heart cells. Even the most detailed models [78, 93, 21, 107] preserve this structure, though they may have many more ionic currents and gating variables.

The first model of ventricular fibers is by Beeler and Reuter [7], it includes the outward calcium current that causes the typical prolongation of action potential from 2-3 ms in nerve cells to 200-300 ms in cardiac cells. In 1985, Di Francesco and Noble published the first model of Purkinje Fibers [26]. Nowadays, the most popular models for cardiac tissue are the Luo-Rudy phase I and phase II models [77, 78, 79] consisting 8 and 12 variables, respectively, and the Noble et al. models [93] consisting of 40 to 60 equations. All these models are derived from animal experiments and describe non-human cells, typically guinea-pig or rabbit. Recently, the Luo-Rudy model has been modified using experimental data from human cells to describe single human atrial cells by Courtemanche et al. [21] and Nygren et al. [95] and to describe single human ventricular cells by Priebe and Beuckelmann [107].

The dynamical behavior of heart cells was another focus of much research, in real cells as well as in the various models. A central question is which rhythms a cell can exhibit under periodic stimulation [47, 45, 41, 54, 135]. Wave propagation in extended pieces is another central topic, that we treat in the more general context of excitable media in the following section.

1.3 The Heart as an Excitable Medium

One of the exciting properties of wave propagation in the heart is that it is very similar to wave propagation in other media. The reason for this is that wave propagation in the heart is based upon a few simple properties that other media share.

The first property is that each heart cell except for the pacemaker cells has a rest state that is stable with regard to small perturbations. Secondly, there

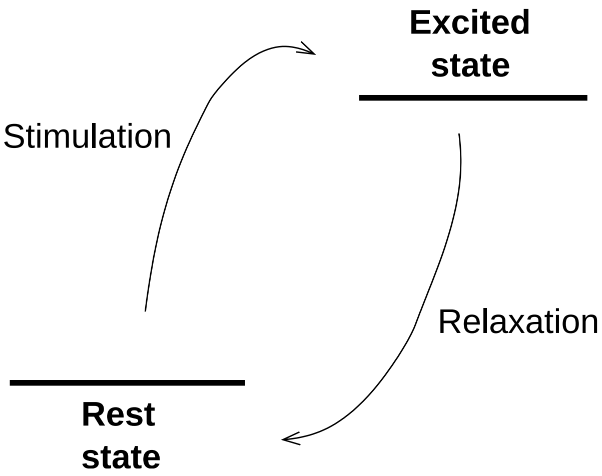

Figure 1.6: *Sketch of the basic features of an excitable cell. In absence of sufficiently strong stimuli, the cell remains in rest state. A supercritical excitation causes a long excursion in phase space ("excited state"), after which the cell returns to rest state.*

is a stimulation threshold above which the cell no more relaxes to rest state, but the cell is driven even further away by its intrinsic dynamics. Thirdly, the driving away from equilibrium eventually stops and the cell slowly returns to rest state, rendering it susceptible to new stimulation. A sketch of this behavior is shown in Fig. 1.6. The three mentioned properties constitute what is called the *excitability* of the cell, the application of a supercritical stimulus is called a successful stimulation or an excitation and the excursion in phase space that the cell takes after an excitation before coming back to rest state is called an *action potential* in a cardiology context. Finally, a prerequisite for wave propagation in the heart is that cells are coupled in a way that can be described by diffusion of transmembrane voltage. Since a rise in transmembrane voltage is really the stimulus needed to excite a cell, diffusion of transmembrane voltage provides a mechanism for the propagation of excitation.

Any diffusively coupled system of excitable cells is called an excitable medium. The first discovered and best studied example is the Belousov-Zhabotinsky (BZ) reaction. [8, 137, 127]. It is ideal from an experimental point of view: It has cheap and safe components, it can be set up in a petri dish, excitation shows by a change of color and can therefore be followed by the naked eye, and finally, excitation waves move so slowly (typically in the order of 1 mm/s) that they can easily be studied in detail. Consequently, the BZ has been the most popular system for the study of excitation patterns in excitable media. But excitability is present in many other media. Well-known examples are neural tissue [55], colonies of dictyostelium discoieum in the aggregation phase [81], or chemical reactions on platinum surfaces [68].

In one dimension, the only possible type of propagation is a traveling pulse. In two dimensions, the simplest patterns are a plane waves (they are essentially the same as a pulse in 1D) and circular waves caused by a point excitation. Much more interesting are spiral waves. They are characterized by a spiral-shaped wave front that is rotating in time. The inner end of the wave front, called the *tip*, may move around a circular region of the medium that is never excited, then called the *core* of the spiral [138], or on a path that usually has some symmetry but may be quite complicated, the tip is then said to be *meandering* [130]. What distinguishes spiral waves from plane waves and target patterns is that they leave the medium at the boundary only if the tip is meandering strongly and they can therefore persists for a long time. This leads to interesting problems regarding their long-term behavior. If a wave front in a spiral wave breaks, two new spirals can develop, which is called spiral breakup. In a medium where spirals inevitably break after some time, a spiral will degenerate into a large number of small excitory waves. This process may be important in the heart, where the healthy rhythm is replaced by a tachycardia, which might correspond to a spiral wave, and later degrades into fibrillation, which is made up of many small excitations. Other questions include the interaction of spirals or the dependency of spiral dynamics on the parameters of the medium.

In three dimensions, the analogue of a spiral wave is a *scroll wave*. It can be thought of as a spiral pulled up into the third dimension, so that the tip becomes a one-dimensional line, called the *filament*. This filament may of course be curved or even closed.

The most elaborate theory of spiral wave dynamics available [85] does not treat the partial differential equations that fully describe the excitable medium [85, 86], as this would be too complicated even for the simplest types of media. Instead, spiral waves are first reduced to their fronts, assuming the spatial width of these fronts is small compared to their wavelength. Then a front can be characterized by its curvature K as a function of arc length l and equations determining the development of $K(l)$ over time can be derived [138].

In modeling excitable media, the most fundamental question is whether the medium is mathematically described by differential equations (DEs) or by cellular automata. DEs are the natural setting, because the local dynamics are naturally described by ionic models, i. e. ordinary differential equations and the connectivity of the cells is well described by diffusion, leading to a partial differential equation.Unfortunately, DE modeling is computationally rather costly, and a much faster alternative are cellular automaton (CA) models [120, 128].

In CA models, a cell is characterized by a low number of internal states and simple rules about how neighboring cells interact. This reduces computations typically by one to two orders of magnitude compared to DE models. On the downside, CA models are reliable only in specific circumstances. For example, CAs can be made to almost perfectly reconstruct the activation sequence for sinus rhythm, because there, each cell is excited from rest state and goes through a very predictable series of states. Much on the contrary, during ventricular fibrillation, cells may receive very different types of stimuli and at the same time be in very different internal states themselves, so it seems impossible to construct a cellular automaton whose state space is much simpler than that of the DE model itself. So while CAs are interesting where speed is essential and the range of possible states is limited, DE models will always remain the method of choice if reliability and flexibility are the goal.

A minimal DE model of excitability was introduced by FitzHugh [33, 34] and Nagumo [91] and is now known as the FitzHugh-Nagumo model. While it was originally developed as a simplification of the Hodgkin-Huxley model (s. a.), the FHN model may also be arrived at by systematically looking for the simplest possible model exhibiting excitability. It has two variables that can be thought of as activator and inhibitor concentrations. The model has a stable fixed point for both activator and inhibitor concentrations at a low level. If the activator concentration is raised above some threshold, the activator catalyzes its own production so that the system moves further away from steady state. At the same time, the inhibitor is produced, although at a lower rate. Once a sufficient amount of inhibitor has accumulated, it reduces the activator concentration down to steady state level and then decays itself, so that the system is back at steady state.

The FHN model has greatly helped the understanding of excitability, because it is simple enough to be understood in great detail, in some aspects even analytically. Although the FHN model has a number of parameters that allow for the adjustment to certain desired properties, it is limited in the range of dynamical phenomena it can show, especially if compared to the latest ionic models of heart cells.

It is very challenging to find a model that is at the same time relatively simple and reliable. Phenomenological models like the FHN model are limited and their parameters do not have a direct physiological meaning. Full-fledged ionic models are hard to analyze and computationally too costly to be used in large-scale simulations. We show one way to develop an intermediate model in Chapter 4.

An important question in the context of finding efficient models is which properties of an excitable medium are actually relevant for the excitation patterns it can develop. Once these properties have been singled out, they can be used to check the quality of a proposed simplified model.

One property that is important in this respect is how the action potential and especially the action potential duration change with the duration of the diastolic interval (DI), i. e. the resting time before the stimulation. This relation is called the APD restitution curve (see Fig 1.7), and typically has the following properties: For very low DIs, the APD restitution curve is undefined, as a stimulus at the corresponding time cannot yet elicit an action potential. As DI becomes sufficiently large for APs to be initiated, the APs are still relatively short and APD rises with DI until saturation sets in at DI about 300 ms. The conduction velocity is usually a monotonous function of the DI as well; this function is called the CV restitution curve.

Both APD and CV restitution curve can be determined experimentally rather easily, and their predictive power is high: assuming that APD and CV are truly functions of diastolic interval (DI), an initial knowledge of the excitation fronts and DI everywhere actually suffices to determine all future states of the medium. The drawback of this description is, of course, that both APD and CV are *not* fully determined by the proceeding DI, but the variation of APD and CV is small in many situations.

The above considerations on how to improve computational efficiency of model become a must if the whole heart or large pieces of it are being modeled.

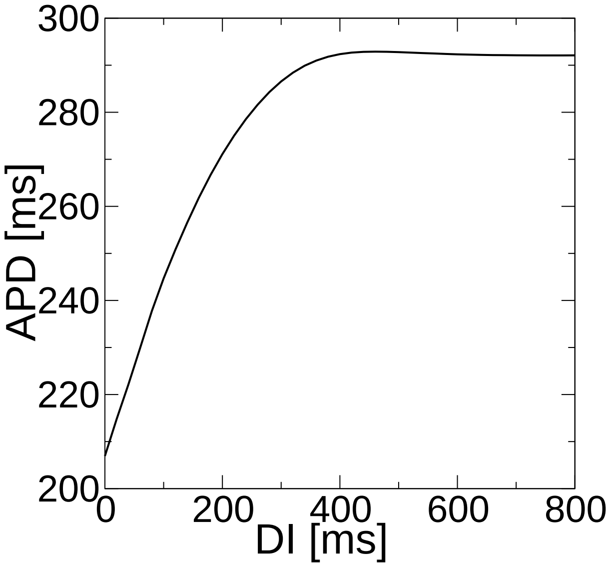

Figure 1.7: *Restitution curve of a human atrial cell. We show the duration of an action potential (y-axis) as a function of the resting time before the excitation (x-axis). Data was obtained from the Courtemanche model of human atrial cells [21].*

1.4 Whole Heart Modeling

The main goal of whole heart modeling is to gain a quantitative and experimentally verifiable understanding of the function of the heart. Although the function of the heart can be broken down into subsystems that may be studied individually, these subsystems need to be integrated at some point to ensure their correct interaction and to test whether the considered properties really suffice to describe the heart and to study the role of global properties like geometry.

A range of clinical procedures that are routinely being applied may be improved by means of whole heart models as well. The most common of these procedures is ablation, in which heart tissue is deliberately destroyed by means of overheating because it is suspected to be the origin of harmful spontaneous activity. Unfortunately, the way of tracking down the origin of spontaneous activity is still very imprecise so that considerable amounts of tissue are lost unnecessarily. Here, a good model could help to locate the focus of harmful activity more precisely. In a similar way, the positioning of the electrodes of an automatic defibrillator can be optimized using a realistic model.

Today's whole heart models are still far from integrating all important aspects of the heart. The heart is a muscular pump driven by propagating electrical waves. Therefore, a full virtual heart would need to incorporate the interaction of excitation patterns, mechanics, and fluid dynamics. Most research is concentrated on the especially important aspect of excitation dynamics and excludes mechanics and fluid dynamics [123, 1, 96, 11, 51] (for more references, see [100]). Similarly, models concentrating on mechanics and hydrodynamics of the heart [83, 84, 104, 105] use simple models of excitation.

Even within excitation modeling, further simplifying assumptions about geometry as well. Even today, the majority of simulation studies is still on two dimensional square lattices [5]. Such studies are useful, as they usually investigate effects that should persist in some form even in more realistic geometries.

But to investigate global excitation patterns and how one such pattern replaces another, one cannot do without realistic geometries. It is well known that curvature *does* have an effect of wave propagation as do junctions of surfaces, e.g. the septum joining the atria (or ventricular) wall. Also the anisotropy of cardiac tissue strongly favors certain directions of propagation. As a result, efforts have been taken to base models on anatomical geomet-

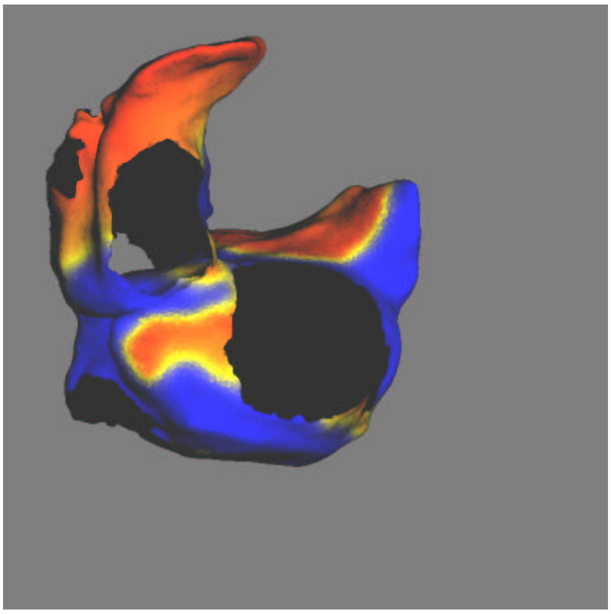

Figure 1.8: *Fibrillation in a model of the whole human atria. Left atrium is topmost, view is from ventricles, the large wholes are indeed the transition to the ventricles. Colors indicate transmembrane voltage, with blue corresponding to ≈-85 mV (resting potential) and red to ≈ 30 mV (peak potential). The simulation is from our whole-heart model (Chapter 7).*

rical data. These efforts were at first restricted to the ventricles, because ventricular arrhythmias are more dangerous than atrial arrhythmias. The anatomical models of the ventricles [69, 70, 71, 96] so far build on canine anatomy.

The development of anatomical models of excitation propagation in the atria has begun only recently. In 1999, Virag et al. proposed a model composed of two connected spheres with holes [11], and in 2000, Harrold and Henriquez published the first atrial model based on human anatomical data [51]. In Chapter 6 and 7, we present a new atrial model that for the first time includes anisotropy due to the fiber structure of the atrial wall. Our model is numerically efficient and includes special conduction pathways so it is ideally suited for extensive and realistic simulations of reentrant arrhythmias. As an example, Fig. 1.8 shows a simulation of atrial fibrillation.

1.5 Outline

This thesis comprises a number of studies, ranging from single cells stimulation over basic properties of excitable media to the development of an anatomical model of the human atria.

Chapter 2 is concerned with a periodically stimulated ionic model of human heart cells. Cells respond to very slow stimulation by generating one action potential per stimulation, but this response can only be maintained up to a certain stimulation frequency. Above that critical frequency, usually a period-2-rhythm occurs, either 2:1, where only every other stimulation produces an action potential, or 2:2, called alternans, where two different action potential shapes take turns. We investigate the onset of period-2-rhythms in the Beeler-Reuter model of ventricular fibers, find hysteresis and bistability at the onset of alternans. We quantify how blocking of specific ionic currents inhibits alternans and find that calcium buffers inside the cell generally promote the genesis of alternans.

In Chapter 3, we investigate the stability of spiral waves in excitable media exhibiting a special property called negative restitution. Negative restitution means that for certain ranges of the diastolic interval, the action potential duration becomes shorter for longer diastolic intervals. This unusual property has actually be found in heart cells, in particular in cells that are susceptible to sustained arrhythmia. We investigate how negative restitution can lead to instabilities in one-dimensional wave propagation and in spiral waves. We find that instabilities occur as soon as the slope of the restitution curve becomes steeper than -1, analogous to the established fact that spiral waves in media with positive (normal) restitution exhibit instabilities if the slope of the restitution curve becomes steeper than +1.

In Chapter 4, we study the effects of charge conservation violation that has been recently detected in a popular class of ionic models and that now literally hundreds of simulation studies suffer from. We quantitatively determine the connection between charge conservation violation and drift of rest state. Using this measure, we show that charge conservation violation has only minimal effects for simulations of wave propagation. The results of the many simulation studies of wave propagation violating charge conservation should therefore not be affected by this violation. We conclude by presenting the proper method of simulating wave propagation in second-generation models, given today's understanding.

In Chapter 5, we propose a method to reduce the complexity of ionic models. By this method, the Courtemanche et al. model, one of the most realistic descriptions of human atrial tissue available today, can be reformulated to be computationally substantially more efficient, while important electrophysiological properties are retained. By fixing ionic concentrations and combining gating variables, we increase simulation speed by a factor of almost 4. To validate the model, we compare the original and the reformulated model with regard action potential shape, action potential duration and conduction velocity restitution, achieving good agreement. We then study spiral waves in the reformulated Courtemanche model versus a model of remodeled atrial tissue that has undergone electrophysiologic changes as a result of continued atrial fibrillation.

The main project of this dissertation, the development of a realistic model of excitation propagation in the human atria, is introduced in Chapter 6. Starting from human anatomical data, we construct a realistic geometry, including fiber orientations and special conduction pathways. The electrophysiology of the cells is described by the efficient and yet realistic model developed in Chapter 5. We use our realistic model to study which geometrical aspects of the atrium make a difference of possible clinical importance. Finally, we summarize our results in Chapter 7.

Chapter 2

Alternans and 2:1 Rhythms in an Ionic Model of Heart Cells

ECG alternans is commonly held to be an indicator of electrical instability of the heart, but the development of alternans has not yet been fully understood theoretically. We investigate the onset of alternans and 2:1 rhythms for stimulation at increasing frequencies in the Beeler-Reuter model, a simple ionic model of myocardial tissue. We find hysteresis and bistability at the onset of alternans; well-timed stimuli can switch between the two limit cycles. We determine quantitatively the effect of blocking specific ionic currents. Moreover, we find that calcium buffers generally promote alternans.

2.1 Introduction

Nonlinear dynamics have been used successfully to understand biological rhythms (see [129, 43, 44], for nonlinear dynamics in the heart in particular, see [42, 100]). A common rhythm in biological signals is *alternans*, in which a signal consists of two alternating segments. Alternans often develops out of a periodic signal when a parameter is changed; it is then an example of a period doubling bifurcation.

Mechanical alternans in the heart has been observed already more than a century ago [39]. ECG alternans has been connected to malignant arrhythmias and has become accepted as a predictor of forthcoming arrhythmic events [112]. Consequently, numerous experiments and some numerical simulations investigating alternans have been carried out [46, 72, 118, 18, 119, 12, 49, 135, 48], for a review refer to [31].

Alternans has been shown to exist in single cells, in experiment as well as in theory [46] (see Section 2.2). Single heart cells and fibers are the smallest units to exhibit alternans and understanding the development of alternans should be most feasible in them.

In the context of paced systems, alternans is also called a 2:2 rhythm, as two stimuli lead to two action potentials of different shape. Likewise, a rhythm in which only every other stimulus induces an action potential is called 2:1. We study in detail the development of 2:2 and 2:1 rhythms in the paced Beeler-Reuter (BR) model of myocardial tissue as the stimulation frequency is increased. Previous experimental studies have shown that the 1:1 → 2:2 transition exists in bullfrog tissue [48] and chicken tissue [46]. Model studies showed that the 1:1→ 2:2 transition occurs in the BR model [59, 46], a cable of BR cells [72] and a sheet of cells of the more detailed Luo-Rudy model [5]. Besides, transitions from 1:1 to other rhythms than alternans and further bifurcations have been described in several studies [4, 28, 135].

We find and study hysteresis and bistability in the onset of alternans in the BR model. Then we quantify how blocking individual ionic currents can inhibit the development of alternans. Finally, we extend the BR model to include scalable calcium buffers and see how calcium buffer efficiency influences the onset of alternans.

2.2 The Stimulated Beeler-Reuter Model

Ionic cell models were invented by Hodgkin and Huxley in 1952. Since then, many new ionic currents have been found and studied, and heart cell models aiming at completeness have become very complex [78, 21, 107]. Because we are not interested in a precise reconstruction of all cell properties but in an understanding of the mechanisms that lead to alternans, we chose the simple BR model as a starting point [7]. It is the simplest ionic model that accurately reproduces the action potential of myocardial tissue (see Fig. 2.1) and is widely used to model ventricular cells [72, 15, 108].

We add a periodic extra current to the BR model to simulate periodic excitation. Then we study the effect of increasing stimulation frequency.

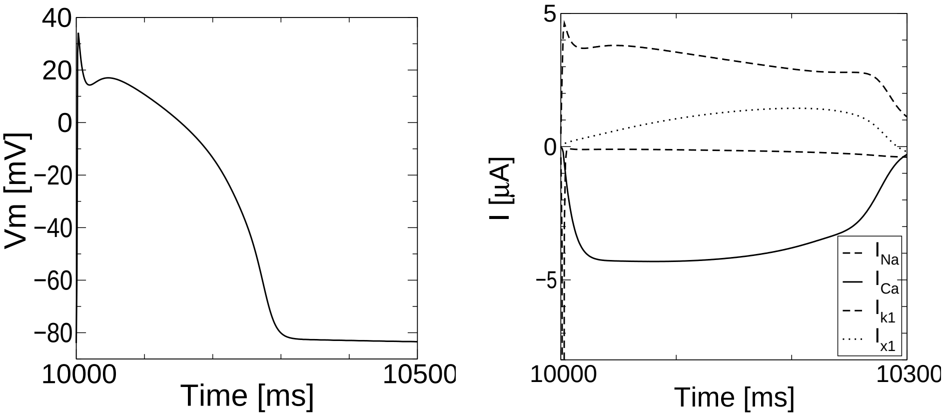

Figure 2.1: *Action potential (left) and ionic currents (right) in the BR model. Note that the sodium current is very short and very strong (it leaves the plotted range and goes down to -150* $\mu A/cm^2$*).*

2.2.1 The Model Equations

In the Beeler-Reuter model [7], the transmembrane Voltage V (always in mV) changes according to

$$\frac{dV}{dt} = -(1/C_m)(I_{ion} + I_{stim}). \tag{2.1}$$

where C_m is the membrane capacitance (in μF) I_{ion} is the sum of the ionic currents (in μA) and I_{stim} is the stimulus current. The ionic current I_{ion} consists of

$$I_{ion} = I_{Na} + I_s + I_{K_1} + I_{x_1}. \tag{2.2}$$

The fast inward sodium current I_{Na} is given by

$$I_{Na} = (g_{Na} m^3 \cdot h \cdot j + g_{NaC})(V - E_{Na}), \tag{2.3}$$

where g_{Na} is the maximal sodium conductivity, g_{NaC} is the sodium leak conductivity, E_{Na} is the sodium equilibrium potential and m, h, and j are gating variables. Similarly, the slow inward current I_s is given by

$$I_s = g_s \cdot d \cdot f \cdot (V - E_s), \tag{2.4}$$

where g_s is the maximal calcium conductivity, E_s the calcium equilibrium potential [7] and d and f are gating variables. The potassium current I_{K_1} is simply a function of transmembrane voltage:

$$I_{K_1} = I_{K_1}(V), \tag{2.5}$$

and the time-activated outward current I_{x_1},

$$I_{x_1} = x_1 \bar{I}_{x_1}(V), \tag{2.6}$$

has a gating variable x_1. The functions I_{K_1} and I_{x_1} are given in [7].

The gating variables m, h, j, d, f, and x_1 follow the dynamics

$$\frac{dy}{dt} = (y_\infty(V) - y)/\tau_y(V); \quad y \in \{m, h, j, d, f, x_1\}. \tag{2.7}$$

The individual expressions for y_∞ and τ_y are given in [7]. Finally, intracellular Ca (always in μmol/l) changes according to:

$$\frac{d}{dt}Ca_i = -k_i I_s + \frac{1}{\tau_{Ca}}(Ca_{i,eq} - Ca_i). \tag{2.8}$$

For integration, we use a forward Euler scheme with $\Delta t = 0.02$ ms.

2.2.2 Stimulation

The BR model has an attractive fixed point at $(V,\ Ca_i,\ x_1,\ m,\ h,\ j,\ d,\ f) = (-84.6,\ 0.178,\ 0.0056,\ 0.011,\ 0.99,\ 0.97,\ 0.0030,\ 1.00)$, corresponding to the rest state of heart tissue. Stimulation is simulated by means of a short extra current I_{stim}. The duration of this current is taken to be 2 ms, which is a typical value used in experiments [29, 46, 72, 89], and the amplitude is set at two times the threshold value necessary to induce an action potential (this threshold was 26 μA).

We consider the model's response to a stimulus an action potential whenever the sum of the ionic currents is negative at the end of the stimulus, i. e. if there is further depolarization due to the cell's own dynamics. For every action potential, we define the action potential duration (APD) by the time between stimulus and the moment where transmembrane voltage goes back below -20 mV.

To get an overview of the behavior at different stimulation frequencies, consider the sequence of APDs produced by stimulation at a certain frequency as plotted in Fig. 2.2. Alternans sets in at a frequency of about 3.55/s. The duration of the shorter action potential drops quickly to below 50 ms and continues to decline. At 3.63/s, there is a transition 2:2 → 2:1. This remains stable for a wide range of stimulation frequencies, and only at about 6.65/s there are further bifurcations and irregular behavior, in good agreement with experimental results [54]. Note that we restarted the system from rest state

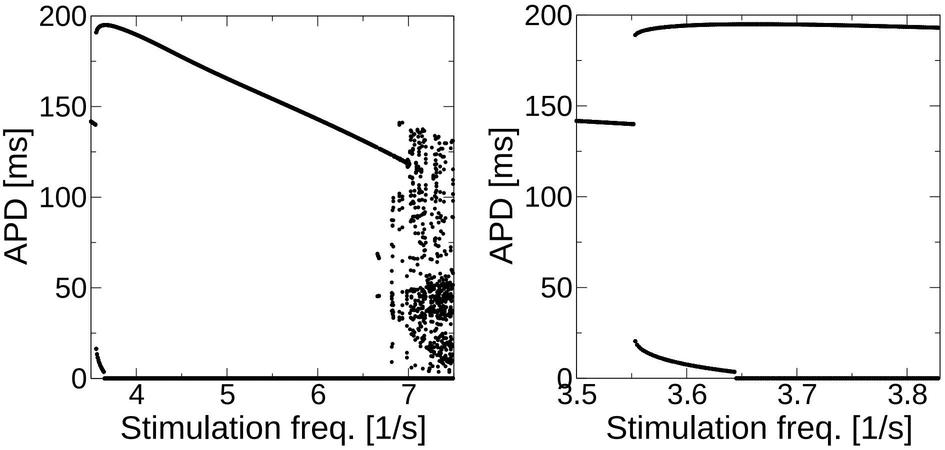

Figure 2.2: *Bifurcation diagram of the stimulated BR model. For every stimulation frequency we let 100 stimulations pass unrecorded and plot the following 20 APDs. Ineffective stimuli are assigned an APD of 0 ms. Right panel zooms into the first bifurcation, here we let 500 stimulations pass unrecorded.*

for every frequency. The result is significantly different if the system is not restarted, as shown below.

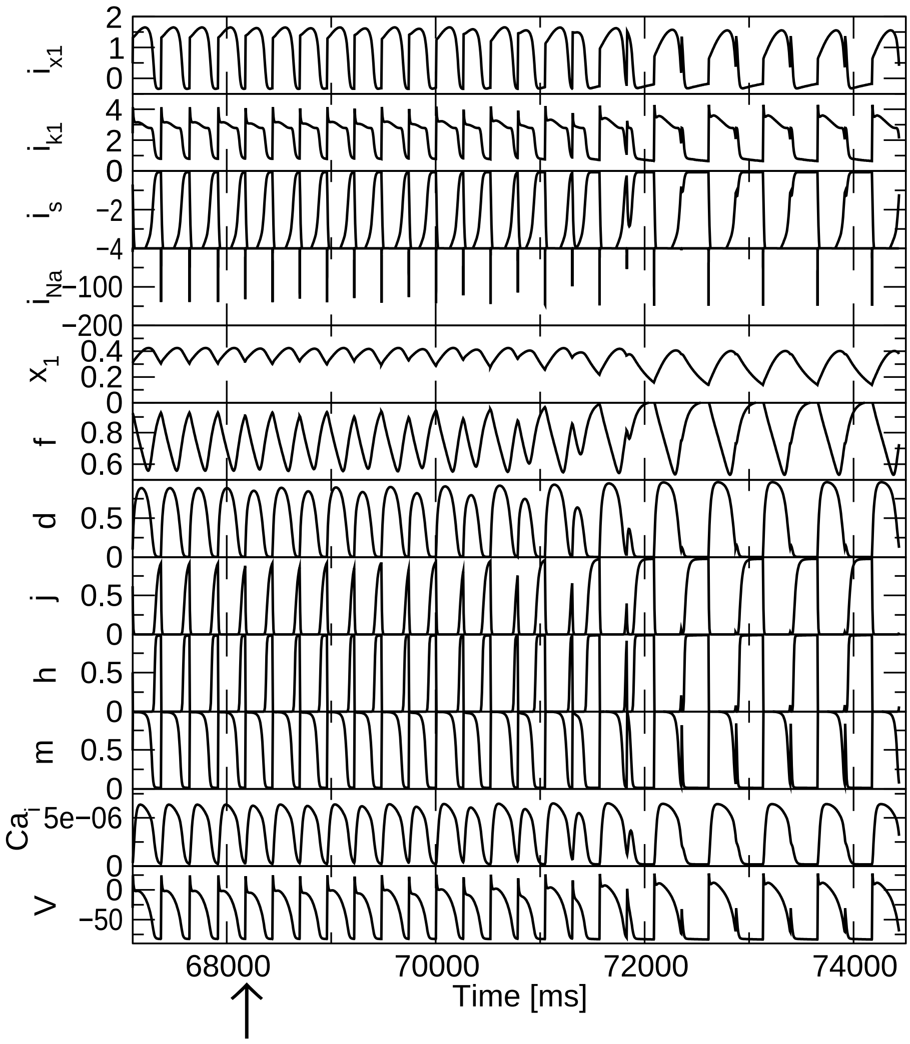

Figure 2.3: *All model variables and ionic currents as a 2:1 rhythm sets in. Stimulation frequency has been increased in steps of 1/s without initializing, so that 2:1 has not yet set in at 3.67/s. We show the last four stimulations at 3.67/s and then switch to 3.83/s stimulation (arrow), again without initializing. After some transients, there is a stable 2:1 rhythm. Units are mV for* V*, mol/l for* Ca_i *and* μA *for the currents.*

2.3 2:1 Development in the BR Model

Fig. 3 shows in detail how a 2:1 rhythm sets in. It appears that the first signs of the transition are in the closing variable j of the sodium current. A simple explanation for the onset of 2:1 at high frequencies is that ever faster stimulation leaves less and less time for recovery, and at some point, j is no more reset to 1. In this situation, a newly given stimulus cannot initiate a sodium current, and the resulting voltage signal is much smaller than in a full action potential. In the following period, there is plenty of time for relaxation; thus, the next stimulus can therefore easily initiate a full action potential. The result is an alternation between full action potentials and small/no action potentials.

However, this explanation is somewhat simplistic. While it is true that alternation can be inhibited by letting j and h relax at higher voltages, one can inhibit 2:1 rhythms and alternans even better by changing other model features, as will be shown in section 2.3.2.

2.3.1 Hysteresis and Bistability

There is hysteresis in the onset of 2:1 in the BR model (see Fig. 2.5). We first increased the stimulation frequency in steps of 0.01/s, this time without resetting the variables to rest state at each new frequency. Alternans sets in not before 3.7/s and soon afterwards develops into a 2:1 rhythm. For decreasing stimulation frequency, a 2:1 rhythm persists down to 3.63/s, followed by alternans down to 3.55/s, where it is replaced by a 1:1 rhythm. Hysteresis has been reported recently in the Luo-Rudy model [135] as well. Thus, in any study of alternans onset, the initial conditions have to be specified.

The presence of hysteresis shows that, at certain frequencies, there are at least two attractors in phase space, the 1:1-attractor and the 2:2/2:1 attractor. The 1:1 attractor disappears for sufficiently high frequencies, whereas the 2:2/2:1 attractor disappears for sufficiently low frequencies. To understand this effect in more detail, we study the development of the basins of these two attractors with changing frequency. As the system is eight-dimensional, a complete determination of the basins is impractical, so we take two different approaches.

In our first study, we consider not full phase space, but a physiologically especially important subset, i. e. the set of states traversed during a standard action potential (from 1/s stimulation). This subset can be parameterized by

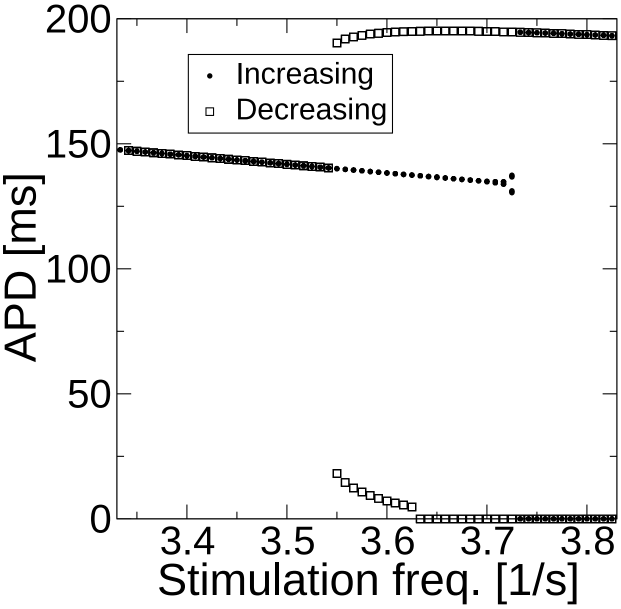

Figure 2.5: *Hysteresis in the onset of alternans. Solid circles show the onset of alternans for increasing frequency, empty squares for decreasing frequency. We changed stimulation frequency in steps of 0.01/s, using the final state of one frequency as the initial state of the next.*

the phase of the action potential, which we normalize to range from 0 to 1. Our question thus becomes which phases of the standard 1/s action potential as initial condition lead to a 1:1 rhythm and which to a 2:2/2:1 rhythm; this depends on stimulation frequency. Fig. 2.6 shows the results. As expected the basin of the 1:1-attractor becomes progressively smaller with frequency. A phase close to 1 drops out of the 1:1 attractor already at a rather low frequency. This is because the first stimulation will produce a long action potential and the second stimulation is likely to meet unrecovered tissue; this is a good starting point for alternans. Note that stimulation from rest state leads to alternans easily for the same reason. Indeed, the bifurcation frequency in Fig. 2.2 almost coincides with the frequency at which the 1:1 basin starts getting smaller (ca. 3.55/s in both cases), and also with the frequency of the 2:2→1:1 transition in Fig. 2.5. On the other hand, in two small interval of initial phases around 0.07 and 0.343, the 1:1 rhythm is stable almost as long as in the hysteresis protocol. This shows that our chosen subset gets close (in phase space) to the 1:1 attractor over the whole range of frequencies considered.

In a second study, we studied how results of our original hysteresis protocol change if we add uncorrelated equally distributed noise to the transmembrane voltage in every time step. This is a way of testing how close to the boundary of the basin the system is as it moves along the attractor. Fig. 2.7 shows that the increasing noise shifts the transition 1:1→2:1 to lower frequencies. In much the same way, increasing noise shifts the backwards transition 2:2→1:1 to higher frequencies (no picture shown), but the shift is much smaller. This indicates that the basin of 2:2 disappears much more abruptly.

Finally, we use the insight we gained to demonstrate how accurately placed extra stimuli can induce switching from one attractor to the other in the bistable regime. In Fig. 2.8, the cell is paced at 3.56/s and is initially in a 2:2 rhythm. By putting an extra stimulus at phase 0.5, we induce a switch to a 1:1 rhythm. After 8 beats in 1:1 rhythm, we set another stimulus at phase 0.8. This induces a switch back to 2:2 rhythm. The placement of both stimuli is not critical, the switching occurs for a range of phases.

2.3.2 Alternans Inhibition

To inhibit alternans while retaining the basic action potential shape, either the relaxation has to be accelerated or the rest state has to be moved so

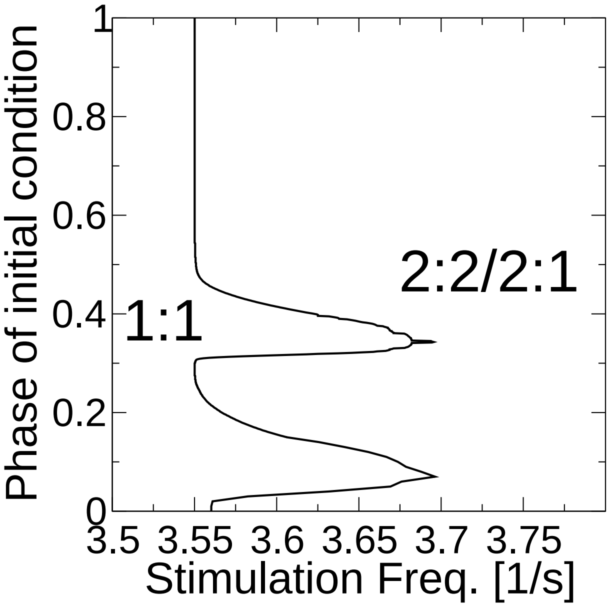

Figure 2.6: *Basins of the 1:1 and the 2:2/2:1 attractor as a function of stimulation frequency. We consider as initial conditions states from a standard 1/s-stimulation limit cycle (parameterized by its phase). Each vertical section of the figure shows which of these initial conditions lead to 1:1 and which to a 2:1/2:2 rhythm. Reading the figure from left to right, for low frequencies, any initial condition from the standard cycle leads to a 1:1 rhythm, while for faster stimulation an ever smaller part does so; for frequencies above 3.7/s, any initial condition from the standard cycle leads to a 2:2/2:1 rhythm. For phases between 0 and 0.15, V reaches values outside our tabulation range, so for these phases, we performed calculation without tabulation. For a given phase, the alternans onset frequency rises by about 0.01/s if tabulation is turned off.*

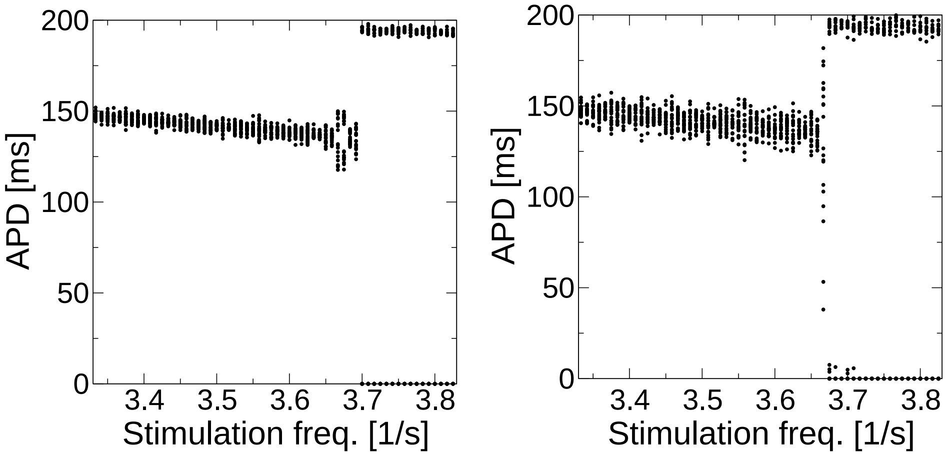

Figure 2.7: *The effect of noise on the stability of rhythms. The protocol is as in Fig. 2.5, but at each time step, we add uncorrelated equally distributed noise to* V*. In the left panel, the amplitude of this noise is* ± 2 *mV, in the right panel* ± 4 *mV.*

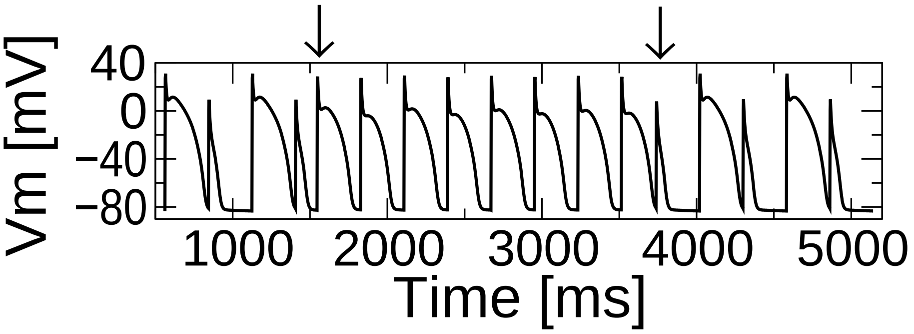

Figure 2.8: *In the bistable regime, a single well-timed pulse can switch rhythms. Starting from a 2:2 rhythm, an extra stimulus indicated by the first arrow induces a transition to a 1:1 rhythm. This transition is reversed by a second extra stimulus indicated by a second arrow.*

that it is reached earlier. Acceleration of the relaxation via modification of ionic currents is promising, because drugs to modify the channel behavior are known [29]. We quantify the effect of altering an ionic current by introducing a constant c_{mod} by which the current is multiplied. For several values of c_{mod}, we determine the frequency of alternans onset. Note that this setting is also a valid description of natural deviations of current amplitudes, e.g. due to genetically caused differences in ion channel densities.

Fig. 2.9 shows the effect of modifying the sodium, calcium, and potassium currents. Amplification of the sodium current inhibits alternans, because a strong initial peak in the action potential lifts x_1 so that repolarization is strong from the beginning. Stronger repolarizing potassium currents also shift the alternans onset frequency to higher values. A strong calcium current promotes alternans, because calcium is the main depolarizing current.

The onset of alternans is most sensitive to changes in the calcium current and the potassium current i_{k1}. It is rather insensitive to i_{Na}, because no matter by which factor i_{Na} is multiplied, it is turned off by h soon after V becomes positive. The dependency on i_{x1} is not strong either, because i_{x1} is "self-inhibiting": A strong i_{x1} inhibits excitation and that way prevents x_1 from becoming large at the initial peak. Consequentially, i_{x1} does not grow as much as might be expected from the increase in x_1.

Moving the recovery threshold to higher transmembrane potentials obviously inhibits alternans, but the inhibition is significant only if the threshold is moved strongly (not shown).

2.4 Alternans and Calcium Buffering

Another mechanism in heart cells that might be effective in the development of alternans is calcium buffering. We will introduce simple calcium buffers with adjustable efficiency and study how the efficiency influences the onset of alternans. An overview of recent calcium buffer models can be found in [44].

In the Beeler-Reuter model, there is a "restoring force" that drives Ca_i towards its resting value (see Eq. 2.8). This restoring force does not reflect calcium buffering adequately. In fact, the most important effect of the restoring force is that it drives the calcium back out of the cell, as there is no other outward calcium current. Therefore, when we introduce more realistic calcium buffering, we cannot just drop the restoring force, and we will keep

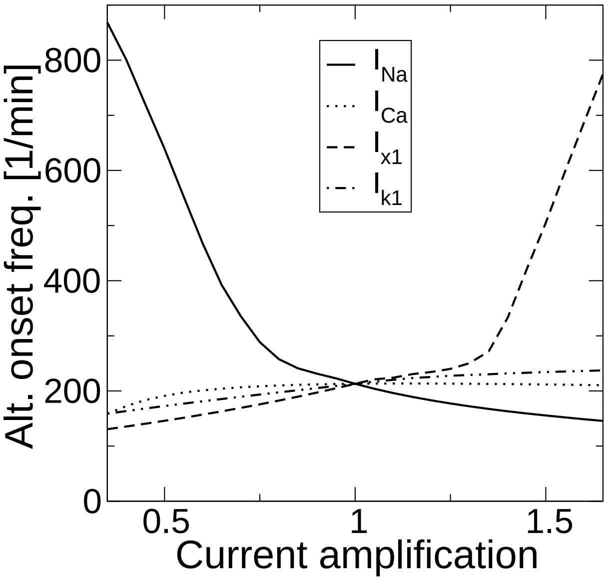

Figure 2.9: *Effect of modifying the ionic currents in the BR model on the development of alternans. For each ionic current, we introduced a global modification factor. We changed this modification factor from 0.35 to 2.0, where a factor of 1 corresponds to the original current.*

it with the calcium buffers we introduce. We interpret the restoring force as an outward calcium current that serves to maintain equilibrium calcium concentration.

The structure in the cell that stores calcium is the sarcoplasmic reticulum (SR), a network of tubes that pervades the cell. Parts of the surface of the SR contain pumps that transport calcium from the myoplasm into the SR; the corresponding parts of the SR are called *uptake* compartments. In other parts of the SR, ion channels for calcium release dominate, they are called the *release* compartments. This structure suggests two-compartment calcium buffers, which are in fact used in detailed modeling of calcium dynamics [78]. The compartments and calcium currents between them are shown in Fig. 2.10. The dynamic equations are:

$$\begin{aligned} \frac{d}{dt}Ca_i &= j_3 - j_1, \\ \frac{d}{dt}Ca_u &= (j_1 - j_2)/V_u, \\ \frac{d}{dt}Ca_r &= (j_2 - j_3)/V_r, \end{aligned} \tag{2.9}$$

where Ca_i, Ca_u and Ca_r are the calcium concentrations (in mol/l) of the intracellular medium, the uptake, and the release compartment, respectively. V_u is the volume of the uptake compartment, V_r the volume of the release compartment, the volume of the myoplasm has been normalized to 1.

We chose the currents j_i in the simplest possible way compatible with physiology. The calcium uptake j_1 is caused by pumps, which are usually modeled using Michaelis-Menten kinetics. We further simplify j_1 by assuming linear operation, $j_1 = d_1 Ca_i$. The translocation of the calcium from uptake to release compartment is brought about by diffusion and modeled here (as usual) by $j_2 = d_2(Ca_u - Ca_r)$. Calcium release j_3 increases with Ca_i as well as with Ca_r ("calcium-induced calcium release"). Physiologic models often use complicated formulations for this current. We chose the simplest term that includes the basic dependency on both Ca_i and Ca_r, $j_3 = d_3 Ca_i Ca_r$.

The resulting model still has the free parameters d_1, d_2, and d_3 (V_u and V_r are known [78]). We think the best way to get realistic values for the free parameters is to impose conditions on important physiological quantities that can easily be measured and functionally depend on d_1, d_2, and d_3. We consider the steady state values of Ca_i, Ca_u, and Ca_r in the absence of calcium

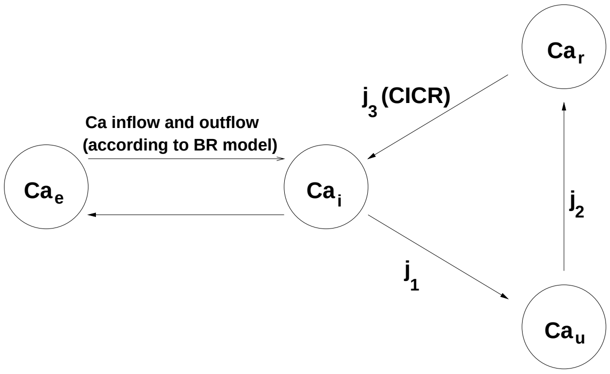

Figure 2.10: *Structure of the proposed model for calcium buffers in the cell. The Ca_e compartment represents the extracellular medium, the Ca_i compartment the myoplasm and the Ca_u and Ca_r compartments the calcium uptake and release parts of the sarcoplasmic recticulum.*

current from the extracellular medium, i. e. we disconnect the BR model from the calcium dynamics. Setting $j_1 = j_2 = j_3$ in Eq. (2.9) becomes

$$d_1 Ca_i = d_2(Ca_u - Ca_r) = d_3 Ca_i Ca_r. \tag{2.10}$$

Therefore,

$$Ca_r = \frac{d_1}{d_3}, \text{ and } Ca_u = \frac{d_1}{d_3} + \frac{d_1}{d_2} Ca_i. \tag{2.11}$$

Two conditions are imposed on d_1, d_2, and d_3 if Ca_i, Ca_u, and Ca_r are required to take on physiologically realistic values (the order of those given in [78], $Ca_i \approx 0.17$ μmol/l, $Ca_u \approx 1800$ μmol/l, and $Ca_r \approx 1700$ μmol/l). We use the last free parameter for the adjustment of the time constant τ with which perturbations of the steady state relax. The functional dependency of τ on d_1, d_2 and d_3 is gained by linearizing the dynamics (2.9) at the steady state and calculating the eigenvalues of the Jacobi matrix. Setting $\tau = 180$ ms, a typical time-constant of Ca-relaxation [78], yields after some calculation

$$d_1 = 8.67 \cdot 10^{-2}, d_2 = 1.56 \cdot 10^{-4}, d_3 = 50.98. \tag{2.12}$$

We now consider the model as shown in Fig. 2.10. The BR equations and the calcium buffer equations are linked at the intracellular calcium, whose rate of change is

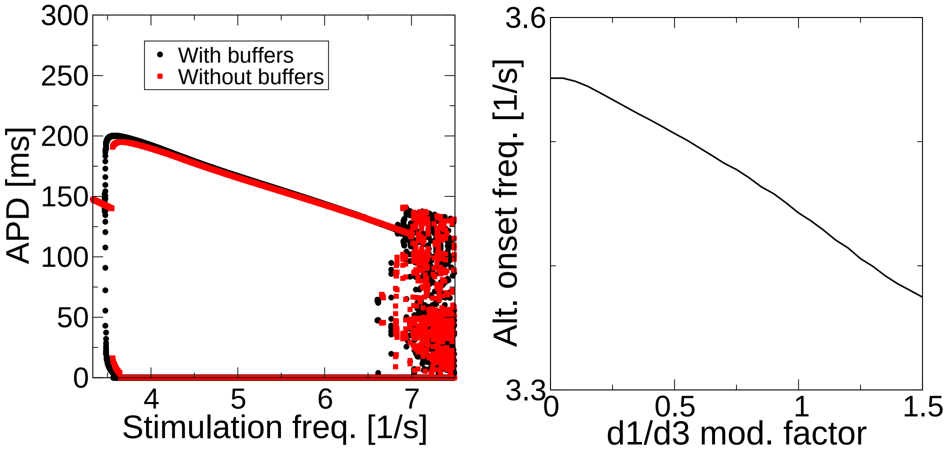

Figure 2.11: *The effect of the calcium buffers on the onset of alternans. Left panel shows the slight shift towards lower frequencies in the bifurcation diagram. The protocol is as in Fig. 2.2. Right panel shows the shift of alternans onset frequency as a function of calcium buffer efficiency; here we restarted from rest state for each frequency.*

$$\begin{aligned}\frac{d}{dt}Ca_i &= -k_i I_s + \frac{1}{\tau_{Ca}}(Ca_{i,eq} - Ca_i) - d_1 Ca_i + \\ &\quad +d_3 Ca_r Ca_i.\end{aligned} \tag{2.13}$$

The basic structure of the bifurcation diagram of the BR model is not changed by the new Ca-buffering mechanism (Fig. 2.11).

To assess the effect of calcium buffers quantitatively, we simultaneously vary the strength j_1 and j_3 by multiplying them with an identical factor and determine the corresponding alternans onset frequencies. As shown in Fig. 2.11, the stronger the uptake pump, the earlier alternans sets in, which means that calcium buffering promotes the development of alternans.

To understand this effect, consider how the net calcium inflow $d/dt(Ca_i)$ is modified by the buffers. The effect of the calcium buffers has two components, which can clearly be seen in Fig. 2.12. On the one hand the calcium release, which is fast but small, produces an extra initial peak in Ca_i. On the other hand the calcium uptake considerably decreases Ca_i over the second part of the action potential. The lower Ca_i causes the equilibrium potential for calcium to rise and that way increases the calcium current slightly (Eq. 2.4).

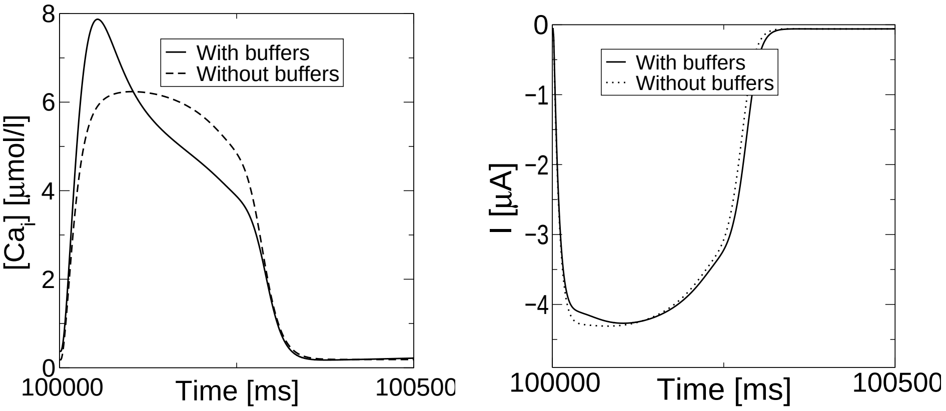

Figure 2.12: *The effect of the calcium buffers on calcium concentration and calcium current. In both panels, model cells were stimulated at low frequency (1/s) and transient have passed.*

As the calcium current is depolarizing, repolarization is delayed. The balance of de- and repolarizing currents during an action potential is delicate, so that the slight change in calcium current leads to a sizable shift of alternans onset frequency.

2.5 Discussion

Alternans is linked to dangerous arrhythmias and understanding its mechanisms is of great clinical importance. We studied the onset of alternans in a simple model. In this simple model, we were able to understand in detail hysteresis and bistability at the onset of alternans, the potential for inhibiting alternans by blocking specific currents, and the influence of calcium buffers on alternans development. We believe that similar mechanisms apply to more detailed models and the real cell, where the existence of hysteresis and bistability has already been shown [48, 135].

We are not aware of any experimental study that investigates the effect of calcium buffers on alternans genesis. Methods for blocking of calcium buffers are, however, available [6, 60], so it can be tested if the mechanisms we describe are indeed effective, or if the relationship between calcium buffering and alternans genesis is more complex in real cells.

2.6 Appendix: Modifications in the Calcium Buffer Model

2.6.1 New State variables

Ca_u	calcium concentration in the uptake compartment
Ca_r	calcium concentration in the release compartment

2.6.2 New Dynamic Equations

$$\begin{aligned}\frac{d}{dt}Ca_i &= -10^{-7}i_{Ca} + 0.07 * (10^{-7} - Ca_i) - \\ & \quad j_1 + j_3 \end{aligned} \tag{2.14}$$

$$\frac{d}{dt}Ca_u = (j_1 - j_2)/V_u \tag{2.15}$$

$$\frac{d}{dt}Ca_r = (j_2 - j_3)/V_r$$

2.6.3 Calcium Currents in the Cell

$$j_1 = d_1 Ca_i \tag{2.16}$$

$$j_2 = d_2(Ca_u - Ca_r) \tag{2.17}$$

$$j_3 = d_3 Ca_i Ca_r \tag{2.18}$$

2.6.4 New Constants

Name	Meaning	Value	Unit
d_1	strength of calcium uptake pump	0.0867	s^{-1}
d_2	strength of diffusion from uptake to release	$1.56 \cdot 10^{-4}$	s^{-1}
d_3	strength of calcium-induced calcium release	50.98	s^{-1}
V_u	volume of the calcium buffer uptake compartment (relative to the cytoplasm volume)	0.06	
V_r	volume of the calcium buffer release compartment (relative to the cytoplasm volume)	0.006	

Chapter 3

Wave Propagation in an Excitable Medium with a Negatively Sloped Restitution Curve

Recent experimental studies show that the restitution curve of cardiac tissue can have a negative slope. We study how the negative slope of the restitution curve can influence basic processes in excitable media, such as periodic forcing of an excitable cell, circulation of a pulse in a ring, and spiral wave rotation in two dimensions. We show that negatively sloped restitution curve can result in instabilities if the slope of the restitution curve is steeper than -1 and report different manifestations of this instability.

3.1 Introduction

Complicated spatio-temporal patterns play an important role in excitable media of various types. If such patterns occur in cardiac tissue they cause cardiac fibrillation, which is one of the main causes of death in the industrialized world[90]. In many cases, complex spatio-temporal patterns arise as a result of some type of instability. The type of instability most studied today is the so-called alternans instability. This instability may occur if one forces an excitable medium with a sufficiently short period. In this case, instead of a periodic response with the same period as the stimulus, the durations of successive action potentials begin to alternate (e.g. short-long-short-long etc.). There is a simple criterion governing the onset of alternans, based on the restitution curve of the tissue, which relates the action potential duration (APD) to the diastolic interval. The diastolic interval (DI) is the time that has elapsed between the end of the preceding action potential and the start of the next one. An alternans instability can occur if the slope of the restitution curve is more than one [94, 45]. In two-dimensional excitable media, an alternans instability can cause spiral breakup: fragmentation of one spiral wave into a spatio-temporally chaotic pattern comprising many wavelets of various sizes [99, 40, 23, 57, 64]. Spiral breakup is now one of the most actively pursued candidates for the mechanism underlying onset of ventricular fibrillation.

The theory of restitution instability was developed assuming that the slope of the restitution curve is always positive. This assumption is reasonable as it means that longer recovery times lead to longer action potential durations as has been confirmed in numerous experimental studies. However, it was shown recently that in some cases, the slope of the restitution curve can become negative as well. For example, it was shown that the restitution curve has a region with negative slope in remodeled atrial tissue, i.e. in tissue which sustains chronic atrial fibrillation [126]. It was also shown that there is a small region with negative slope in the restitution curve of normal human ventricular tissue [35, 88]. In spite of the existence of negatively sloped restitution curves this phenomenon has hardly been studied. In the only published paper in that area known to us [109], it was found that the addition of a non-monotonous region to the restitution curve can result in increased instability of the pulse rotating in a ring of the cardiac tissue. However, mechanisms underlying this effect as well as the precise role of the non-monotonicity in the loss of stability were not clear.

In this article, we study the effects of negatively sloped restitution in several contexts whose study lead to a good understanding of the alternans instability: a periodically forced excitable cell, circulation of a pulse in a ring, and spiral wave rotation in two dimensions. Our main conclusion is that negative restitution can induce instabilities if the slope of the restitution curve is steeper than -1.

3.2 Periodic Forcing of an Excitable System

We start with a simple analysis. Consider stimulating an excitable cell with a constant period T and denote the action potential durations of the successive pulses as APD_n and their diastolic intervals as DI_n. Because the period of stimulation is constant, $APD_n + DI_n = T$. The action potential duration of the pulse APD_{n+1} is determined by the previous diastolic interval, or

$$APD_{n+1} = f(DI_n) = f(T - APD_n), \tag{3.1}$$

where f stands for the restitution properties. The dynamics of this map can be easily studied. An equilibrium point of this map corresponds to a periodic response of the excitable medium. Such an equilibrium becomes unstable, however, as soon as $|\frac{df}{dDI}| > 1$. The case $\frac{df}{dDI} > 1$ corresponds to the alternans instability discussed in [94, 45], the case $\frac{df}{dDI} < -1$ corresponds to a new instability which is induced by negative restitution. Therefore, if the slope of the restitution curve becomes steeper than -1, we can expect instabilities in the excitable medium.

A useful graphical representation of possible dynamics in this case is shown in Fig. 3.1. The solid lines represent restitution curves. In order to obtain the dynamics of map (3.1) under periodic forcing one should draw a straight line $APD = T - DI$ and perform the well-known "cobwebbing"-method with respect to this line (similar to [94, 124].

Fig. 3.1a shows an example of a restitution curve with everywhere negative slope. The dashed line represents forcing with one possible period. We see that, in this case, the map defined by (3.1) has a stable equilibrium B at a long DI and an unstable equilibrium A at a short DI. We see that the solution perturbed from the stable equilibrium B returns to it without oscillations (no alternans) and there is a basin of attraction of this equilibrium: if one perturbs the system to a DI shorter than that given by point A, the series of APDs goes to infinity. If we decrease the period of forcing, the

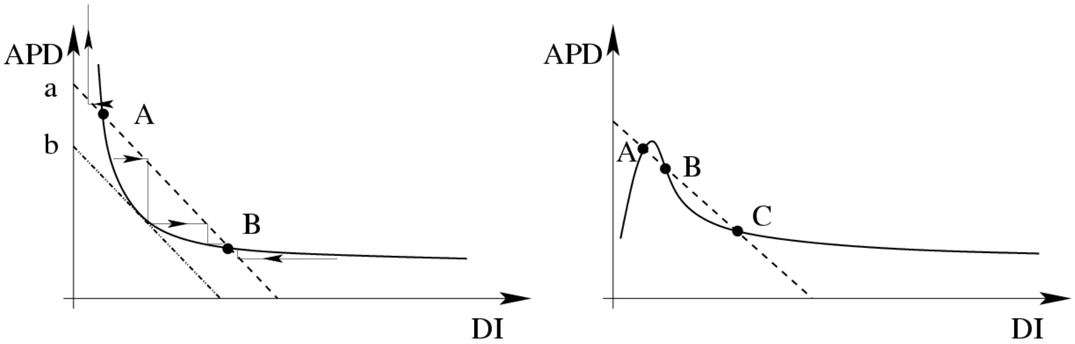

Figure 3.1: Qualitative dynamics in an excitable medium with negatively sloped APD restitution. Points of intersection of the restitution curve (the solid line) and the dashed and dotted lines a and b, defined by the relationship $APD = T_{a,b} - DI$ give the equilibria of map (3.1).

dashed line shifts downward. As a result, the equilibria A and B approach each other and the basin of attraction of equilibrium B shrinks. Further decrease in the period of external forcing results in the disappearance of the equilibria via a saddle-node bifurcation at some period which corresponds to the dot-dashed line in Fig. 3.1. The obvious condition for the saddle-node bifurcation is given by the following pair of equations:

$$\frac{dAPD(DI^*)}{dDI} = -1, \tag{3.2}$$

$$T = APD(DI^*) + DI^*, \tag{3.3}$$

where DI^* is the equilibrium value of DI.

If the restitution curve is non-monotonous and has regions of negative as well as of positive slope (Fig. 3.1b), map (3.1) can have three equilibria: a stable equilibrium C, an unstable equilibrium B, and an equilibrium A which can be either stable or unstable. If both equilibria A and C are stable, we can obtain two different stable durations of the action potential at *the same forcing period*. Note, however, that three equilibria are possible only if the restitution curve has a region with slope steeper than -1. As in the previous case, changing of the period of forcing results in disappearance of either equilibria A and B or of equilibria B and C via a saddle-node bifurcation.

Therefore, our conclusion is that periodic forcing of an excitable medium with negatively sloped restitution curve can result in instability if the slope of the restitution curve is steeper than -1. In this case, the APD is not alternating but monotonously increasing. Note, that if due to this instability the refractory period of cardiac tissue becomes longer than the period of forcing, Wenckebach blocks [125] can occur and produce quite complex dynamics. These dynamics can potentially be studied using map (3.1).

In the next section we study effects of a negatively sloped restitution curve on propagation of periodic waves: circulation of excitation in a ring of excitable tissue with negatively sloped restitution.

3.3 Circulation in a Ring

Consider a pulse circulating in a ring of excitable medium with negatively sloped restitution. If circulation is stationary, we can find its characteristics from the solution of the following equation:

$$\frac{L}{c(DI^*)} = APD(DI^*) + DI^*, \tag{3.4}$$

where L is the length of the ring, and $c(DI)$ is the dispersion relation (dependency of the velocity on DI), and $APD(DI)$ is the restitution of curve cardiac tissue.

The only difference between Eq. (3.1) and (3.4) is that while the left hand side of Eq. (3.1) is constant ($T = \text{const}$), that of Eq. (3.4) is a function of DI: $(\frac{L}{c(DI^*)})$.

We can easily find spatially uniform equilibria of (3.4) using a graphical method similar to that of Fig. 3.1. For that, as in Fig. 3.1, we first need to draw the restitution curve. Then, however, instead of drawing the straight lines $APD = T - DI$, we need to draw the curves $APD = \frac{L}{c(DI)} - DI$. Because in normal conditions velocity c is a monotonously increasing function of DI, the dashed lines $APD = \frac{L}{c(DI)} - DI$ become curves and their slopes become steeper at small DI. Graphically, this means that these lines curve upwards from the straight dashed lines in Fig. 3.1. The patterns presented in Fig. 3.1 will, however, remain the same qualitatively: For the monotonously decreasing restitution curve from Fig. 3.1a, we can expect two equilibria, for the non-monotonous restitution curve from Fig. 3.1b we can expect three equilibria, etc. These spatially uniform solutions will also disappear via a bifurcation similar to the saddle-node bifurcation shown in Fig. 3.1a. The following condition for this bifurcation is, however, slightly different from (3.2):

$$\frac{dAPD(DI^*)}{dDI} = -1 - \frac{L}{c^2(DI^*)}\frac{dc(DI^*)}{dDI}. \tag{3.5}$$

Because $\frac{dc(DI^*)}{dDI}$ is assumed to be positive, bifurcation in this case occurs for slopes of the restitution curve steeper than -1.

Let us study the stability of these spatially uniform solutions. Our analysis of this problem uses the method developed in [20] with some modifications to account for the negative slope of the restitution curve. Assume that we have an excitory pulse revolving in a ring of the length (L) and that the velocity of the wave (c) and duration of the pulse (APD) depend on DI only. Such a pulse can be described by the following delayed integral equation:

$$\int_{x-L}^{x} \frac{ds}{c(DI(s))} = DI(x) + APD(DI(x-L), \tag{3.6}$$

where x is the space coordinate along the ring. This equation basically equates the time of wave rotation around the ring at point x: $\int_{x-L}^{x} \frac{ds}{c(DI(s))}$ to the sum of the diastolic interval and APD at this point: $DI(x)+APD(DI(x-L))$.

Assume that this equation has a spatially uniform solution, (3.4), corresponding to a steady traveling pulse of excitation. The stability of this solution can be found by computing the growth factor, Q, of the perturbation

$$DI = DI^* + be^{Qx/L}, \tag{3.7}$$

which, after substitution of (3.7) into (3.6), yields the following eigenvalue problem [20]:

$$e^Q = \frac{A+QB}{A+Q}, \tag{3.8}$$

where $A = \frac{L}{c(DI^*)^2}\frac{dc}{dDI}(DI^*)$, and $B = -\frac{dAPD}{dDI}(DI^*)$.

We study this equation in the case of a negatively sloped restitution curve ($B > 0$) and a normal dispersion curve ($A > 0$).

First, following [20], let us prove that if $0 < B < 1$, the real part of Q cannot be positive and therefore the circulation is stable. In fact, if we assume that $Re(Q) > 0$, then, on one hand, the modulus of the left hand side of (3.8) is greater than one ($|e^Q| > 1$). On the other hand, $|A + QB| < |A + Q|$ and the right hand side of (3.8) is less than 1. Therefore, we have a contradiction which proves that for $0 < B < 1$ the circulation of the pulse in the ring is stable.

Now, assume $B = 1$. In that case we have infinitely many roots of (3.8) with $Re(Q) = 0$, which are:

$$Q_k = i2\pi k; \quad k = 0, 1, 2, .. \text{ etc.} \tag{3.9}$$

and a real root $Q = -A$, which for normal dispersion curve ($A > 0$) is negative and cannot contribute to the instability.

Now let us show that if $B > 1$, the pulse becomes unstable. To do this, we find the dependency of Q_k on B close to the point $B = 1$. In this case, we can assume that $Q_k(B) \equiv \alpha_k(A, B) + i\beta_k(A, B)$ is a differentiable function of A, B and find its derivatives at $B = 1$:

$$\frac{\partial \alpha_k}{\partial B} = \frac{4\pi^2 k^2}{A^2 + 4\pi^2 k^2}, \quad \frac{\partial \beta_k}{\partial B} = \frac{2\pi A k}{A^2 + 4\pi^2 k^2}; \tag{3.10}$$

$$\frac{\partial \alpha_k}{\partial A} = \frac{\partial \beta_k}{\partial A} = 0 \tag{3.11}$$

This yields the following linear approximations close to $B = 1$ for the wavelengths of the perturbations $\Lambda_k = \frac{2\pi L}{\beta_k}$ and their increments α_k:

$$\alpha_k \approx \frac{4\pi^2 k^2 (B-1)}{A^2 + 4\pi^2 k^2}; \quad \Lambda_k \approx \frac{L}{k}(1 - \frac{A(B-1)}{A^2 + 4\pi^2 k^2}) \tag{3.12}$$

We see that $\alpha_k > 0$ if $B > 1$, hence the pulse becomes unstable if the slope of restitution curve becomes steeper than -1 and the growth rate of perturbations near the bifurcation is fastest for the perturbations with the shortest wavelengths.

To validate the results of these analytical computations, we performed computations using equation (3.6) with

$$APD(DI) = a + \frac{\alpha}{DI} \ , c(DI) = \beta \cdot DI \tag{3.13}$$

and parameter values $a = 10, \alpha = 50, \beta = 1$. DI was assumed to be non-negative. For such choice of functions, equation (3.6) has just one spatially uniform equilibrium point ($L^* = DI^{*2} + 10DI^* + 50$), which becomes unstable

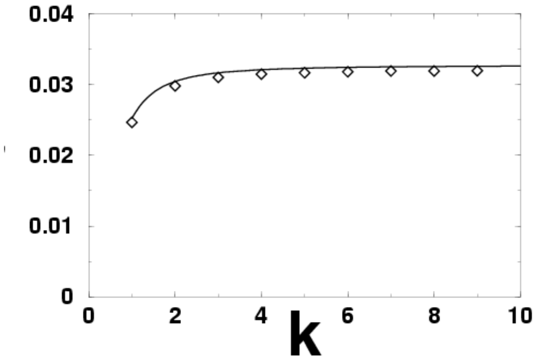

Figure 3.2: Growth factors of perturbations with initial amplitude $A = 10^{-4}$ in a ring of the length $L = 168$. Computations were done using Eq. (3.6) with functions given in (3.13), and $a = 10, \alpha = 50, \beta = 1$. Further explanations are in the text.

for $L < 170.71$. We set DI to this fixed point of Eq. (3.6) everywhere in the ring and then imposed perturbations of the form $DI = DI^*(1 + A * \sin(kx))$. Fig. 3.2 compares the growth factors of perturbations of different wave numbers k. Numerical and analytical results match almost exactly.

What type of bifurcation do we have at $B = 1$; what is the direction of this bifurcation? Unfortunately, it was not possible to perform a non-linear analysis similar to [20]. This is because, for roots (3.7) of the characteristic equation (3.8), non-linear amplitude terms in asymptotic expansions of (3.6) disappear, which makes the problem highly degenerate. Therefore, we studied the behavior of our system around the bifurcation point numerically using equation (3.6) with parameters as in Fig. 3.2. We have determined the basin of attraction of the spatially uniform equilibrium point of this equation close to the bifurcation point at $L = 170.71$. For this, we added spatially uniform perturbations to the exact solution, and checked whether the system returns to equilibrium (Fig. 3.3). We see that the basin of attraction of the stable solution decreases and becomes zero when we approach the bifurcation point. In all cases the solution becomes unstable without alternans: we observe the successive shortening of DI until the pulse fails to propagate.

Thus, our conclusion is that if the slope of the restitution curve is steeper than -1, a revolving pulse on a ring of excitable tissue is unstable. By "the

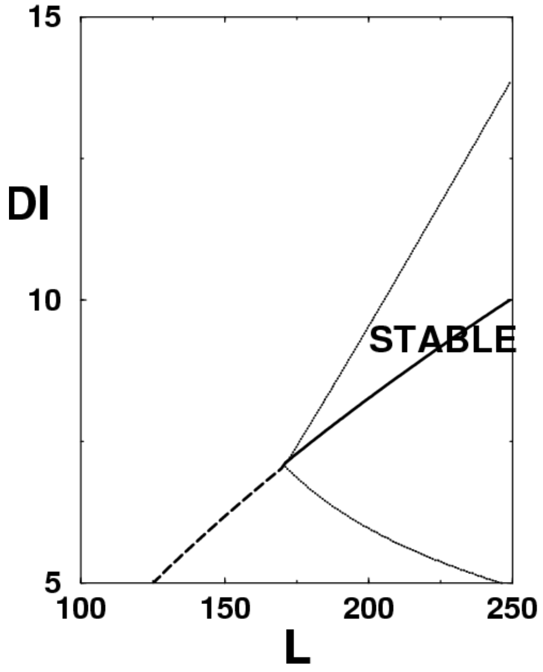

Figure 3.3: Bifurcation diagram of spatially uniform solution for pulse circulating in a ring of excitable tissue. L is the ring length, DI is the diastolic interval, thin lines show the basin of attraction of the equilibrium (thick line, solid for stable, dashed for unstable) with respect to spatially uniform perturbations. See the text for further explanation.

slope of the restitution curve", we mean the slope evaluated at the DI^* corresponding to this pulse. Note that the conditions for this instability coincide with the conditions for instability of a pulse under periodic external forcing considered in section 3.2.

3.4 Spiral Waves in Excitable Media with Negative Restitution

We study numerically the dynamics of spiral waves in an excitable medium with negative restitution. For our study we use two models of an excitable medium: a cellular automaton and a reaction-diffusion model. Our main conclusions are: there are no significant effects of negative restitution as long as the slope of the restitution curve is less steep than -1. In media with slopes steeper than -1, the dynamics of spiral waves can significantly change: (1) the average restitution time jumps to a value where the slope of the restitution curve is about -1; (2) spiral waves can break up into turbulent patterns. We discuss a possible connection between such instabilities and fibrillation in atrial tissue.

Rotating spiral waves occur in a wide variety of non-linear excitable media [132]. While spiral waves may be stable under certain conditions, they can also break up into turbulent patterns. In the case of the heart, spiral waves cause tachycardia, a dangerous cardiac arrhythmia associated with a rapid heart beat [3, 25]. Tachycardia can deteriorate into fibrillation, which is fatal if it occurs in the ventricles of the heart, or a serious complication if it occurs in the atria. One possible mechanism of such deterioration is spiral breakup [99, 57, 23, 98, 64, 110, 111].

It was shown that spiral breakup heavily depends on a property of the excitable medium called its restitution curve [19]. The restitution curve of a medium is the dependency of some pulse characteristic on the restitution time, which is the interval between the start of a pulse and the end of the previous pulse. Often the measured characteristic of the pulse is its duration (called action potential duration or APD in the case of cardiac tissue), which yields the APD restitution curve. Another important pulse characteristic is its refractory period (RP), which is the time interval during which a cell cannot be excited after a previous excitation; this leads to the RP restitution curve. In cardiac tissue, the RP and APD restitution curves are similar. Under normal conditions, longer restitution times lead to longer pulse durations and refractory periods, so that the restitution curve has positive slope everywhere. In this case, it has been shown that instabilities, e. g. spiral breakup, can occur if the slope of the restitution curve is steeper than 1 [19].

Experiments show that the slope of the RP restitution curve of cardiac tissue can become negative (we call this negative restitution) [35]. In the case of atrial tissue, negative restitution has been observed in healthy animals, and it became even more pronounced under pathological conditions (chronic atrial fibrillation) [126]. It was also shown in a modeling study that even a small degree of negative restitution can be important for wave propagation in a ring of excitable tissue [109]. In spite of the existence of negative restitution in cardiac tissue, the influence of negative restitution on spiral wave dynamics has not yet been studied.

In this Chapter, we study numerically how negative restitution can affect spiral wave dynamics. We are interested in general mechanisms; therefore, we look at restitution curves that are simple rather than realistic for heart tissue.

We developed two types of models of an excitable medium with negative restitution: a cellular automaton model (CA) and a reaction-diffusion type model (RD). Both types of description of excitable media — CA [57] and RD [99, 23, 98, 63] — have successfully been used to study spiral breakup in media with positive restitution.

CA model. — We modified a cellular automaton model [139] in a way that allows us to directly input the restitution curve. In our model, each cell can be in one of the following three states: resting, excited, or refractory. If a cell is in the rest state, we look at every time step whether one of its eight closest neighbors is in the excited state. If so, we increase an inner variable called excitation counter by 1 for each excited neighbor at each time step. If the excitation counter exceeds a predefined threshold (th), the cell switches to the excited state. In the excited state, a cell can excite its neighbors for a constant number of time steps (t_{ex}) and then switches to the refractory state, where it again stays for a constant number of time steps. At the end of the refractory state, the cell switches back into the rest state. The "action potential" in the CA model is therefore fully characterized by the times at which the cell is excited and at which it returns to rest state, and the shape of the action potential can be considered rectangular.

Now we make the restitution curve of the CA model non-constant. To achieve that, we need the duration of the refractory period to depend on the time spent in the rest state before excitation. In the CA model, the refractory period (t_{ref}) is the sum of the times spent in excited and refractory state. So by letting the duration of the refractory state depend on the restitution time, an arbitrary restitution curve can be forced upon the model. In our simulations, we always used $t_{ex} = 10$ and $th = 19$.

RD model. — We also used a reaction-diffusion model of FitzHugh-Nagumo type piecewise linear "Pushchino kinetics"[102]:

$$\begin{aligned}\frac{\partial e}{\partial t} &= \frac{\partial^2 e}{\partial x^2} + \frac{\partial^2 e}{\partial y^2} - f(e) - g \\ \frac{\partial g}{\partial t} &= \varepsilon(e,g)(e-g),\end{aligned} \tag{3.14}$$

where e is the transmembrane potential and g is the gate variable. In order to make the shape of the action potential as simple as possible, we used the following nonlinear function $f(e)$ [65]: $f(e) = \lim_{C\to\infty} Ce$ when $e < 0$, $f(e) = (e - 0.1)$ if $0 \leq e \leq 1$, and $f(e) = \lim_{C\to\infty} C(e-1)$ when $e > 1$. For this shape of $f(e)$, the excitation pulse has a plateau region at $e = 1$, the rest state at $e = 0$, and the shape of the pulse is close to rectangular. To model the regions of infinite slope of function $f(e)$ numerically we use the `if` operators stating that if the variable e is above 1 it is set to 1, and if $e < 0$, it is set to 0. It was shown that this procedure gives a sufficiently precise solution of Eq. 3.14 with f as given above [101]. In our basic model, $\varepsilon(e,g) = 0.067$ if $0.1 < e < 0.99$ and $\varepsilon(e,g) = 0.1$ for other values of e. Such a model has an almost flat restitution curve (the solid line in Fig. 3.4). In order to describe a medium with negative restitution, we made the function $\varepsilon(e,g)$ dependent on the restitution time. We put $\varepsilon(e,g) = T^{-1}(t_r)$,(if $0.45 \leq g \leq 0.55$ and $e < 0.1$), where t_r is the restitution time, and $T_{RD}(t_r)$ is the function, using which we set up the desired restitution curve. In fact, if $0.45 \leq g \leq 0.55, e < 0.1$, the excitable medium is in the refractory state and the time interval during which the variable g decreases from $g = 0.55$ to $g = 0.45$, is given by $T_{RD}(t_r) \ln \frac{0.55}{0.45}$. Therefore, by choosing the function $T_{RD}(t_r)$, we can construct an excitable medium with any desired dependence of the refractory period on t_r.

For numerical modeling of Eq. 3.14, we used the explicit Euler method with Neumann boundary conditions and a rectangular grid. Numerical integration was performed with a space step $h_s = 0.6$ and a time step $h_t = 0.03$. The error in these computations, estimated using the difference between the computed and the analytically found velocity of plane wave propagation [65], was about 5%.

To initiate the spiral wave we used in both models initial data corresponding to a 2D broken wave front, or alternatively the S_1S_2 stimulation protocol, which is often used in experimental electrophysiology [16]. Note that we chose the parameters of the CA model such that spirals closely match those in the RD model. We characterize spirals by their average restitution time (ART). To find ART we first compute the restitution times at each point of excitable medium and find their spatial average. The restitution times were evaluated as the time the point spent in rest state prior to the preceding excitation. The rest state in RD model was determined as the time between the end of the refractory period and the next excitation. The refractory period was estimated to be the time interval from the beginning of excitation until the moment of time when the variable g reaches the value $g = 0.45$ at the wave back.

Results. — We start with a simple analysis. Consider stimulation of an excitable medium with a constant period T and denote the refractory periods of the successive pulses as $(t_{ref})_n$ and their restitution times as $t_{r,n}$. Because the period of stimulation is constant, $(t_{ref})_n + t_{r,n} = T$. The refractory period of the pulse $t_{ref,n+1}$ is determined by the previous restitution time, or $t_{ref,n+1} = f(t_{r,n}) = f(T - t_{ref,n})$, where f is the restitution curve, and the dynamics are given by iteration of this discrete map. A fixed point of this map corresponds to a train of pulses of equal length. Such a fixed point is unstable whenever $|\frac{df}{dt_r}| > 1$ [19]. The case $\frac{df}{dt_r} > 1$ corresponds to the positive restitution studied earlier, $\frac{df}{dt_r} < -1$ corresponds to negative restitution. Therefore, we expect instabilities for negative restitution if the slope becomes steeper than -1.

In order to study the effect of negative restitution on spirals wave dynamics in our CA model, we first induced a spiral wave in a medium with a constant restitution curve . For our CA model parameters, ART = 20; this value is marked on the restitution curve (square in Fig. 3.4abducted). Then we generated a family of restitution curves that all go through this location ($t_r = 20$, $t_{ref} = 76$) but have slopes between 0 and -1.5. These restitution curves are linear up to $t_r = 50$ time units and constant for $t_r > 50$ time units. Three examples of such restitution curves together with the computed location of spirals are shown Fig . 3.4a. Note, that because all restitution curves go through the point $t_r = 20$, $t_{ref} = 76$, there exists a spiral wave solution with $t_r = 20$, $t_{ref} = 76$, but it does not mean that this solution is stable.

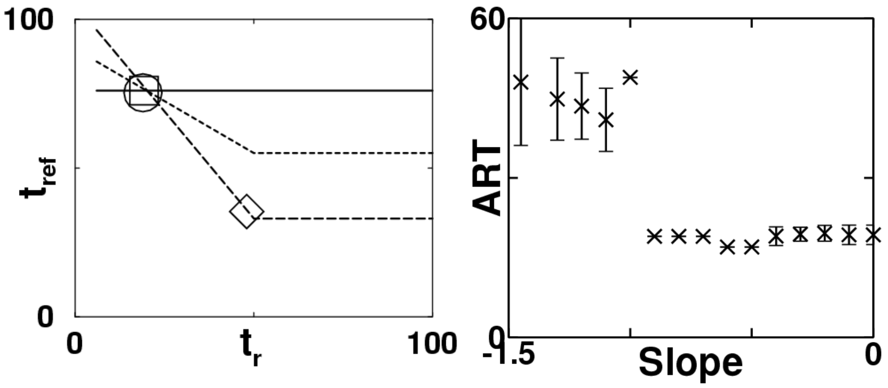

Figure 3.4: **Left**: Restitution curves used in our CA model. $t_{ref}(t_r) = 76 + (t_r - 20) \cdot \text{slope}$ for $t_r < 50$ and $t_{ref}(t_r) = 76 + 30 \cdot \text{slope}$ for $t_r \geq 50$. The restitution curves shown have slope 0 (solid), -0.7 (dashed), and -1.45 (long-dashed). Spiral locations are indicated by a square (for slope 0), a circle (slope -0.7), and a diamond (slope -1.45).
Right: The range of average restitution times (ARTs) vs. slopes. The error bars show the standard deviations, but they are smaller than the symbol size for slopes less steep than -1. Medium size was 40x40.

From Fig. 3.4a we see that for slopes 0 and -0.7 the spiral location is close to the spiral location for a constant restitution curve, but for slope -1.45, it is considerably shifted to the right. The complete dependency of the spiral location on the slope is shown in Fig. 3.4b. We see that for slopes less steep than -1, the ART remains almost the same as for the constant restitution curve, with only small standard deviations in the ART. For slopes steeper than -1, the ART jumps to much higher values. The ART is then close to 50, the value at which the oblique segment of the restitution curve ends. Also, for slopes steeper than -1, ART has a larger standard deviation. This reflects the non-stationarity of spirals which we observe for such restitution curves. For slopes steeper than -1.15 we frequently observed breakup, which was more pronounced for still steeper slopes. In some cases, the spirals disappeared at the boundary.

We did similar computations in the RD model. By choosing functions $T_{RD}(t_r)$, we generated a family of restitution curves similar to those used in the CA model (see Fig. 3.5a). We see that as for the CA model, the ART of a spiral wave is almost unchanged for the restitution curves with slopes

0 and -0.7 and it is shifted to the right for slope -1.4. We also see that the dependency of ART on the slope in the RD model (Fig. 3.5b) is similar to that in the CA model, but there are some differences: First, the rise of ART in the RD model is less abrupt; Second, the breakup of spirals for slopes steeper than -1 is not as pronounced as in the CA model.

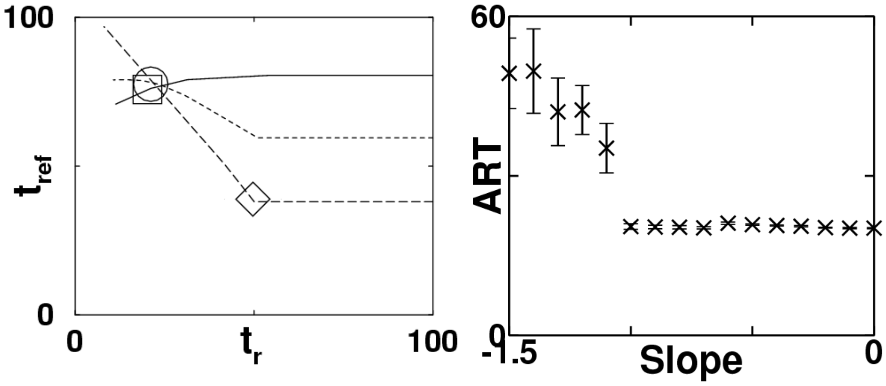

Figure 3.5: Restitution curves and corresponding range of average restitution times in the RD model. Restitution curves were set up using $T_{RD}(t_r) = 300 + 5(t_r - 20) \cdot \text{slope}$ for $t_r < 50$ and $T_{RD} = 300 + 150 \cdot \text{slope}$ for $t_r \geq 50$. Medium size was 300x300, the meaning of symbols is the same as in Fig. 3.4.

In our view, this shift of ART can be explained by the following simple consideration. It is reasonable to assume that spiral waves tend to minimize their period. Usually, this results in the selection of the smallest possible distance between the wave front and wave back in a spiral. In physiology such distance is called *excitable gap*, in our case it is just the restitution time. However, for media with negative restitution, the minimal excitable gap (restitution time) does not necessarily mean the minimal period. Because the period of a spiral wave is $T = (t_{ref} + t_r)$, the minimum is reached at $\frac{dT}{dt_r} = 0$, $\frac{d^2T}{dt_r^2} > 0$, which implies $\frac{dt_{ref}}{dt_r} = -1$, $\frac{d^2t_{ref}}{dt_r^2} > 0$. So, according to the period minimization principle, for a restitution curve with everywhere positive second derivative, the spiral should choose an ART for which the slope of the restitution curve is -1.

Although the results shown in Fig. 3.4 and 3.5 are consistent with this explanation, they are not conclusive because the slope jumps discontinuously and takes on only two values for each restitution curve. Therefore, we studied a medium whose restitution curve has continuously varying slope. For both CA and RD models, we generated a restitution curve which is constant for $t_r > 53.2$ and a parabola for $t_r < 53.2$, such that the slope is -1 at $t_r = 38.2$. We initiated a spiral wave in such a medium and found its ART (Fig. 3.6a). We see that the spiral indeed chooses an ART close to the point where the restitution curve has slope -1 (arrow) in both models. We also performed a series of computations in which we shifted the parabola. The results are presented in Fig. 3.6b, the straight line shows the value of ART at which the restitution curve has slope -1. We see that for both models, the time average of the ART is always in the region where the slope is less steep than -1 (above the solid line). In the RD model, the average ART is almost exactly at slope -1, in the CA model, there are some deviations towards larger ARTs. Therefore, we conclude that spiral waves tend to avoid the regions where the restitution curve has slopes steeper than -1 by choosing an ART value at which the slope of the restitution curve is close to and less steep than -1.

Another important phenomenon which may occur in media with negative restitution is spiral breakup into a complex turbulent pattern. Fig. 3.7 shows examples of such patterns which occur in CA and RD models with parabolic restitution curve. In the CA model the breakup typically occurs in the following way. At some region of the spiral, the excitable gap becomes rather small, leading to a longer duration of the next excitation (due to the negative restitution). This leads to progressively smaller excitable gaps (which can be seen in Fig.3.7a, first subfigure). Finally, the wave front breaks; in case of Fig. 3.7a, this occurs close to the core of the spiral wave. The open ends of the broken front form new spirals, which in turn break up further, resulting in patterns presented in Fig. 3.7a.

In the RD model, the effects are similar (see Fig. 3.7b), however, the regions of instability are not as regular as in the case of CA model. The breakup again occurs close the core of the spiral.

Note that the breakup in the RD model is in general substantially less pronounced than in the CA model. In fact, we have observed a very limited breakup for the parabolic restitution curve from Fig. 3.6a and in order to generate a picture comparable to the CA model we increased the curvature of the parabola by a factor of 2.

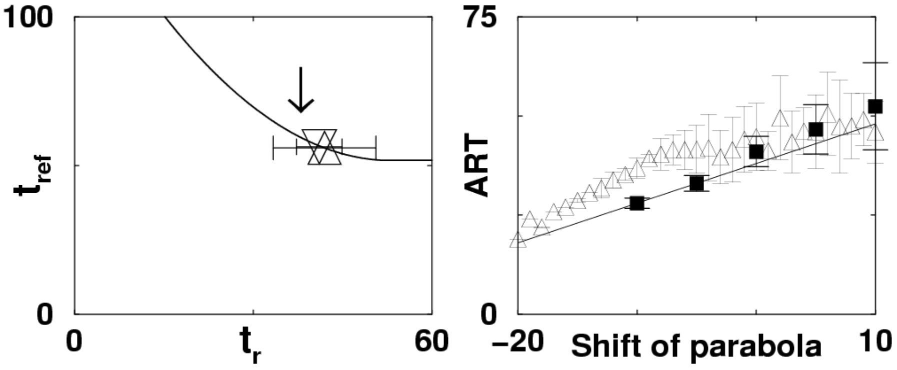

Figure 3.6: Spiral in a medium with a parabolic restitution curve. **Left:** RD and CA restitution curves are very similar. For better readability, we show only CA restitution curve: $t_{ref} = \frac{(TR_0 - t_r)^2}{30} + 51.7$ for $t_r < TR_0$ and $t_{ref} = 51.7$ for $t_r \geq TR_0$; RD restitution curve is: $T_{RD} = \frac{(TR_0 - t_r)^2}{6} + 150$ for $t_r < TR_0$ and $T_{RD} = 150$ for $t_r \geq TR_0$ with $TR_0 = 53.2$. The arrow shows where the restitution curve has slope -1. The time averages of the (spatial) average restitution times are indicated by an upward triangle (CA) and a downward triangle (RD). Error bars indicate standard deviations, the large error belongs to the CA model. Medium size was 80x80 (CA) and 300x300 (RD). **Right:** Average restitution time as a function of parabola shift. The value of $TR_0 = 53.2$ is replaced by $TR_0 = 53.2 +$ (Shift of parabola). The corresponding average restitution times are represented by triangles for the CA model and by squares for the RD model. Error bars indicate standard deviations in time. The solid line shows which ART corresponds to slope -1 in the restitution curve.

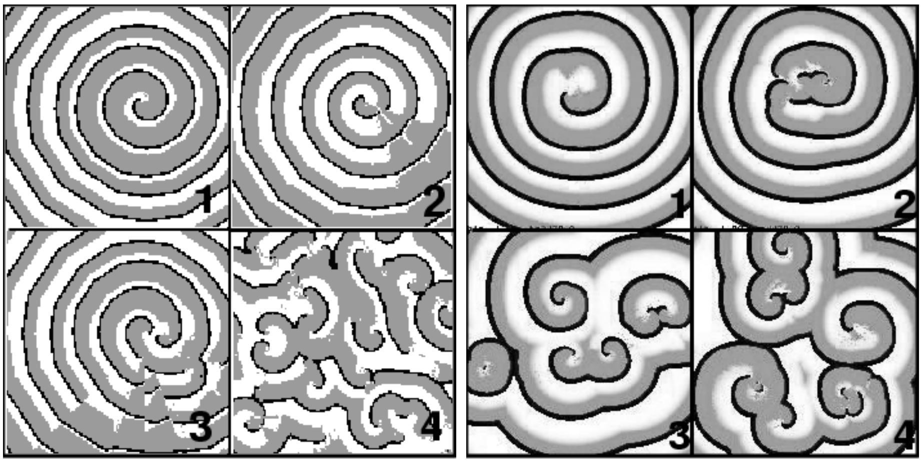

Figure 3.7: Spiral breakup for negative restitution. **Left**: in the CA model, with restitution curve from Fig. 3.6a, after 97, 101, 110, and 475 spiral periods (medium size 160x160). We show only the central 120x120 points of the medium to have the same scaling as in the right image. **Right**: in the RD model, with the restitution curve $T_{RD} = \frac{(53.2-t_r)^2}{3} + 150$ for $t_r < 53.2$ and $T_{RD} = 150$ for $t_r \geq 53.2$, after 22, 43, 145, and 211 spiral periods (medium size 721x721).

3.5 Discussion

This Chapter discusses general effects of negatively sloped restitution curve on stability of wave propagation in excitable media. The main conclusion is that instabilities occur if the slope of the restitution curve is more negative than -1. The manifestation of this instability is different from the alternans instability which occurs if the slope of the restitution curve is positive and steeper than 1. In fact, under periodic forcing, the negative slope restitution instability is associated with a saddle-node bifurcation, and results in successive (unbounded) increase of APD, while the alternans instability is associated with a supercritical flip bifurcation and results in APD oscillations. For a pulse circulating in a ring of excitable medium described by the delayed integral equation (3.6), negative restitution instability corresponds to an infinite-dimensional bifurcation (as infinitely many roots of the characteristic equation cross into the right half-plane). Linear analysis has also shown that the modes with the highest spatial frequency have the largest growth factors. The numerical studies showed similarity of this bifurcation with a subcritical Hopf bifurcation. In contrast, the alternans instability occurs via a supercritical infinite-dimensional Hopf bifurcation [20]. In two-dimensional excitable media with negatively sloped restitution curve the breakup of spiral waves is in some way less pronounced than the breakup known in media with positive restitution. The main difference is that in media with negative restitution, breakup takes quite a long time to develop (tens of rotations), compared to just a few rotations in the case of positive restitution curves [98]. This may be a consequence of the effect found in this paper: shifting of spiral DI to the region where the slope of the restitution curve is -1. In fact, a slope of -1 is the value at which instability first occurs and therefore the growth rate of the instabilities is minimal, which may explain their slow development. Quite differently, in media with positive restitution, the shift of DI is absent and the spiral is usually located in the region with slope much steeper than 1 [97], which results in faster growth of instabilities and faster breakup of spirals.

Still, the effect of DI shifting to the point where the slope equals -1 might in certain situations promote spiral breakup. In fact, this shift should be observed not only for restitution curves with everywhere negative slope, but also for restitution curves whose slope is negative just in a small interval. In such a case, the shift can potentially move the spiral from the region where breakup is absent to the region of slope -1 where breakup is possible.

In conclusion, we have shown that the negatively sloped restitution curve can result in various instabilities for periodically forced systems and for one and two-dimensional wave propagation in excitable medium. These instabilities can be expected if the slope of the restitution curve is more negative than -1.

Chapter 4

Waves Propagation in Second-Generation Ionic Models of Cardiac Tissue

Recently, it has been shown that cardiac cell models accounting for changes in intracellular ionic concentrations ("second-generation models") have widely been used in a way that violates charge conservation. This problem was tackled by directly or indirectly imposing charge conservation for the case of single cells. In this Chapter, we study the effects of charge conservation violation on wave propagation. We show that the effect of charge conservation violation is small in homogeneous media, but may become significant in heterogeneous media. We conclude by proposing a proper method of simulating wave propagation in second-generation models, given the present understanding.

4.1 Introduction

Excitable cells have first been modeled quantitatively in the seminal paper by Hodgkin and Huxley on the giant squid axon [55]. Hodgkin and Huxley viewed the cell as a capacitor and its ionic channels as variable resistors. In the following decades, new ionic channels were discovered and the characterizations became much more precise [82, 7, 77]. A fundamental shift in model development was making intracellular ion concentrations state variables. Models with this feature are called "second generation" models

[26, 78].

Second-generation models are now generally accepted to be an important tool for studying the electrophysiology of excitable cells. However, recent findings show that they suffer from a mathematical deficiency [117]. The problems arise from the fact that the equations of second-generation models are linearly dependent, or stated differently, that transmembrane voltage (V_m), although treated as an independent variable, is a function of the intracellular ion concentrations.

This defect leads to a number of artifacts. For example, rest states of second-generation models are not unique but depend on the initial conditions of a simulation. A closely related problem is that external pacing may lead to drifts in intracellular concentrations and V_m.

As countless studies of single cells and of wave propagation have already been carried out using second-generation models, the question of how reliable their results are needs to be addressed. Also, researchers need to know what is the best way to design future simulation studies.

Regarding single cell simulations, new models have been developed recently that enforce charge conservation by eliminating V_m as an independent variable but expressing it as a function of the intracellular ion concentrations [117]. In particular, Endresen et al. showed that this removes the dependency of the limit cycle on initial conditions in a model of the sinusatrial mode [30]. In a different approach, Hund et al. [56] showed that in the Luo-Rudy dynamic model [78] unphysiological drifts can be avoided if all stimulation currents are actually carried by ions ("specific" stimulation).

All studies listed above were performed for the excitation of a single cardiac cell. The most important application of these model is, however, to wave propagation, which we study for the first time in this Chapter. The main new problem is that the equation that has since Hodgkin and Huxley [55] been used for wave propagation contains a voltage diffusion term which results in a violation of charge conservation in second generation models. We show that the effect of these unspecific currents is minimal for homogeneous media, but for heterogeneous media, it can lead to errors of significant size. Finally, we extend the work of [117, 30] to propose an appropriate method for future studies of wave propagation in second generation models of excitable tissue.

4.2 Methods

For numerical simulations, we use the Luo-Rudy model (LR) of the ventricular mammalian myocyte [78, 136, 32], if not stated otherwise. In every time step, ionic currents through ion channels, pumps, and exchangers are updated according to model equations. From these ionic current, the changes in ionic concentrations are computed in the following way:

$$\begin{aligned}
\partial_t[K^+]_i &= -\frac{A_{cap}C_m}{V_{myo}F}[I_{K,t} - 2I_{NaK}] && (4.1)\\
\partial_t[Na^+]_i &= -\frac{A_{cap}C_m}{V_{myo}F}[I_{Na,t} + 3I_{NaK} + 3I_{NaCa}] && (4.2)\\
\partial_t[Ca^{2+}]_i &= -\frac{A_{cap}C_m}{V_{myo}F}[I_{Ca,t} - 2I_{NaCa}] && (4.3)\\
& \quad -\frac{V_{nsr}}{V_{myo}}[I_{up} - I_{leak}] + \frac{V_{jsr}}{V_{myo}}I_{rel}] && (4.4)\\
\partial_t[Ca^{2+}]_{jsr} &= I_{tr} - I_{rel} && (4.5)\\
\partial_t[Ca^{2+}]_{nsr} &= I_{up} - I_{leak} - \frac{V_{jsr}}{V_{nsr}}I_{tr}. && (4.6)
\end{aligned}$$

Here, $I_{K,t}$, $I_{Na,t}$, and $I_{Ca,t}$ are sums of all currents in the LR model through K^+, Na^+, and Ca^+ channels, respectively. See Table 4.1 for definitions of symbols.

In the absence of stimulation, we update V_m according to the traditional scheme:

$$\begin{aligned}
\partial_t V_m &= -I_{tot} && (4.7)\\
I_{tot} &= I_{K,t} + I_{Na,t} + I_{Ca,t} + I_{NaK} + I_{NaCa}. && (4.8)
\end{aligned}$$

At times when there is stimulation, we set

$$I_{tot} = I_{K,t} + I_{Na,t} + I_{Ca,t} + I_{NaK} + I_{NaCa} + I_{Stim}. \qquad (4.9)$$

If this stimulation is supposed to be *nonspecific*, we do not adapt the ion concentration. If, on the other hand, we need specific stimulation, we change an ion concentration accordingly. By default, we stimulate using potassium ions, which changes Eq. 4.1 to:

$$\partial_t[K^+]_i = -\frac{A_{cap}C_m}{V_{myo}F}(I_{K,t} - 2I_{NaK} + I_{Stim}). \qquad (4.10)$$

AP	Action potential
APD	Action potential duration
A_{cap}	Capacitative area of membrane (cm^2)
C_m	Specific membrane capacitance (μF/cm^2)
$I_{Ca,t}$	Total Ca^{2+} current through all ion channels in LR model
$I_{K,t}$	Total K^+ current through all ion channels in LR model
$I_{Na,t}$	Total Na^+ current through all ion channels in LR model
I_{leak}	Ca^{2+} leak from NSR (mM/ms)
I_{NaCa}	Na$^+$-Ca^{2+} exchanger (μA/μF)
I_{NaK}	Na$^+$-K$^+$ pump (μA/μF)
I_{rel}	Ca^{2+} release from JSR (mM/ms)
I_{tr}	Ca^{2+} release from NSR to JSR (mM/ms)
I_{up}	Ca^{2+} uptake into NSR (mM/ms)
JSR	Junctional sarcoplasmic recticulum
NSR	Network sarcoplasmic recticulum
V_{myo}	Volume of myoplasm (μl)
V_{JSR}	Volume of JSR (μl)
V_{NSR}	Volume of NSR (μl)
$[Ca^{2+}]_{i,tot}$	Intracellular concentration of bound and free Ca^{2+} (mM)
$[Ca^{2+}]_{jsr,tot}$	JSR concentration of bound and free Ca^{2+} (mM)
$[Ca^{2+}]_{nsr,tot}$	NSR concentration of Ca^{2+} (mM)
$[K^+]_i$	Intracellular concentration of K$^+$ (mM)
$[Na^+]_i$	Intracellular concentration of K$^+$ (mM)
∂_t	time derivative

Figure 4.1: Definitions of symbols used in the text

$[\mathrm{K}^+]_\mathrm{i}$	141.2 mM
$[\mathrm{Na}^+]_\mathrm{i}$	9 mM
$[\mathrm{Ca}^{+2}]_\mathrm{i}$	6×10^{-5} mM
$[\mathrm{K}^+]_\mathrm{o}$	4.5 mM
$[\mathrm{Na}^+]_\mathrm{o}$	140 mM
$[\mathrm{Ca}^{+2}]_\mathrm{o}$	1.8 mM
V_m	-90 mV
$[\mathrm{Ca}^{+2}]_\mathrm{NSR}$	1.838 mM
$[\mathrm{Ca}^{+2}]_\mathrm{JSR}$	1.838 mM

Figure 4.2: Initial values used for simulations

In one-dimensional simulations we solve the cable equation,

$$\partial_t V_m(x,t) = -I_{tot} + D\frac{\partial^2 V_m}{\partial x^2}(x,t), \tag{4.11}$$

where D is a diffusion constant. We use a forward Euler scheme with space step 0.1 mm and fixed time step of 0.02 ms. The flow that results from diffusion in each time step was either considered to be nonspecific (nonspecific diffusive current), or to be carried by potassium ions (specific diffusive current), in which case we changed $[K^+]_i$ accordingly (see Results).

For two-dimensional simulations, we used a forward Euler scheme with time step 0.02 ms for the reaction part and an alternating direction scheme with space step 0.2 mm to compute diffusion.

4.3 Results

4.3.1 Single Cells

We start by working out how nonspecific stimulation causes drift in the resting potential. Combining Eq. 4.1 – 4.6, we get the relationship between ionic concentrations and $\dot{V}_m$ (as done earlier in [117]):

$$\begin{aligned} \dot{V}_m &= \frac{V_{myo}F}{A_{cap}C_m}([\dot{K}]_i + [N\dot{a}]_i + 2[C\dot{a}]_i + && (4.12) \\ &\quad + \frac{2V_{nsr}}{V_{myo}}[C\dot{a}]_{nsr,tot} + \frac{2V_{jsr}}{V_{myo}}[C\dot{a}]_{jsr,tot}). \end{aligned}$$

Integration of Eq. 4.12 leads to (4.13)

$$\begin{aligned} V_m &= \frac{V_{myo}F}{A_{cap}C_m}([K]_i + [Na]_i + 2[Ca]_i + && (4.14) \\ &\quad + \frac{2V_{nsr}}{V_{myo}}[Ca]_{nsr,tot} + \frac{2V_{jsr}}{V_{myo}}[Ca]_{jsr,tot} + V_0), \end{aligned}$$

where V_0 is an integration constant which we set such that the initial conditions given in Fig. 4.2 are satisfied. The physical meaning of Eq. 4.14 is that charge is conserved.

A nonspecific stimulation current I_{stim} changes Eq. 4.12 to:

$$\dot{V}_m = \frac{V_{myo}F}{A_{cap}C_m}([\dot{K}]_i + [N\dot{a}]_i + 2[C\dot{a}]_i + \tag{4.15}$$

$$+\frac{2V_{jsr}}{V_{myo}}[\dot{Ca}]_{jsr,tot} + \frac{2V_{jsr}}{V_{myo}}[\dot{Ca}]_{jsr,tot}) + I_{stim}.$$

In this setting, charge is no more conserved. The size of the violation of charge conservation due to continued stimulation can be seen to be $\frac{A_{cap}C_m}{V_{myo}F}\int_0^t I_{stim}dt$, and accordingly, V_0 will shift by just this amount:

$$V_0(t) = V_0(0) + \frac{A_{cap}C_m}{V_{myo}F}\int_0^t I_{stim}dt'. \tag{4.16}$$

A shift in V_0 results in a shift of the rest state of the system. Indeed, if the system is in rest state $x^{eq}(V_0)$ for any particular V_0, Eq. 4.14 is satisfied. If V_0 is then changed to V_0', $x^{eq}(V_0)$ no more satisfies Eq. 4.14 and can therefore no more be the rest state. Instead, the ionic concentrations in Eq. 4.14 will adjust until a new equilibrium is reached. During nonspecific stimulation the V_0 will change continuously causing the rest state to drift.

We conclude that stimulation with nonspecific currents causes drift in the rest state. On the other hand, it is equally clear why specific stimulation does not lead to drift. Indeed, if we include the stimulus current from Eq. 4.10 into Eq. 4.15, it cancels out, so that V_0 is not changed and the equilibrium remains unmoved. Note that this is true for stimulation with potassium ions as well as sodium ions, or even for stimulation with a combination of potassium and sodium ions.

Let us now quantitatively investigate the effect of changing V_0 on the rest state of the system. This problem can be solved analytically using standard methods from the theory of dynamical systems. Consider an arbitrary dynamical system depending on a parameter V_0:

$$\dot{x}_i = f_i(x_j, V_0); \tag{4.17}$$

then, an equilibrium x^{eq} has to satisfy

$$f_i(x_j^{eq}, V_0) = 0, \tag{4.18}$$

and the rates of changes of the equilibrium coordinates with V_0 can be found from

$$\frac{\partial x^{eq}}{\partial V_0} = -\frac{\partial f_i}{\partial x_j}^{-1}\left(\frac{\partial f_i}{\partial V_0}\right), \tag{4.19}$$

where $\frac{\partial f_i}{\partial x_j}$ is the Jacobian of f. Alternatively, the effect of changing V_0 on the rest state can be studied numerically, by simulating a complete relaxation to

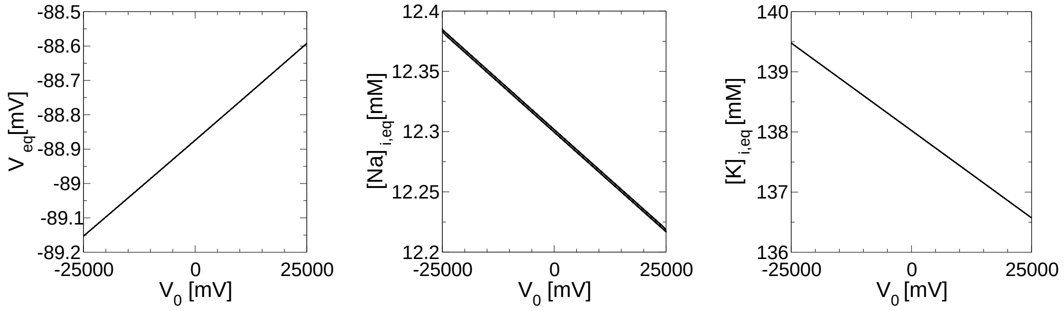

Figure 4.3: *The effect of varying the integration constant V_0 on the equilibrium of the CM model. The three graphs show different model variables (V_m, $[Na]_i$, and $[K]_i$) as V_0 is varied. V_0 was initially put to 0 and then increased by 10 mV every 5 seconds model time up to $V_0 = 5000$ mV. Then V_0 was decreased, again in steps of 10 mV every 5 seconds. This whole cycle was then repeated.*

rest state and then slowly increasing V_0, after every step giving the system sufficient time to get back into rest state again. We chose the numerical approach to gain the dependency shown in Fig 4.3.1. All dependencies are approximately linear, with a slope of $1.12 \cdot 10^-5$ for V_m, $-3.25 \cdot 10^-6$ mM/mV for $[Na]_i$, $-5.99 \cdot 10^-5$ mM/mV for $[K]_i$.

Hund et al.[56], in their Fig. 3, show how the ionic concentrations drift under long-term pacing with a non-specific current. As each stimulus leads to a shift in the integration constant, the computed dependency is analogous to ours. They get results in the same order of magnitude, but slopes differ by a factor of 4, which may be due to the fact that they use a modified Na-Ca exchanger.

We note that a change in integration constant in the order of 25000 mV changes the concentrations by less than 1% in all cases. This result will be important to assess the importance of shifts in V_0 that typically occur during wave propagation.

4.3.2 Wave Propagation

Virtually any wave propagation study using second-generation models relies on the cable equation:

$$\partial_t V_m(x,t) = -I_{tot} + D\frac{\partial^2 V_m}{\partial x^2}(x,t), \tag{4.20}$$

where the diffusion constant $D = \frac{1}{\rho_s S C_m}$, with ρ_s the resistivity of the cable, S its surface to volume ratio and C_m the capacitance per unit area. In the absence of diffusion, we recover Eq. 4.7 for each point in space individually. As shown above, $V_m(x,t)$ is then determined by the intracellular ion concentrations up to an integration constant $V_0(x)$, which changes if a nonspecific stimulating current is applied at position x.

Setting D to a non-zero value introduces such an unspecific current, causing a shift in V_0:

$$V_0(x,t) = V_0(x,0) + D \cdot \int \frac{\partial^2 V}{\partial x^2}(x,t)dt. \tag{4.21}$$

We will now study the effect of this unspecific diffusive current on wave propagation. We start with a simple example. Consider a pulse of fixed shape and constant velocity propagating in a cable. Then we can replace space derivatives from Eq. 4.20 by time derivatives. For a point x^* of the medium, it follows from Eq. 4.20 that the change of $V_0(x^*)$ due to the pulse passing between $t = t_1$ and $t = t_2$ is:

$$V_0(x^*, t_1) - V_0(x^*, t_2) = \frac{D}{c^2}([\frac{\partial V^*}{\partial t}]_{t^+} - [\frac{\partial V^*}{\partial t}]_{t^-}), \tag{4.22}$$

which is zero if the medium is at rest at x^* for $t = t_1$ and $t = t_2$.

Although there is no persistent change in V_0, there still is an effect on dynamics at x^*, because V_0 is changed temporarily while the pulse is passing by. From Eq. 4.22 we see that the size of this temporary change is at any time less than $\frac{2}{\rho_s S C_m v^2}[\frac{\partial V^*}{\partial t}]_{max}$. Substituting typical values for cardiac tissue, e. g. $\rho_s = 150\Omega cm$, $S = 0.25\frac{1}{\mu m}$, $C_m = 1.8\frac{\mu F}{cm^2}$, $v = 100 cm/s$, and $[\frac{\partial V^*}{\partial t}]_{max} = 300V/s$, we find that $V_0(x^*, t^+) - V_0(x^*, t^-) < 80$ mV. Comparing this to the 25000 mV that are necessary to effect a 1% change in equilibria, we see that the equilibria at any point are only shifted by less than 0.01%, so that the error in the pulse dynamics introduced by a shift in V_0 is minimal.

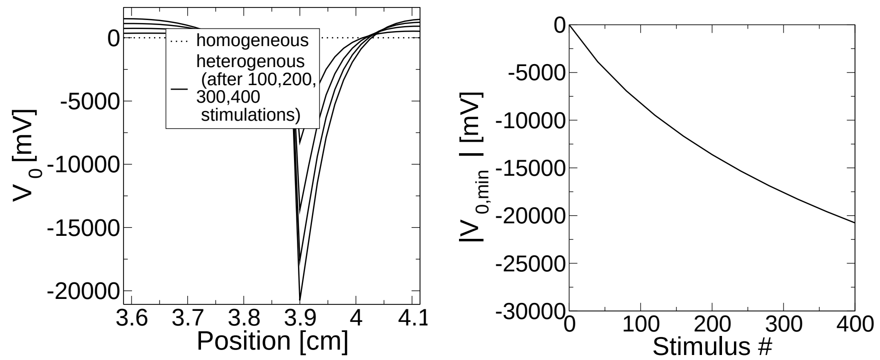

Figure 4.4: *The buildup of V_0 at a heterogeneity. We model a line of cells that in the first half (0 to 3.9 cm) a complete sodium block and in the second half normal sodium conductivity. Then we pace at the end with normal conductivity.* **Left***: buildup of V_0 in the region of the junction.* **Right***: Largest amplitude of V_0 as a function of number of stimulus number.*

This example supposed that the pulse encounters perfectly relaxed medium and the medium fully relaxes again after the pulse has passed. These conditions are only imperfectly satisfied for real pulses, so we confirmed the above results numerically in a ring of cells.

We chose a ring length of 12.5 cm, and the pulse was initiated by injection of a K^+ current in a limited region. We monitor the cumulated changes in $V_0(x)$ as the pulse propagates around the ring, but there is virtually no change of $V_0(x)$ after the pulse has attained stable shape (not shown).

The situation significantly changes if the pulse shape or velocity is variable, because inflow and outflow of unspecific current may then differ. A natural situation for changes in pulse shape or velocity to occur is at tissue heterogeneities. We numerically study the effect of a heterogeneity on V_0 by simulating a periodically paced line of cells that has normal electrophysiological properties in one half but a completely blocked sodium current in the second half. This sodium block reduced the conduction velocity to 10% in the affected region. As shown in Fig. 4.4a, we observe a constant buildup of V_0 at the junctions of the two domains. This buildup is in the order of 50 mV per stimulation, which is more than the buildup per stimulus in a paced cell. From the Fig. 4.4b it cannot be safely decided if the buildup of V_0 saturates eventually, but at any rate it continues to magnitudes where equilibria are notably shifted.

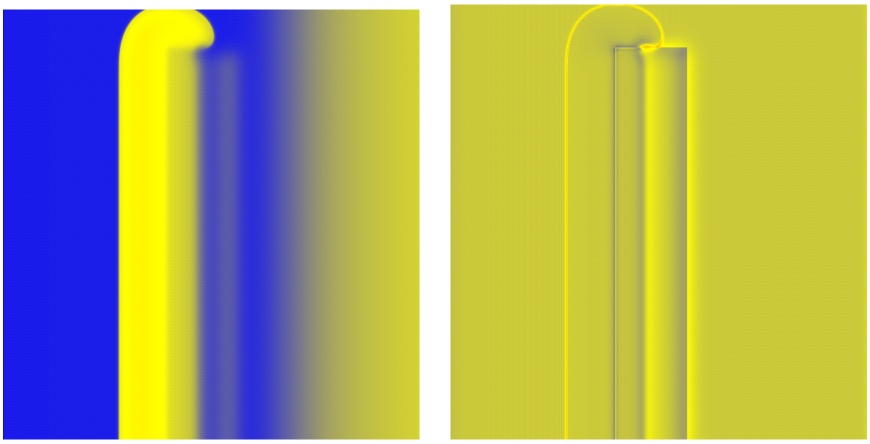

Figure 4.5: *Introduction to our visualization of changes in V_0. The left panel shows an early stage of the development of a spiral wave, directly after a stimulus has been set in a wave back. The right panel shows the corresponding distribution of V_0. We use the same coloring scheme as for spiral waves: blue for low values, yellow for higher values and red for still higher values. The initial picture is mostly yellow because there is no significant buildup of V_0 yet.*

In two dimensions, the planar wave fronts behave as pulses did in one dimension. For curved wavefronts, however, different results can be expected. This holds true especially for the tips of spiral waves. We introduce a spiral wave in a 12 cm × 12 cm medium of LR cells and monitor the buildup of V_0. In Fig. 4.5, we explain how we visualize changes in V_0. In Fig. 4.6 we show how positive and negative V_0 are built up along the tip trajectory. The changes of V_0 were in the order of 200 mV each time the tip passed, but as buildup is only slow, because it is confined to a narrow region around the tip. Besides, if a spiral tip goes along a certain path and later the same path backwards, the initial changes in V_0 are essentially neutralized. This is often the case for the widespread regular tip patterns.

Our results show that changes of V_0 are common in wave propagation in second-generation models, and that especially in heterogeneous media, these changes can become large. Clearly, a numerical method avoiding such changes is preferable.

The way to eliminate changes in V_0 is to allow only voltage diffusion that is connected to an equivalent ion diffusion. This could be achieved by di-

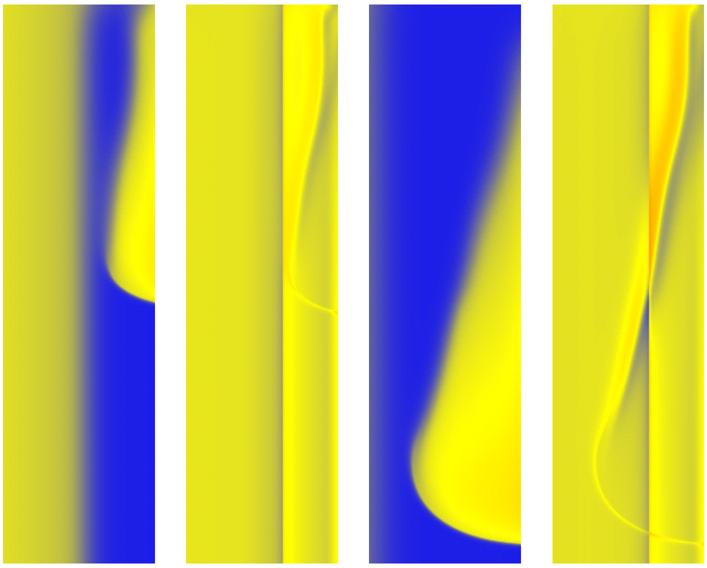

Figure 4.6: *The buildup of V_0 in the wake of a spiral tip. Left two pictures show the surrounding of a spiral tip and the corresponding distribution of V_0, right two pictures show the same situation 45 ms later. There is clearly a strong loss of V_0 along the front bounding at the spiral tip (around 200 mV), as this front cannot move forward because the medium is still refractory, and the large diffusive flows connected to the steep gradients of fronts keep flowing. Analogously, there is a large buildup of V_0 in the refractory medium bounding to the stopped front.*

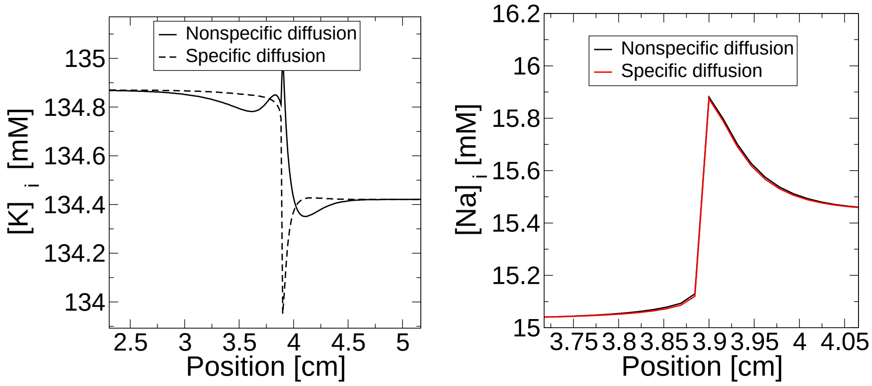

Figure 4.7: *Ionic concentration at a junction of domains for nonspecific and specific stimulation.* **Left***: Potassium concentration after 400 stimulations.* **Right***: Sodium concentration after 400 rotations.*

rectly formulating diffusion laws for the different *ions* and using them as a replacement of the voltage diffusion described in Eq. 4.20. The diffusion of ions between cells is, however, not understood in detail, while the description by voltage diffusion is experimentally well justified and specific conductivities can actually be measured [67, 131]. We therefore propose that voltage diffusion as described in Eq. 4.20 should be kept but the diffusive current should be accompanied by a corresponding ion flow. We choose potassium ions as carriers of the diffusive current, because they are by far the most abundant ion species in the cell [56]. The rate of change of the intracellular potassium concentration (see Eq. 4.1) is thus changed to:

$$\partial_t [K^+]_i = -\frac{A_{cap} C_m}{V_{myo} F} [I_{K,t} - 2 I_{NaK} - D \frac{\partial^2 V_m}{\partial x^2}(x,t)]. \tag{4.23}$$

It is not clear yet whether this proposed change leads to other undesirable In Fig. 4.7, we show the potassium and the sodium concentration at the transition to sodium blocked tissue as it has developed after 400 stimulations for specific or nonspecific diffusive current. The potassium concentration is markedly different for specific and nonspecific diffusion, because the potassium ions carry the diffusive current for specific diffusion. The difference closely mirrors course of V_0 (see Fig. 4.4). For the sodium concentration, it makes much less of a difference whether specific or non-specific diffusion is used. This is explained by the fact that even if two connected cells have significantly different rest states, voltage diffusion forces them into a similar state.

4.4 Discussion

Second-generation models that are stimulated by nonspecific currents, as is common practice, show unphysiological behavior, which has lead to concern among researchers considering such models for simulations.

It has been shown that these unphysiological behaviors can be avoided in single cells by reformulating the models in a way that the mathematical deficiency causing these behaviors, a linear dependency in the model equations, is removed, or by stimulating them only with currents that are accompanied by a corresponding ion flow.

We showed mathematically that nonspecific currents directly add to the integration constant V_0 that relates V_m to the ionic concentrations. The integration constant V_0 may be regarded as a model parameter. We studied the dependency of resting potential and ion concentration on V_0 in the Luo-Rudy model, finding that only very large changes in V_0 (≈ 25000 mV) produce significant changes in the rest state. The Courtemanche model of human atrial cells yields similar results. Using the above dependency, we can quantitatively assess the effect of given nonspecific stimulations.

In one-dimensional propagation, we showed that there is no effect for a pulse of fixed shape and propagation velocity. If a pulse does change in time, e. g. due to inhomogeneities in the medium, there may be a large distortion in V_0.

In two dimensions, we showed that V_0 permanently changes only along the tip trajectory of the spiral. Although these changes may be sizable, the long-term buildup is only slow, because it is confined to a narrow region around the tip. Besides, if a spiral tip goes along a certain path and later the same path backwards, the initial changes in V_0 are essentially neutralized. This is often the case for the widespread regular tip patterns.

In three dimensions, the dominating reentrant patterns are scroll waves. The relation of in- and outflow should are similar to those of spiral waves in 2D. We expect no new effects and do not perform simulations.

We established a method appropriate for future studies of wave propagation in cardiac tissue, in which each diffusive charge flow is accompanied by a corresponding flow of potassium ions. This results in a buildup of potassium at domain junction, which is not a mathematical defect model, but reflects the fact that ions are not free to diffuse in our model, which is probably not how real cells work. This potassium buildup is not as severe as buildup of V_0 because it does not change the equilibrium, so that the potassium concentration would be eventually restored if the cell is given sufficient rest. On the other hand, dynamic equilibria may be significantly different for the (standard) non-diffusing and diffusing ions. We have not yet resolved this issue. A way to avoid potassium buildup even without knowing much about the true mechanisms of ion diffusion between cells is to introduce weak diffusion of potassium ions, which would not significantly affect the behavior of the cell in other respects.

Chapter 5

An Efficient Electrophysiological Model of Human Atrial Cells

The realistic simulation of cardiac arrhythmias in the whole heart remains a major computational challenge. We show that the model by Courtemanche et al., one of the most realistic descriptions of human atrial tissue available today, can be reformulated to be computationally substantially more efficient while the important electrophysiological properties are retained. By fixing ionic concentrations and combining gating variables, we increase simulation speed by a factor of almost 4. To validate the model, we compare the original and the reformulated model with regard to action potential shape, action potential duration, and conduction velocity restitution. On all accounts we achieve good matches. We then use our newly developed model to study the properties of spiral waves in remodeled tissue, finding that these spiral waves are both faster and more stable than spiral waves in normal tissue.

5.1 Introduction

Cardiac arrhythmias are a major cause of death in the western world. To understand their mechanisms, models of cardiac excitation are being developed on all scales, from single cells to the whole heart.

In 1952, Hodgkin and Huxley developed the first ionic model of a biological excitable medium, the giant squid axon [55]. Since then, models that capture increasingly many features of cardiac cells have been put forward [7, 26, 77], including the widely used guinea pig ventricular model by Luo and Rudy ("LRd model", [78]). Comprehensive models of human atrial cells have been put forward by Nygren et al [95], based on the Lindblad et al. rabbit atrial cell model [74], and by Courtemanche, Ramira, and Nattel (CNR) [21] based on the LRd model. The CNR model has been used to explore the effects of tachycardia-induced remodeling and selective K^+ channel blockade on human atrial electrophysiology [22]. Unfortunately, the CNR model is complex and therefore computationally costly. This problem is becoming increasingly important as 2D and 3D studies are starting to get widely applied [51, 133, 134]. A computationally more efficient and yet physiologically accurate model is therefore desirable.

In this chapter, we first reformulate the CRN model of atrial cells, strongly reducing its complexity, while at the same time preserving its most important electrophysiological properties, i. e. action potential (AP) shape, AP restitution curve, conduction velocity, and properties of spiral waves. For this reformulation, we use the same methods as in our reduction of the Priebe-Beuckelmann model of ventricular cells [10]. Next, we use our newly developed model to study spiral wave activity in both normal tissue and in "remodeled" atrial tissue that has undergone electrophysiologic changes due to sustained atrial fibrillation. This remodeling of atrial tissue is crucial to an understanding of atrial fibrillation [126] and has been studied intensively [2, 92, 22].

5.2 Materials and Methods

Our reformulation of the CRN model has the following components: fixing ionic concentrations, replacing all activation variables except m by their steady-state values, combining the two I_{Na} inactivation variables j and h into one, and combining the I_K components I_{K_r} and I_{K_s} into a single I_{K_n}. All currents as formulated in the original model will be marked by a superscript "o" while all reformulated currents will be marked by a superscript "r".

5.2.1 Fixing the Ionic Concentrations

In the CRN model, the concentrations of Ca^{2+}, Na^+, and K^+, denoted by $[Ca]_i$, $[Na]_i$, and $[K]_i$, respectively) are state variables. The concentrations

$[\mathrm{Na}]_\mathrm{i}$ and $[\mathrm{K}]_\mathrm{i}$ do not change significantly over an AP, so we set them to their initial values ($[\mathrm{Na}]_\mathrm{i} = 11.2$ mmol, $[\mathrm{K}]_\mathrm{i} = 139$ mmol). $[\mathrm{K}]_\mathrm{i}$ will later be shifted in order to balance the effect of reformulating the currents. While $[\mathrm{Ca}]_\mathrm{i}$ strongly changes over an action potential, we still fix it to an intermediate value of $3 \cdot 10^{-4}$ mmol. This saves a substantial amount of computing time while, as results show, the excitation propagation properties remain largely the same.

5.2.2 Eliminating gating variables

In the CRN model, the *fast sodium current* is described by $I^o_{Na} = g_{Na} \cdot m^3 \cdot h \cdot j \cdot (V - E_{Na})$, where g_{Na} is the maximum sodium conductance, m is the fast activation variable, h and j are fast and slow inactivation variables, V is the transmembrane potential, and E_{Na} is the sodium equilibrium potential. Similar notations are used in the following equations. As in [10], we combine the inactivation variables h and j into one new variable v, i. e. we propose $I^r_{Na} = g_{Na} \cdot m^3_\infty \cdot v^2 \cdot (V - E_{Na})$ as the new equation for the fast sodium current. The new inactivation variable v has the usual Hodgkin-Huxley type dynamics, i. e. $\frac{dv}{dt} = \frac{v_\infty(V)-v}{\tau_v(V)}$. The functions $v_\infty(V)$ and $\tau_v(V)$ that determine the dynamics of v should be chosen such that I^r_{Na} matches I^o_{Na} as closely as possible. To achieve this, we performed voltage-clamp-like numerical experiments on the original CRN cell. Starting from the resting state, we fixed V at different values and studied the development of h and j. To get identical asymptotical behavior, we set $v_\infty(V) = \sqrt{h_\infty(V) \cdot j_\infty(V)}$. To get similar behavior over time, we need to make sure that $v(V)$ approaches its steady-state at a similar pace as does the quantity $\sqrt{hj}$ of the original model. We use our previously published method [10] to first obtain an initial approximation $\tau^{est}_v(V)$ of $\tau_v(V)$ and then determine $\tau_v(V)$ by minimizing $\int_0^{T_e} (I^r_{Na}(t) - I^o_{Na}(t))^2 dt$ with $T_e = 5\tau^{est}_v(V)$.

The *calcium current* $I_{Ca,L}$ of the CRN model is $I^o_{Ca,L} = g_{Ca,L} \cdot d \cdot f \cdot f_{Ca} \cdot (V - E_{Ca})$, where d is the activation variable and f the inactivation variable for the L-type calcium current. The only reformulation we perform for this current is that we replace the activation variable d by its steady-state function : $I^r_{Ca,L} = g_{Ca,L} \cdot d_\infty(V) \cdot f \cdot f_{Ca}(V) \cdot (V - E_{Ca})$

The original formulation of the *transient outward current* I_{to} is $I^o_{to} = g_{to} \cdot o^3_a \cdot o_i \cdot (V - E_K)$, o_a being the activation variable, o_i the inactivation variable of I_{to}. Again, we replace the activation variable o_a by its steady-state function and we obtain : $I^r_{to} = g_{to} \cdot o^3_{a,\infty} \cdot o_i \cdot (V - E_K)$.

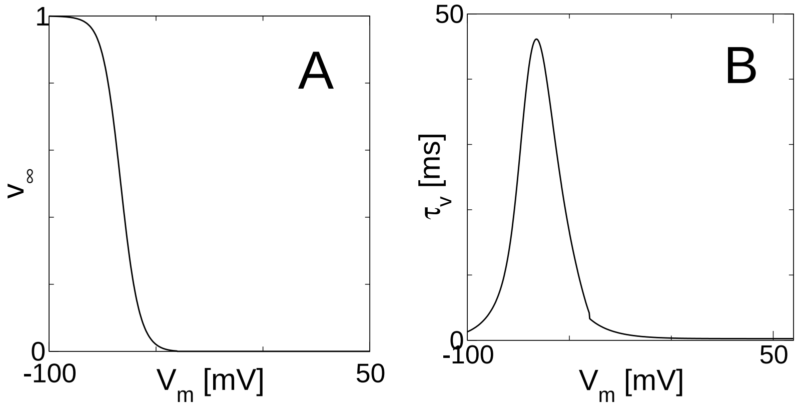

Figure 5.1: *(A) Steady state value, X_∞, and (B) time constant, τ_v, of the inactivation variable v of the fast sodium current (I_{Na}) in the reformulated Courtemanche et al. model.*

In the original model, the rapid and slow components of the delayed rectifier potassium current (I_{K_r} and I_{K_s}, respectively) are given by $I_{K_r} = g_{K_r} x_r (V - E_K)/(1 + \exp((V + 15)/22.4)))$ and $I_{K_s} = g_{K_s} x_s^2 (V - E_K)$, where x_r and x_s are activation variables.

As in [10], we propose the following combined current to replace the individual I_{K_r} and I_{K_s}: $I_{K_n} = g_{K_n} \cdot X^2 \cdot (V - E_{K_n})$. The new gating variable X has again standard Hodgkin-Huxley type [55] gating variable dynamics. To ensure that our newly defined current has the same asymptotic amplitude as the sum $I_{K_r} + I_{K_s}$, we define $X_\infty(V) = \frac{1}{X_{max}} \sqrt{g_{K_r} x_{r\infty}(V) + g_{K_s} x_{s\infty}(V)}$, where X_{max} is the maximal value of the square root term, so that $x_{n\infty}$ always lies between 0 and 1. To determine $\tau_X(V)$, we demand that for voltage clamps at any voltage, the resulting I_{K_n} should differ from $I_{K_r} + I_{K_s}$ as little as possible in a least-square sense, as in section 5.2.2. The resulting functions $x_{n\infty}(V)$ and $\tau_X(V)$ are shown in Fig. 5.2.

In the CRN model, The *ultrarapid potassium current* $I_{K_{ur}}$ is represented by $I^o_{K_{ur}} = g_{K_{ur}} \cdot u_a^3 \cdot u_i$. Once more, we replace the activation variable (u_a) by its steady-state function: $I^r_{K_{ur}} = g_{K_{ur}} \cdot u^3_{a\infty}(V) \cdot u_i \cdot (V - E_K)$

We leave the *time-independent currents* unchanged, but we sum them up into one time-independent current I_V (subscript “V” to indicate that I_V is a function of transmembrane voltage) and then tabulate I_V. Thus, the tabulated I_V consists of the inward rectifier potassium current (I_{K_1}), the sodium and the calcium background currents ($I_{Na,b}$ and $I_{Ca,b}$, respectively),

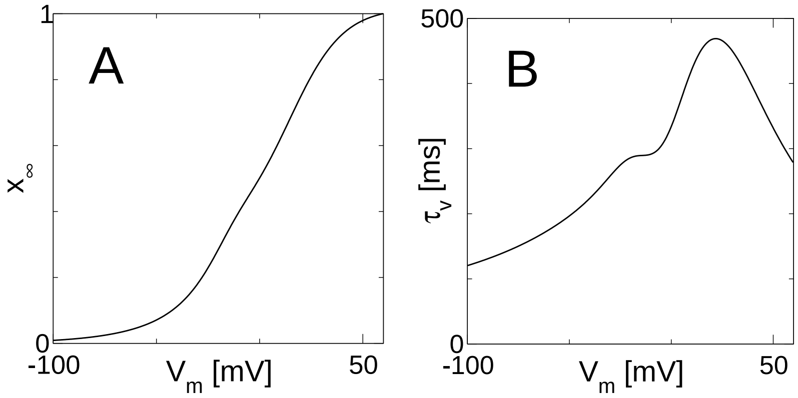

Figure 5.2: *(A) Steady-state value, x_∞, and (B) time constant, τ_x, of the activation gating variable x of the delayed rectifier potassium current (I_K) in the reformulated Courtemanche et al. model.*

the sarcolemmal calcium pump current ($I_{Ca,p}$), the sodium-potassium pump current (I_{NaK}) and the sodium-calcium exchange current (I_{NaCa}).

5.2.3 Model parameters

Our reductions produce alterations in the AP shape that can largely be reversed by adjusting a number of model parameters.

By fixing $[Ca]_i$ to 300 nM, we eliminated Ca-induced inactivation of $I_{Ca,L}$. In order to cancel out the resulting increase in $I_{Ca,L}$, we reduced $g_{Ca,L}$ from 1238 to 850 pS/pF. Also, the fact that $[Ca]_i$ is now significantly higher at resting potential (3 nM vs. 1.02 nM) raises the resting potential. To balance this change, we lower the potassium equilibrium potential E_K from a typical -86.8 mV (it is variable in the Courtemanche et al. model) to -91.0 mV by fixing $[K]_i$ to 155 mM. By comparing the amplitudes of I_{K_n} in the reformulated model and $I_{K_s} + I_{K_r}$ in the original model, we found that $g_{K_n} \approx 858$ pS/pF. Further, we decrease g_{to} by 10% to balance the replacement of the activation process of I_{to} by a steady-state activation. For the time-independent currents, we could get a good fit of both the sum of the time independent currents and the AP shape by attenuating the time-independent currents by 30%. In Table 5.1, we introduce a factor k_V for I_V to reflect this change. The temperature is 310 K, as in the CRN model. All parameter values of the CNR model and the reformulated model are shown in Table 5.1.

Parameter		CRN	reformulated
g_{Na}	[pS/pF]	7800	7.8
$g_{Ca,L}$	[pS/pF]	123.8	80
g_{Ito}	[pS/pF]	165.2	148.68
g_{K_1}	[pS/pF]	90	90
g_{K_r}	[pS/pF]	29.4	n. a.
g_{K_s}	[pS/pF]	129	n. a.
g_{K_n}	[pS/pF]	n. a.	858
k_V		1.0	0.7
$g_{Na,b}$	[pS/pF]	0.674	0.674
$g_{Ca,b}$	[pS/pF]	1.13	1.13
$I_{NaK,max}$	[pA/pF]	0.6	0.6
$I_{NaCa,max}$	[pA/pF]	1600	1600
$I_{Ca,p,max}$	[pA/pF]	0.275	0.275
$[Ca^{2+}]_i$	[mM]	variable	0.0003
$[Ca^{2+}]_o$	[mM]	1.8	1.8
$[Na^+]_i$	[mM]	variable	11.2
$[Na^+]_o$	[mM]	140	140
$[K^+]_i$	[mM]	variable	155
$[K^+]_o$	[mM]	5.4	5.4
T	[K]	310	310

Table 5.1: Parameter values in the CRN model and the reformulated model.

5.2.4 Numerical Approach

Mathematical model of wave propagation

We model the propagation of excitation by the cable equation:

$$\frac{\partial V}{\partial t} = -I_{ion} + \frac{1}{\rho_s S C_m}\frac{\partial^2 V}{\partial x^2} \tag{5.1}$$

$$\begin{aligned} I_{ion} = {} & I_{Na} + I_{K_{ur}} + I_{Ca,L} + I_{K_1} + I_{to} + I_{K_n} + I_{Ca,p} \\ & + I_{NaK} + I_{NaCa} + I_{Na,b} + I_{Ca,b}, \end{aligned} \tag{5.2}$$

where ρ_s is the resistivity (in Ωcm), S is the surface to volume ratio of the cable and C_m is the capacitance per unit area. For $C_m = 1.84\,\frac{\mu F}{cm^2}$, $S = 0.25\frac{1}{\mu m}$, and $\rho_s = 79.1\ \Omega$cm (isotropic case), we obtained an asymptotic plane wave conduction velocity (CV) of 85 cm/s (Table 5.2) to values observed experimentally [50, 73].

In the one-dimensional case we used a forward Euler method to integrate 5.1. In two dimensions, we used the two-dimensional analogue of 5.1 and split it into an ordinary differential equation (ODE) for reaction and a partial differential equation (PDE) for diffusion. The PDE was solved using an alternating direction implicit scheme [106], while for the ODE, we applied a forward Euler scheme. The relaxation equations for the gating variables were integrated using the standard method by Rush and Larsen [115]. In all simulations, we used a constant time step of 20 μs; in the 1D and 2D simulation we used a constant space step of 250 μm. All programs were coded in C++ compiled using the Gnu compiler gcc 2.95, and run on either a Pentium III/600 mobile or Athlon 1700+ CPU.

Numerical Accuracy

We tested the numerical accuracy of our model in a cable by changing the time and space step and measuring the CV of a propagating AP. For integration we used a forward Euler method.

Table 5.2 shows the results we obtained: in both the original and reformulated model, an increase of the time step from 10 μs to 20 μs caused a change less than 1%, while an increase in Δx from 100 μm to 300 μm reduced CV by 10%.

	Conduction velocity (cm/s)					
	reformulated model			CRN model		
$\Delta x (\mu\text{m})$	$\Delta t = 5\ \mu\text{s}$	$\Delta t = 10\ \mu\text{s}$	$\Delta t = 20\ \mu\text{s}$	$\Delta t = 5\ \mu\text{s}$	$\Delta t = 10\ \mu\text{s}$	$\Delta t = 20\ \mu\text{s}$
60	85.1	-	-	84.5	-	-
80	84.7	-	-	84.2	-	-
100	84.4	84.7	-	83.7	84.0	-
150	83.3	83.8	83.3	82.9	82.9	83.3
200	82.3	82.6	82.6	81.6	81.6	82.0
250	80.9	80.9	81.2	80.1	80.4	80.6
300	79.3	79.6	79.4	78.5	78.5	78.9

Table 5.2: Convergence of the conduction velocity as time and space step are decreased. The entry “-” means that no convergence was reached.

Restitution Properties

Restitution of action potential shape and action potential duration (APD) were obtained by pacing a single cell at different frequencies. For each frequency, we stimulated 10 times without recording to let transients pass. For the next stimulation, we determined the APD using a threshold corresponding to 90 % repolarization (-69.3 mV for the original CRN model, -68.3 mV for the reformulated version). All stimulus currents had a strength of 2.9 nA (2.6 times threshold) and a duration of 2 ms.

Restitution of CV was measured by initiating a pulse in a ring of cells. Starting with a ring of 2000 grid points (50 cm) , we waited until the pulse had fixed shape over the whole ring and then determined the DI and the CV. For short diastolic intervals, the pulse shape did not converge. Therefore, if the pulse had not converged after 5 rotations, we calculated the diastolic interval and the conduction velocity for each cell individually. This leads only to a slight variation in the CV associated with a given DI. Whenever either the pulse shape had converged or 10 recorded revolutions had passed, the ring size was reduced in steps of 20.

Spiral Waves

To obtain a spiral wave, we initiate a plane wave S_1 on a 1000×1000 grid of model cells. We let the wave traverse the square and apply a rectangular second stimulus S_2 when the end of the refractory region passes the midpoint to the square (the precise point in time varies with the tissue properties). The stimulus S_2 is rectangular (100 grid points wide, 800 grid points high). This leads to a symmetrical double spiral wave of which we simulate only the upper half. The spiral tip is defined to be the innermost part of the spiral front that excited neighboring tissue and we detect it manually. To determine the spiral period, we detect excitation times in each grid point individually and then calculate the average period of excitation as well as its standard deviation.

5.3 Results

5.3.1 The Action Potential

Figure 5.3 compares the steady-state action potential in the reformulated and the original CRN model. The overall shape of the reformulated AP is very similar to that of the original model. Figure 5.3 shows the main ionic currents, I_{Na}, $I_{Ca,L}$, I_{to}, I_{K_n}, and the remaining current I_V for both models. Comparing the currents in both models, we observe a perfect match for the sodium current and a good match for $I_{K_{ur}}$. For I_{to} and I_V the peak amplitude in the reformulated model is significantly larger and activation is slightly faster. The net charge carried by these currents during an action potential in the original and reformulated model differs by only 20% for I_V and less than 5% for I_{to}. On the other side, $I_{Ca,L}$ is significantly reduced in the beginning of the action potential, but it has the same qualitative shape.

5.3.2 Restitution of Action Potential Duration

Figure 5.4 compares the action potential duration in the original and the reformulated model. While both curves match closely, APD restitution is smoother in the reformulated model. The uneveness in the original model is connected to the activation of I_{to}, replacing the activation variable o_a of I_{to} by its steady-state value removes the bumps. The smoother APD restitution curve of the reformulated model might be an advantage, as we have no hints of irregularities from experimental studies.

Figure 5.5 shows the change of AP shape for increasing stimulation frequency (decreasing diastolic interval). It has been observed experimentally [122] that fast stimulation leads to an almost triangular AP, and the reformulated model exhibits this transition just like the CRN model. The data of Figs. 5 and 6 show that our model reproduces the restitution properties of the CRN model regarding both action potential shape and duration.

5.3.3 Restitution of Conduction Velocity

Figure 5.6 compares the restitution of conduction velocity in our model to that of the CRN model. We initiated a pulse revolving in a ring. If it reached constant speed eventually, we took this speed together with the diastolic interval as one data point of the CV restitution curve. For short diastolic

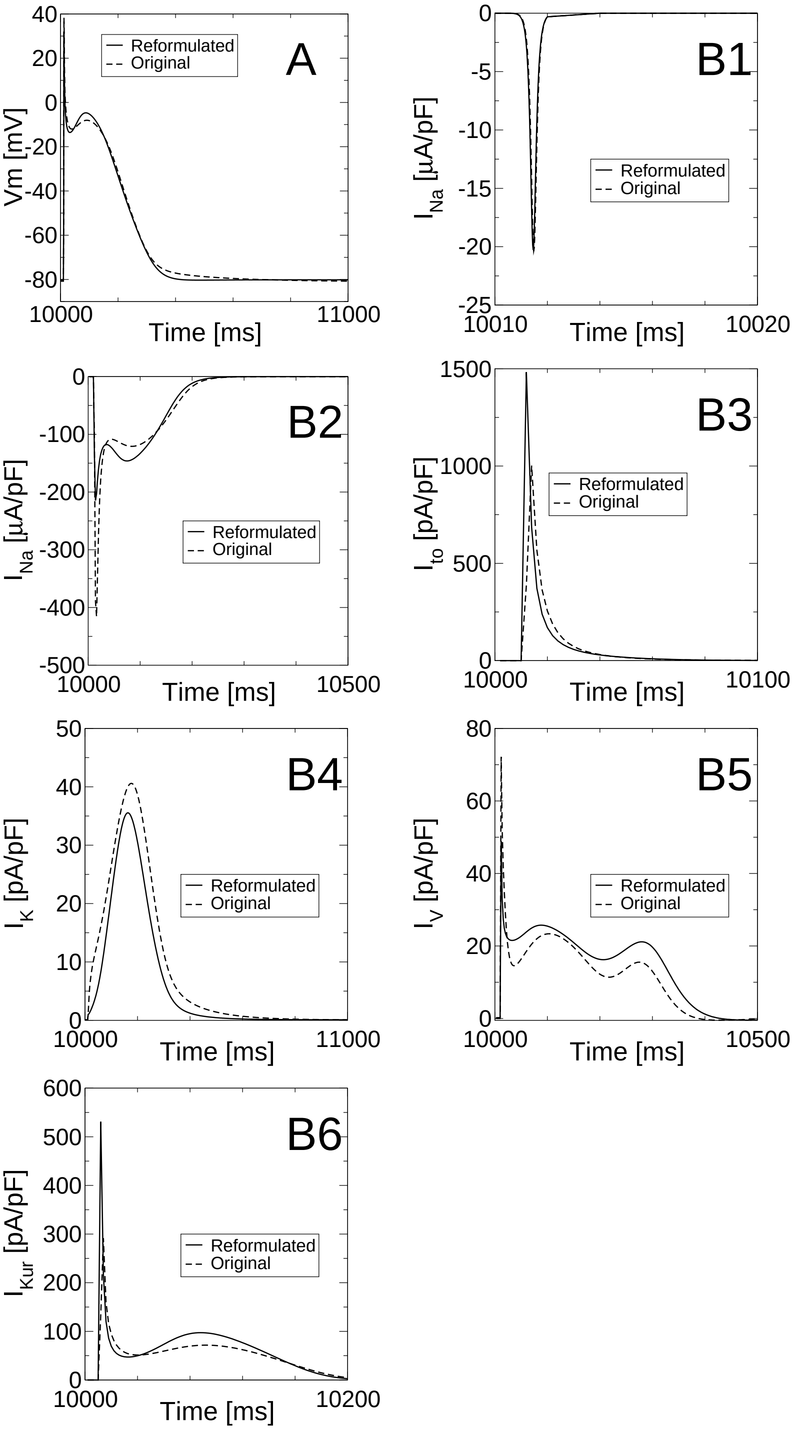

Figure 5.3: *Action potential and associated transmembrane currents in the reformulated Courtemanche et al. model (solid lines) and the original model (dashed lines). All graphs are from the 11*th *action potential of a train of action potentials. Action potential were elicited by a 2 ms stimulus current of 2.6 times threshold. (A) Transmembrane potential (V_m). (B1) Fast sodium current (I_{Na}). (B2) L-type calcium current (I_{Ca}). (B3) Transient outward current (I_{to}) . (B4) Delayed rectifier potassium current (I_K). (B5) Ultrarapid delayed rectifier potassium current (I_{Kur}). (B6) Total time-independent current (I_V). Note the different time scales.*

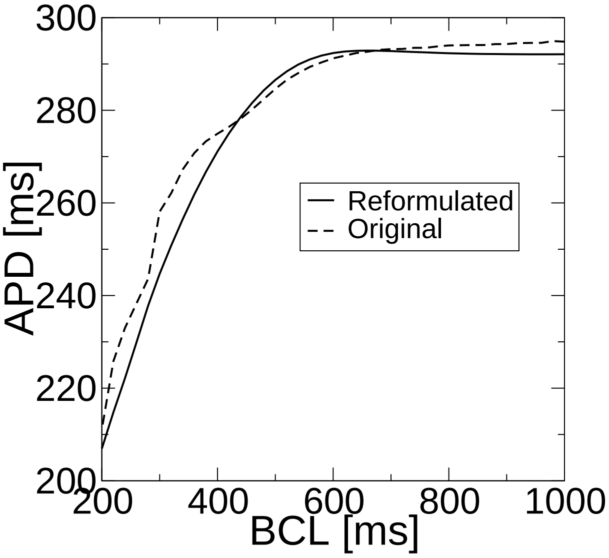

Figure 5.4: *The AP restitution curves of reformulated and CRN model. We stimulated periodically with different basic cycle lengths (BCLs) and let 10 stimulations pass unrecorded.*

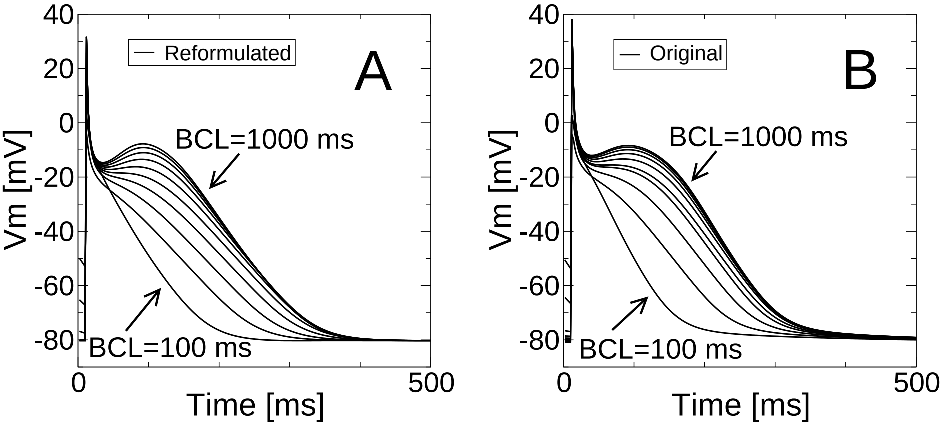

Figure 5.5: *Change of AP shape with stimulation period in the reformulated (A) and the original (B) CRN model. The stimulation period was changed from 1000* ms *to 100* ms *in steps of 100* ms. *For each stimulation period, we let 10 stimulations pass unrecorded. The pictures show a superposition of the 11th AP for different stimulation periods.*

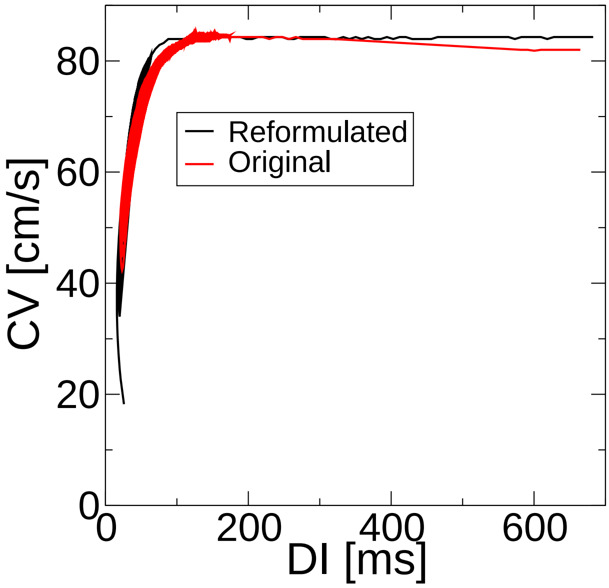

Figure 5.6: *The conduction velocity restitution of the reformulated and the original CRN model. See text for details.*

intervals, the pulse did no more approach constant speed, we then evaluated diastolic interval and CV at individual points. This is the reason why both the curve of our model and that of the original model are not single-valued (see section 5.2.4). Our model reproduces the long plateau of CV for slow stimulation and the sharp decrease of CV at a critical stimulation frequency.

5.3.4 Spiral Wave Properties

In 2D simulation studies, one of the most important forms of abnormal excitation is spiral wave reentry [103]. Atrial spiral wave activity was found in the atria experimentally [58]. Therefore, we initiated spiral waves in two-dimensional cardiac tissue in the original and the reformulated model and compared their dynamics.

Figure 5.7 shows spirals and tip movement over 3 s in both models. In the original model, the tip motion is in both cases is fairly regular for several rotations, but then the tip and a fairly large piece of the innermost spiral wave front come so close to the preceding front that they lose their ability to excite. The first point up the spiral arm that still has the ability to excite becomes the new tip, and starts to immediately move around the former tip, which has now become refractory medium. This introduces fairly large jumps in the spiral tip and causes a irregular and slow spiral period. The area traversed by the tip is about 6 cm × 6 cm, but it is likely to become significantly larger for longer simulations. The average period of the spiral is 335 ± 52 ms. In th reformulated model the tip can loose it's ability to excite as well, but this effect is much less pronounced. Spirals in the reformulated model are more regular and rotate faster. The area traversed by the tip is about 6 cm × 4 cm and the average period of the spiral is 273 ± 36 ms (average ± standard deviation taken over all points of the medium).

5.3.5 Applying the Model: Spiral Waves in Remodeled Atrial Tissue

The most important atrial arrhythmia is atrial fibrillation (AF), both because of its high incidence and because of the considerable long-term risks connected to it. While the excitation patterns underlying AF remain poorly understood, it has been shown that sustained AF leads to changes in the electrophysiology ("remodeling") that in turn promote the persistence of AF and finally make the disease chronic [126]. These electrophysiological changes have been studied quite extensively. It was found that $I_{Ca,L}$ was reduced by approximately 75% and I_{to} and $I_{K_{ur}}$ were both reduced by approximately 50 %. The effects of these changes in single cells have been assessed by Courtemanche et al. [22].

Spiral waves in remodeled tissue have not yet been studied in an ionic model of the human atria, although this might lead to a better understanding of the excitation patterns underlying AF. We therefore implemented the reductions of ionic currents given above and initiated a spiral in this remodeled medium.

A typical snapshot of a resulting spiral wave is given in Fig. 5.8. The spiral has a stable front, a regular, petal-shaped tip motion, a core size of about 4.5 × 4.5 cm and a period of 221 ± 7 ms.

To better understand the contributions of the amplitude reductions of the individual currents, we also studied spiral waves in media in which only one of these reductions was implemented. The results are presented in Fig. 5.8. Reduction of I_{to} alone has almost no effect. This is not surprising as

(A) Reformulated

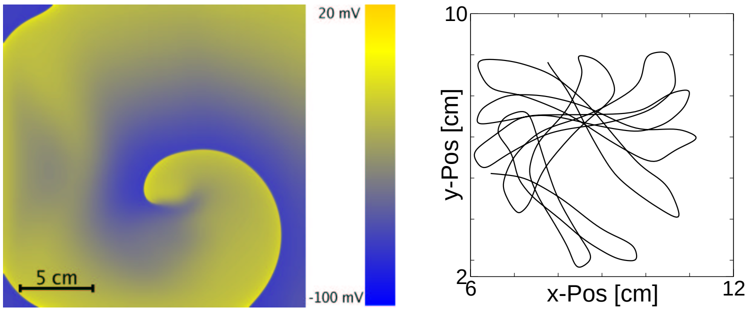

(B) Original

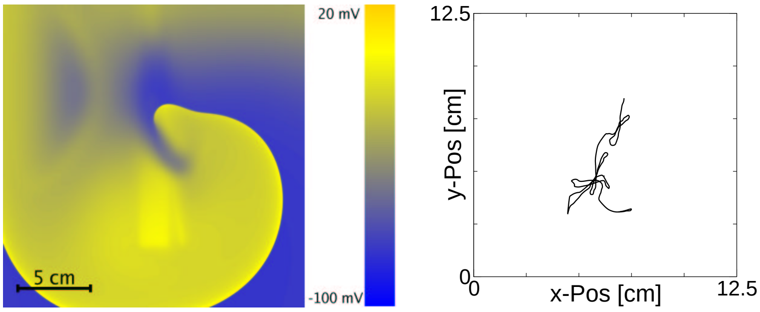

Figure 5.7: *Spiral wave form and tip motion in the reformulated (A) and the original (B) model. Medium size was* 25×25 *cm in all cases.*

Remodeled

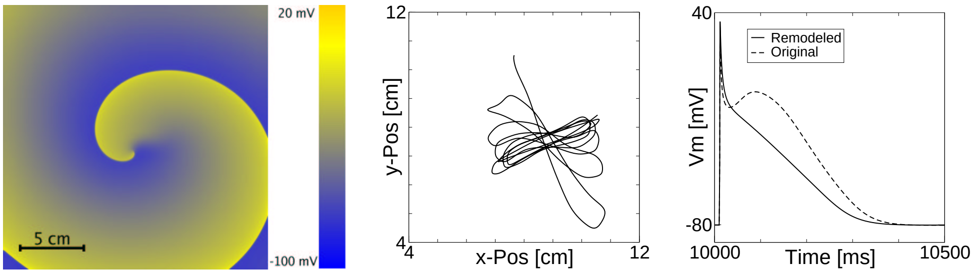

$I_{to} \rightarrow 50\%$

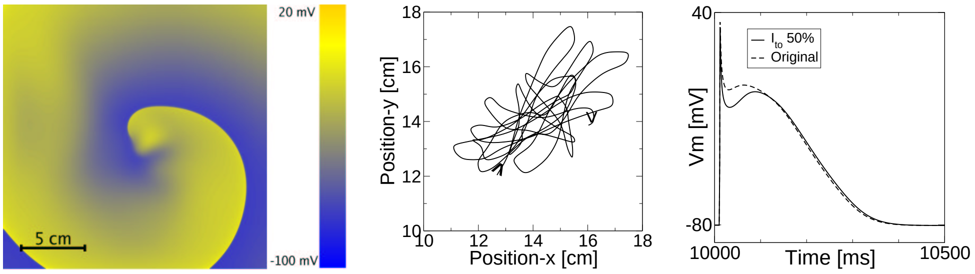

$I_{Kur} \rightarrow 50\%$

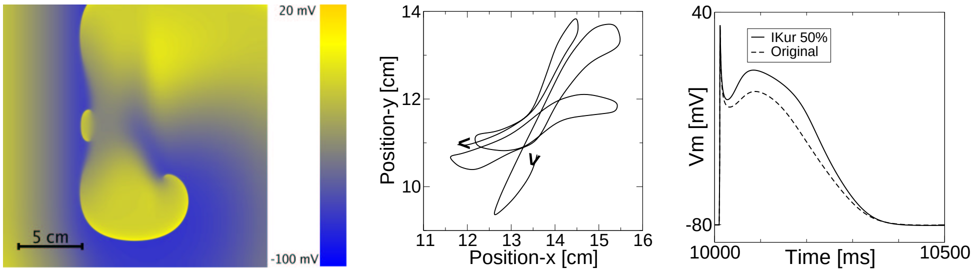

$I_{Ca,L} \rightarrow 25\%$

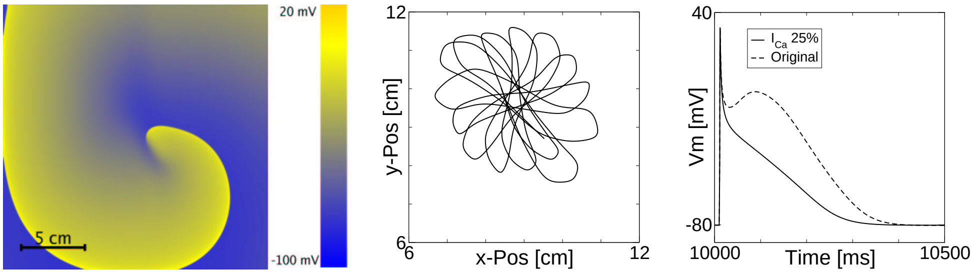

Figure 5.8: *Spiral wave form, tip motion, and action potential shape for remodeled atrial tissue. Upper three panels show properties of remodeled tissue. Below, we consider tissues with only a certain one of the modifications of ionic currents associated with remodeling.*

I_{to} affects neither the front nor the back shape of the action potential and should therefore not be expected to play a major role in wave propagation. If only $I_{K_{ur}}$ was reduced, the wave fronts break very easily. This breakup is interesting because it seems to include a new mechanism: Some wave fronts start to die out as they come too close to the preceding wave back, but later "re-ignite" so that there are actually four open ends developing, as opposed to two for normal breakup. Most importantly, a reduction of $I_{Ca,L}$ alone already leads to a spiral with virtually the same characteristics as for the fully remodeled medium (with a period of ms).

5.3.6 Numerical Efficiency

Due to our reduction, the number of state variables went down from 20 to 7. To compare numerical efficiency of the original and the reformulated model, we simulate in each model a single cell for 1000 s, with a depolarizing stimulus given at the beginning of the stimulation. Computation time is 95 s for the original model and 25 s for the reduced model, corresponding to a speed gain factor of 3.8 on a Pentium III/600 CPU.

5.4 Discussion

In this study, we reformulated the Courtemanche-Ramirez-Nattel model in a computationally efficient way while closely observing that the most important electrophysiological properties remain unaltered.

AP shape – In order to achieve a good fit we had to change several parameters. The calcium conductance $g_{Ca,L}$ was changed in order to have a calcium influx of realistic size during continued pacing even though the intracellular calcium concentration has been fixed. Consequently, the resting potential went up, which we counteracted by decreasing the potassium equilibrium potential to -91 mV. Finally, we reduced I_{to} in order to avoid a too strong decrease of V after the initial spike.

Main ionic currents – The general time course of all major ionic currents is well reproduced in the reformulated model. A significant difference is in the size of the peaks of the $I_{Ca,L}$ current (inward), whichis smaller than in the original model, and the I_{to} current (outward), which is larger than in the reformulated model. The combined effect of these differences is that the incision between the spike and the dome phase of the AP is more pronounced in the reformulated model. This does, however, not have an significant effect on wave propagation.

APD restitution – APD restitution is closely reproduced in the reformulated model, except for the fact that the restitution curve of the original CRN paper is more ragged. Looking at experimental papers on restitution in atrial myocytes, [66, 36] we find no evidence of raggedness therefore do not try to mimic it in our model.

CV restitution – CV restitution is matched very well and lies within the range indicated by experiments [50, 73].

Spiral waves – Spiral wave properties are similar, including the peculiar tip movement in the original model The reformulated model does not exhibit the extreme instabilities of the original CRN model.

Numerical efficiency – We were able to reformulate the CRN model with 6 gating variables. The total number of variables was reduced from 21 in the original model to 7 in the reformulated model, which now consist of the transmembrane potential V and the gating variables of I_{Na} (m and v), $I_{Ca,L}(f)$, $I_{to}(o)$, $I_K(X)$, and $I_{K_{ur}}(u_i)$. The computational gain at the cellular level was of the order of a factor 4. The computational efficiency can be further improved by applying more sophisticated schemes such as adaptive space masks [17] or adaptive time step schemes.

Remodeled Tissue – We find that spiral waves in remodeled atrial tissue have a shorter period than in normal tissue. This agrees well with findings of shorter APDs during atrial tachycardia [37]. On the other hand, we find that the spirals are very stable, which seems to suggest that spiral breakup [97] is not the mechanism that leads to atrial fibrillation, and supports alternative theories on the genesis of atrial fibrillation [58].

Limitations – The reformulated Courtemanche model has been designed to make large-scale simulation of the atria efficient. Intracellular calcium handling has been removed, so the reformulated model is not suited for studies of calcium dynamics. The intracellular concentrations of Ca^{2+}, Na^+, and K^+ have been fixed, so overload conditions cannot be simulated. Also, the ionic currents have been modified, so that studies that depend on the detailed time course of the individual currents might be better advised to use the full model if computation time is not an issue. It should be noted, however, that the understanding many of the mentioned mechanisms, especially intracellular calcium dynamics, is yet far from complete, so that even full ionic models are of limited reliability.

Summary – We developed an efficient electrophysiological model of single human atrial cells that facilitates large-scale computational studies of reentrant arrhythmias. Using this model, we found that spiral waves in remodeled atrial tissue are much more stable and have a significantly shorter period than spiral waves in normal atrial tissue.

5.5 Appendix: The Model Equations

Units are as follows (in all formulas): time in ms, voltage in mV, ion concentrations in mM, conductivities in nS/pF, currents in pA/pF.

5.5.1 The State Variables

Symbol	meaning	initial value
V	transmembrane voltage	-80.15
m	I_{Na} activation	0.00344758
v	I_{Na} inactivation	0.96354
f	$I_{Ca,L}$ inactivation	0.999
X	I_{K_n} inactivation	0.0290321
o_i	I_{to} inactivation	0.999071
u_i	$I_{K_{ur}}$ inactivation	0.999

5.5.2 Equilibrium Potentials

$$E_{Ion} = \frac{RT}{zF} ln \frac{[Ion]_o}{[Ion]_i} \quad \text{for Ion = Na, Ca, and K,} \tag{5.3}$$

where R is the universal gas constant, T the absolute temperature, F the Faraday constant, and z the valence of the ion.

5.5.3 Inward Currents

Fast Na^+ current : I_{Na}

Above, we used v_∞ and τ_v that were calculated pointwise as described in section 5.2.2. Here we give continuous approximations of both functions.

$$I_{Na} = g_{Na} \cdot m^3 \cdot v^2 \cdot (V - E_{Na}) \tag{5.4}$$

$$\alpha_m = \begin{cases} \frac{0.32 \cdot (V+47.13)}{1-\exp(-0.1 \cdot (V+47.13))} & : \text{ for } V \neq -47.13\text{mV} \\ 3.2 & : \text{ for } V = -47.13\text{mV} \end{cases} \tag{5.5}$$

$$\beta_m = 0.08 \cdot \exp(\frac{-V}{11}) \tag{5.6}$$

$$v_\infty = 0.5002 \cdot (1 - \tanh(7.743 + 0.1164 \cdot V)) \tag{5.7}$$

$$\tau_v = 0.3983 + 0.994 \cdot \frac{1 - \tanh(8.743 + 0.1262 \cdot V)}{1 - \tanh(0.08841 \cdot (V + 94.42))} \tag{5.8}$$

Slow Ca^{2+} current : $I_{Ca,L}$

$$
\begin{aligned}
I_{Ca,L} &= g_{Ca,L} \cdot d_\infty \cdot f \cdot f_{Ca} \cdot (V - E_{Ca}) && (5.9)\\
d_\infty &= [1 + \exp(-\frac{V+10}{8})]^{-1} && (5.10)\\
\tau_f &= 9 \cdot [0.0197 \exp[-0.0337^2 (V+10)^2] + 0.02]^{-1} && (5.11)\\
f_\infty &= [1 + \exp(-\frac{V+28}{6.9})]^{-1} && (5.12)\\
f_{Ca} &= (1 + \frac{[\mathrm{Ca}]_\mathrm{i}}{0.00035}))^{-1} && (5.13)\\
& && (5.14)
\end{aligned}
$$

5.5.4 Outward Currents

Transient outward current : I_{to}

$$
\begin{aligned}
I_{to} &= g_{to} o_{a_\infty}^3 o_i (V - E_K) && (5.15)\\
o_{a_\infty} &= [1 + \exp(\frac{V+20.47}{17.54})]^{-1} && (5.16)\\
\alpha_{o_i} &= [18.53 + \exp(\frac{V+113.7}{10.95})]^{-1} && (5.17)\\
\beta_{o_i} &= [35.56 + \exp(\frac{V+1.26}{7.44})]^{-1} && (5.18)\\
\tau_{o_i} &= (K_{Q_{10}}(\alpha_{o_i} + \beta_{o_i}))^{-1}, && (5.19)\\
K_{Q_{10}} &= 3 && (5.20)\\
o_{i_\infty} &= [1 + \exp(\frac{V+43.1}{5.3})]^{-1} && \\
& && (5.21)
\end{aligned}
$$

Time-independent K^+ Current : I_{K_1}

$$
I_{K_1} = \frac{g_{K_1} \cdot (V - E_K)}{1 + \exp[0.07(V+80)]} \qquad (5.22)
$$

Delayed rectifier current : I_K
As with v_∞ and τ_v, we calculated $x_{n,\infty}$ and τ_X pointwise, as described in section 5.2.2. Here we give approximations of both functions.

$$
I_K = g_K \cdot X^2 \cdot (V - E_K) \qquad (5.23)
$$

$$x_{n,\infty} = \frac{1.080}{1+\exp(0.1165-0.04854V)} \tag{5.24}$$

$$\tau_X = 366.6\cdot\exp(-\frac{(-18.46+V)^2}{1102}) \tag{5.25}$$

$$+462.9\cdot(1+\tanh(-0.3822+0.005790\cdot V)) \tag{5.26}$$

$$+119.7\cdot(1-\tanh(1.157+0.08836\cdot V)) \tag{5.27}$$

Ultrarapid delayed rectifier K^+ current

$$I_{K_{ur}} = g_{Kur}u_{a_\infty}^3 u_i(V-E_K) \tag{5.28}$$

$$g_{Kur} = 0.005+\frac{0.05}{1+\exp(-\frac{V-15}{13})} \tag{5.29}$$

$$u_{a_\infty} = [1+\exp(\frac{V+30.3}{9.6})]^{-1} \tag{5.30}$$

$$\alpha_{u_i} = [21+\exp(-\frac{V-185}{28})]^{-1} \tag{5.31}$$

$$\beta_{u_i} = \exp(\frac{V-158}{16}) \tag{5.32}$$

$$\tau_{u_i} = (K_{Q_{10}}(\alpha_{u_i}+\beta_{u_i}))^{-1} \tag{5.33}$$

$$K_{Q_{10}} = 3 \tag{5.34}$$

$$u_{i_\infty} = [1+\exp(\frac{V-99.45}{27.48})]^{-1} \tag{5.35}$$

5.5.5 Background Currents

Ca^{2+} background current : $I_{Ca,b}$

$$I_{Ca,b} = g_{Ca,b}\cdot(V-E_{Ca}) \tag{5.36}$$

Na^+ background current : $I_{Na,b}$

$$I_{Na,b} = g_{Na,b}\cdot(V-E_{Na}) \tag{5.37}$$

5.5.6 Pumps and Exchangers

Ca^{2+} pump current : $I_{Ca,p}$

$$I_{Ca,p} = I_{Ca,p,max}\frac{[Ca]_i}{0.0005+[Ca]_i} \tag{5.38}$$

Na^+**-**K^+ **pump :**I_{NaK}

$$\begin{aligned} I_{NaK} &= I_{NaK,max} \cdot f_{NaK} \frac{1}{1 + (K_{m,Nai}/[Na]_i)^{1.5}} \frac{[K]_o}{[K]_o + K_{m,Ko}} && (5.39) \\ f_{NaK} &= (1 + 0.1245 \exp(0.1 \frac{FV}{RT}) + 0.00365 \sigma \exp(-\frac{FV}{RT}))^{-1} && (5.40) \\ \sigma &= 0.1428 \cdot (\exp(\frac{[Na^+]_o}{67.3}) - 1) && (5.41) \end{aligned}$$

with $K_{m,Nai} = 10$ mM, $K_{m,Ko} = 1.5$ mM, $\gamma = 0.35$, $k_{m,Na} = 1.38$, $K_{m,Ca} = 87.5 mM$, and $k_{sat} = 0.1$

Na^+**-**Ca^{2+} **exchanger :** I_{NaCa}

$$I_{NaCa} = \frac{I_{NaCa_{max}} [\exp[\gamma FV/(RT)][Na]_i^3 [Ca]_o - \exp[(\gamma - 1) FV/(RT)[Na]_o^3 [Ca]_i]]}{(K_{m,Na}^3 + [Na]_o^3)(K_{m,Ca} + [Ca]_o) \cdot [1 + k_{sat} \exp[(\gamma - 1) FV/RT]]} \tag{5.42}$$

Chapter 6

A Realistic and Efficient Model of Excitation Propagation in the Human Atria

Starting from human anatomical data, we construct a triangle mesh representing the atrial surface. We include fiber orientation and special conduction pathways that are known to be important for wave propagation. The electrophysiology of the cells is described by the reformulation for the Courtemanche et al. model described in the preceding Chapter. The activation sequence during sinus rhythm as computed by our model is compatible with experimental findings. We show that spiral waves can be induced a carefully placed extrasystole. We conclude by comparing isotropic and anisotropic wave propagation in our model.

6.1 Introduction

Atrial arrhythmias are clinically important because they are so common. Atrial fibrillation alone occurs in 0.4% to 0.9 % of the general population and in 2% to 4% of the people above 60 [62, 13]. As longevity increases, so does the need to develop therapies for atrial fibrillation.

To understand the mechanisms underlying atrial arrhythmias, various approa-ches are needed, from clinical studies and electrophysiological experiments to theoretical modeling of wave propagation in atrial tissue. In this Chapter we discuss the feasibility of a realistic model of anatomy and electrical activity of the atria.

Starting with Moe [87], there have been a number of atrial models [80, 61, 75, 121]. These models deliberately use a simplified geometry and models of electrical activity that differ considerably from that of human atrial cells.

Recently, an anatomically accurate 3D model of the atria has been developed by Harrild and Henriquez [51]. They use a 3D finite volume method and the Lindblad model [95] of atrial electrical activity. The Harrild/Henriquez model is able to describe accurately the normal atrial activation sequence. However, since iterative integration methods in 3D are used, extensive computations are necessary and it is difficult to study reentrant arrhythmias using this model. Furthermore, the model does not incorporate anisotropy of the atrial walls, which is known to be pronounced [113].

In this study, we develop a numerically efficient model that is realistic both with respect to the atrial geometry and the atrial electrophysiology.

6.2 Model construction

Before we decide on a modeling strategy, we take a close look at our object of study. In Chapter 1, the atria were shown as a part of the heart, while Fig. 6.1 shows both atria in greater detail. The atria have a complex geometry, and also a complicated topology, due to the septum and the many holes marking the transition to blood vessels and to the ventricles (7 in total). The wall is fibrous, but for the most part smooth, with the important exception of a tubular network attached to part of the inner wall of the right atrium. The tubes of this network are called *pectinate muscles* and the ridge at which they coalesce is called *crista terminalis*. These tubes conduct excitation faster than the free atrial wall.

We model the atria as a curved surface in three-dimensional space. The structures discussed in the last paragraph are domains in three-dimensional space, so the most obvious approach to modeling them is to approximate them by tetrahedra, as fully three-dimensional. However, the walls of the atria are at all places very thin, in the order of 1mm in the right atrium and up to 3mm in the left. This suggests that there is little variation in transmembrane voltage across the atrial wall and that the atrial wall may be modeled as a curved surface, which drastically reduces the computational complexity of the model.

The most appropriate data structure to represent a curved surface is a

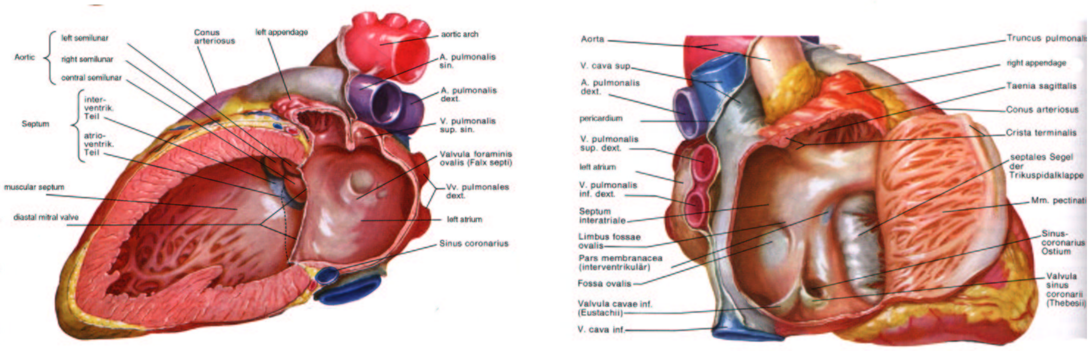

Figure 6.1: *The left and the right human atrium. Note especially the thin walls and the tubular network on the inside of the right atrium.*

triangular mesh. Only in a triangular surface can each vertex be moved individually without creating non-planar surface elements. Also, triangular surfaces are the best studied and many algorithms are available for their manipulation [116].

The anisotropy of the atrial wall can be accounted for by assigning a vector to each triangle that defines the local fiber orientation. The pectinate muscles are modeled as triangle strips that are connected to the atrial wall.

6.2.1 Anatomical Data

Our primary source for anatomical atrial data is the Visible Human Project (http://www.nlm.gov/pubs/visible_human.html). It provides voxel data of a male and a female body(Fig 6.2). Freudenberg et al. segmented these data [38] and provided us with a data set describing the atria (see Fig. 6.3a) of the Visible Female at a resolution of 0.67 mm.

6.2.2 Triangular Mesh Generation

From the voxel data we generated a triangular surface using a generalized version of the Marching Cubes isosurfacing algorithm [76]. An isosurfacing algorithm is in principle applicable because if we define a function that is 1 for all atrial voxels and 0 for all other voxels, then the isosurface of 0.5 approximates the atrial surface (but holes and the septum pose problems that will be addressed later).

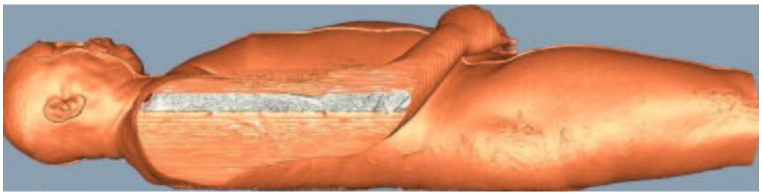

Figure 6.2: *The Visible Female. In the Visible Human Project, two corpses have been cut into slices and each slice has been scanned in. The resulting voxel data have been made publicly available by the National Institute of health. Scanning resolution was 1 mm in the case of the Visible Male and 1/3 mm in the case of the Visible Female.*

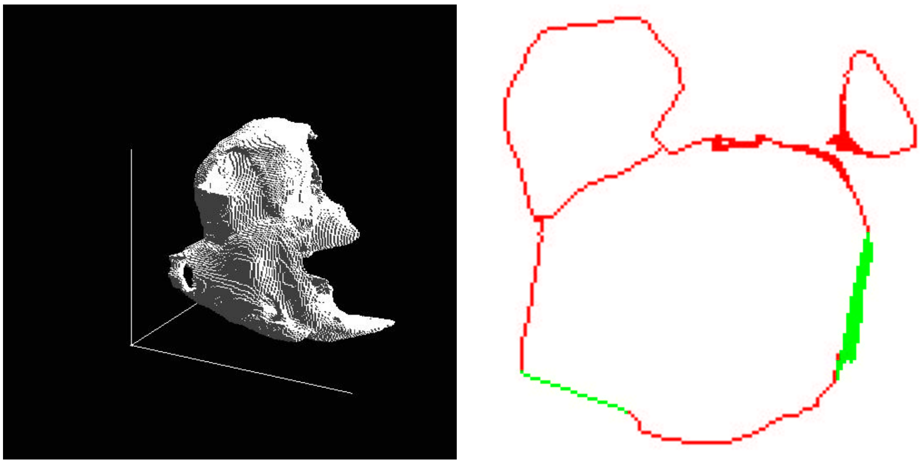

Figure 6.3: *Voxel representation of the human atria.* **Left***: The voxels belonging to the atria of the Visible Female.* **Right***: Screenshot from our program for the manipulation of voxel set. The screenshot shows one of the central slides of the Visible Female atrium. Red squares belong to the atria, green squares have been temporarily added to close the holes of the atria.*

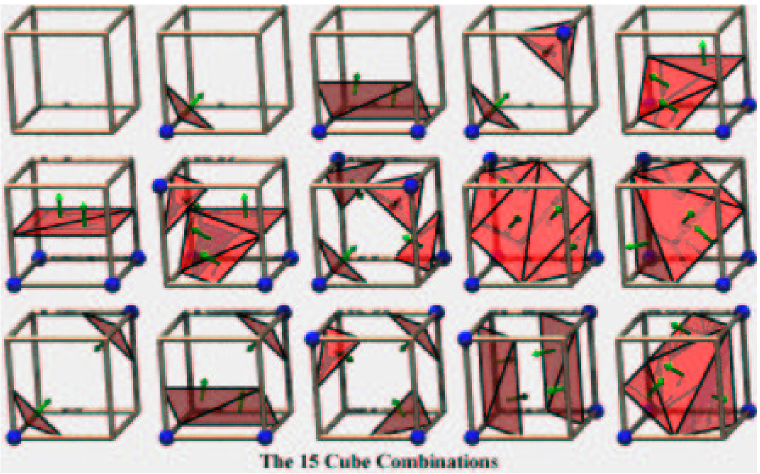

Figure 6.4: *The Marching Cubes Algorithm for the detection of isosurfaces of a given function. Each voxel is assigned the set of isosurface triangles inside of it on the basis of the function values at the voxel's vertices. For the eight corners of a voxel, there are* $2^8 = 256$ *possible combinations for the function values to lie above or below a given isovalue. Taking symmetries into account, it is sufficient to specify the intersection triangles for 15 of these combinations.*

The Marching Cubes Algorithm (MCA) needs a volume of voxels on which a real-valued function is defined. The idea of the algorithm is to "march" through this volume voxel by voxel, and for each voxel to decide if and how the isosurface crosses it, without reference to anything but the function values at the voxel's vertices. This clearly works if, for example, all voxel vertices are above or below the isovalue (then the isosurface does not intersect with the voxel). But it has been shown [76] that in all $2^8 = 256$ possible combinations of 8 voxel vertices lying above or below the isovalue, the voxel can be assigned "triangles of intersection" with the isosurface in a way that the triangles of intersection always match for neighboring surfaces (see Fig. 6.4).

The holes and the septum pose problems to the application of the MCA. Due to the wholes, the border of the atria is not clearly defined, i.e. we cannot immediately tell which voxels belong to the atria. At the point where the septum meets the atrial wall, there are actually three domains meeting (the right atrium, the left atrium and the outside), so that the above/below-approach of the MCA cannot directly be applied.

To handle the holes, we developed a software for manipulation of voxel sets (see Fig. 6.3b). It allows viewing and manipulation of voxel data in slices and includes algorithms for the detection and localization of holes. Using this software, we temporarily closed the atrial holes with marked voxels.

The problem of having more than 2 domains meeting is solved by the recently developed Generalized Marching Cubes Algorithm (GMCA) [53]. It accepts labeled domains as input (each voxel gets a label 1, 2, 3, ..) and outputs triangle patches that define the boundaries between the labeled regions such that the edges of the patches match. After closing the holes temporarily and applying the GMCA, we remove the triangles that intersect with temporary voxels.

We obtained the atrial surface (Fig. 6.5) in good quality as a result of the processing described. The mesh consists of roughly 33000 vertices and 66000 triangles. For proper description of wave propagation we further subdivided each triangle into 9 triangles and obtained a surface composed of approximately 600000 triangles with an average side length of 0.28 mm.

6.2.3 Anisotropy and Pectinate Muscles

The atria are strongly anisotropic. The conduction speed along the axis of the myocyte fiber is about three times that in the direction orthogonal to the fibers [113]. The information regarding typical orientations of gross fibers was obtained from dissections of anatomical specimens. We created a software (see Fig. 6.7b) that allowed us to manually copy these fiber orientations onto views from different angles of our model and then project them onto the underlying triangles. We used interpolation for the triangles that did not receive a fiber orientation in this way.

The relative sizes of the diffusion constants of normal tissue (fiber direction and orthogonal) as well as of crista terminalis/pectinate muscles are set such that the relative conduction velocities in a cable coincide with experimental values [113]. The resistivity of the medium is set such that total activation time of the model atria coincides with experiments.

Crista terminalis and pectinate muscles are modeled as triangle strips on top of the atrial wall (see Fig 6.7a). This way, they are quasi-one-dimensional structures and fit seamlessly into our model framework. The triangle strips are connected to the atrial wall at their beginning and end and to a lesser degree in between.

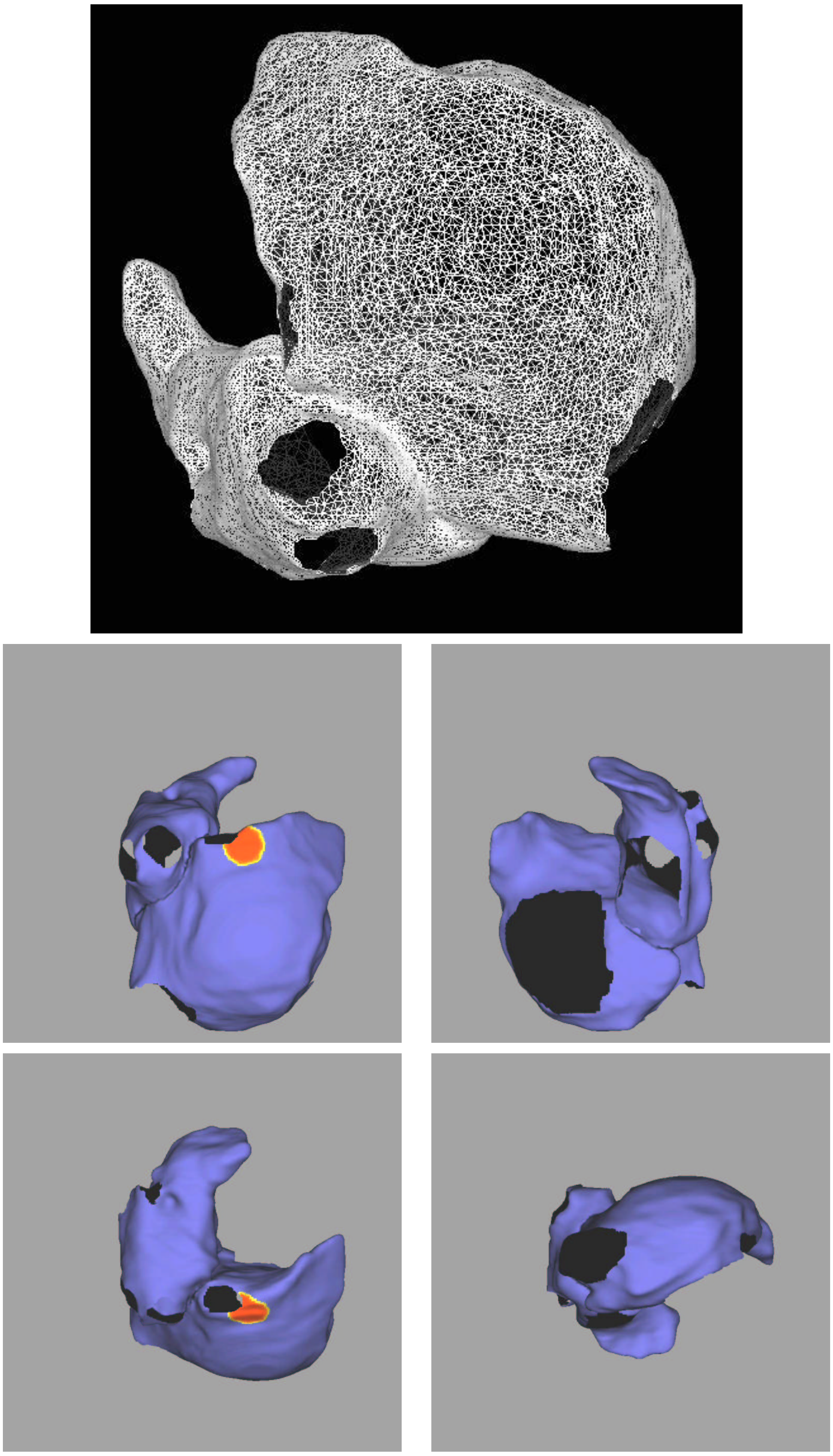

Figure 6.5: *Different views of our atrial model. On top is a view of the triangular mesh. Of the lower four panels, the upper left panel shows the view form the back, upper right panel from the front, lower left panel from above and lower right panel from below. The red spot indicates the position of the sinus node.*

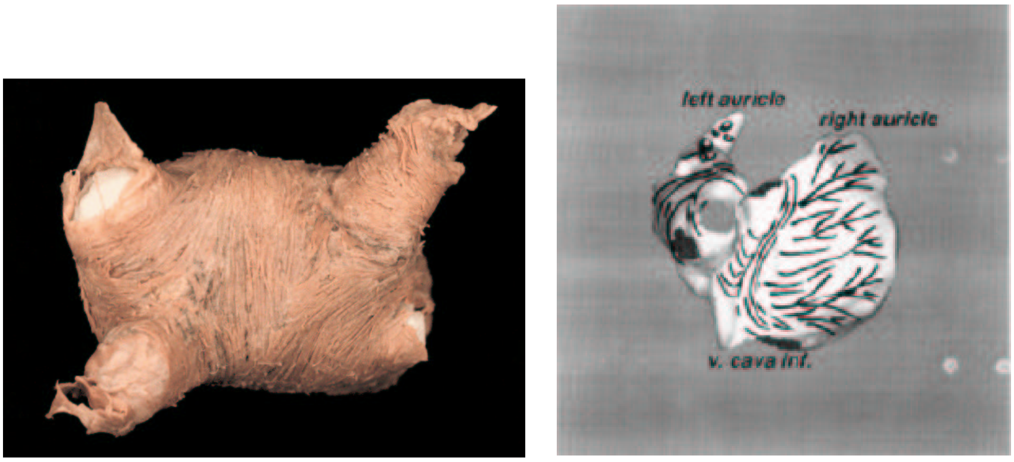

Figure 6.6: *The atria are fibrous.* **Left***: Photograph of part of the left atrium. The four openings are the transitions to the pulmonary veins.* **Right***: Typical fiber orientations drawn into one of the views of our model.*

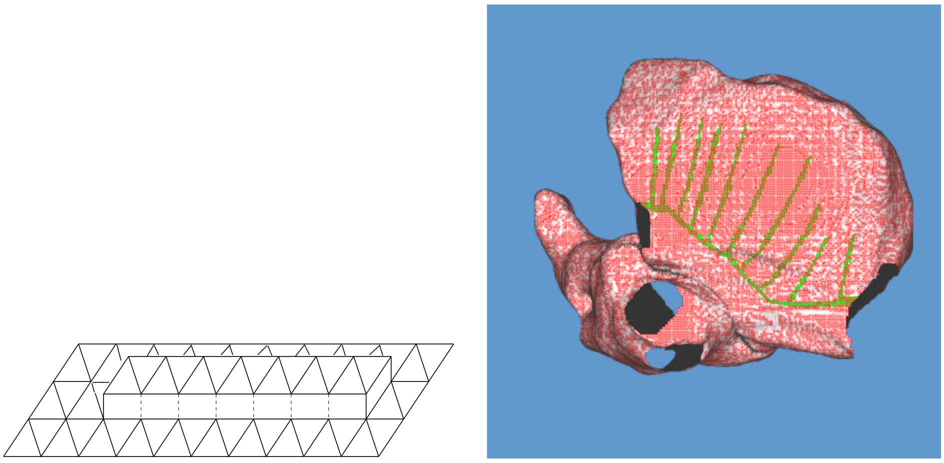

Figure 6.7: *Crista terminalis and pectinate muscles in our atrial model.* **Left***: Crista terminalis and pectinate muscles are modeled as triangle strips on top of the atrial wall that are connected to the wall at their beginning and end and to some degree in between.* **Right***: Crista terminalis and pectinate muscles as they have been incorporated into our triangle mesh. They are both represented by green triangles and treated identically.*

6.2.4 Putting it All Together

Besides the geometrical aspects of our atrial model just discussed, the other major ingredient is the description of the electrophysiology of the atrial cells. Here we use the reformulated Courtemanche model that we developed in the preceding Chapter. Our dynamical equations are therefore:

$$\begin{aligned} \frac{\partial V(x,t)}{\partial t} &= f(V,\mathbf{s}) + \nabla \cdot (D \nabla V) \qquad (6.1) \\ \frac{\partial \mathbf{s}(x,t)}{\partial t} &= g(V,\mathbf{s}), \end{aligned}$$

where V is the transmembrane potential, $\mathbf{s}$ is the vector of gating variables of the simplified model, and D is the diffusion tensor (reflecting the fiber orientation of the atria). The functions f and g specify our tissue model. In the language of physical chemistry, f and g describe reactions, $\nabla \cdot (D \nabla V)$ describes diffusion, and the system of Eqs. 6.1 is called a *reaction-diffusion* system.

6.3 Numerical Methods

The reaction terms of Eq. 6.1 are easy to deal with. In the first equation, we use a forward Euler method to update V in every time step. The contribution of f to the change of V is simply evaluated. In the second equation, all gating variables relax exponentially towards their equilibrium value. Therefore, we do not use the forward Euler method here but an algorithm developed by Rush and Larsen [115] that anticipates the exponential development of the gating variables during the time step.

The diffusion operator in Eq. 6.1 is harder to approximate. The principal choice of methods is between finite element, finite difference and finite volume methods.

In finite element methods, one introduces *base functions* that differ from zero only in a very limited region, typically the direct neighborhood of a vertex. Functions in the vector space spanned by the base functions are considered possible states of the system, and by partially integrating Eq. 6.1 one gains a linear equation that implicitly determines the state of the system after one time step. Finite element method have a solid theoretical foundation and, being implicit, converge even for comparatively large time steps. However, implicit methods have been seen to cause spurious fronts in reaction-diffusion systems.

In finite difference methods, the idea is to approximate operators by a linear combination of the function values at a mesh point and its neighbors. The coefficient of a neighbor in this linear combination is called its *weight*. These methods are simple and usually robust, but their convergence properties are not as good as those of implicit methods and it is sometimes nontrivial to find good weights sets for the vertices of an irregular mesh. Finite volume methods try to combine the advantages of both methods by integrating Eq. 6.1 over some volume and then formulating either an implicit or an explicit scheme for the resulting equation.

We have chosen to use a finite volume explicit scheme. The large time steps possible in implicit methods do not help as much as we need short time steps because of reaction anyway.

We start using a simple method of estimating the diffusion operator in Eq. 6.1 which builds on Gauss' theorem. For each vertex p_i , we consider the neighborhood N of triangles that contain p_i. Then we assume that V is linear on each triangle. Then $\nabla \cdot (D\nabla V)$ can be approximated using Gauss' law:

$$\nabla \cdot (D\nabla V)_i \approx \frac{1}{A(N)} \sum_{j=1}^{\#neighb.} < n_j, D_{i,j}\text{gradV} >, \tag{6.2}$$

where $A(N)$ is the area of N.

While this method yielded reasonable results in our first simulations, it has a deficiency. In certain simple, regular grids it computes seriously wrong weights (Fig. 6.9). We therefore modified it in the following way. We still assume constant gradient on each triangle, but we now consider the inflow into each *edge*. The inflow into an edge is translated into a lift of the edge by computing the amount of charge needed to lift the edge by one unit preserving the linearity of V (see Fig. 6.10). We call this method the *edge flow* method. The main advantage over the Gauss method is that the edge flow method takes into account a larger neighborhood of triangles and is therefore less sensitive to systematic variations in triangle neighborhood size (as in Fig. 6.9). For all simple triangulation patterns of the plane we tested (Fig. 6.9, hexagonal and several others), the edge flow method yields the analytically correct result.

To further test the method we studied the effect of randomly displacing

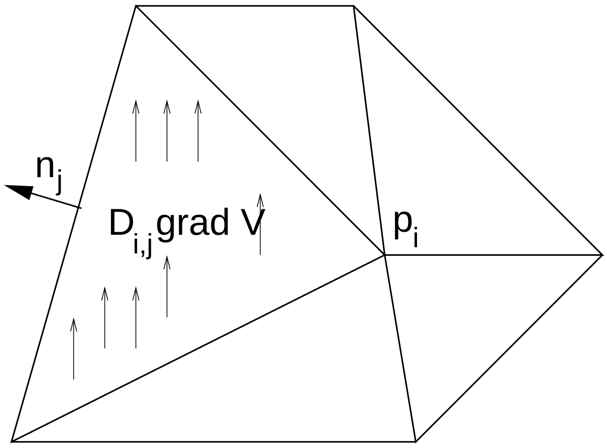

Figure 6.8: *Diffusion estimation according to the Gauss method. For each triangle* $t_{i,j}$ *containing the vertex* p_i*, we assume that* V *is linear and therefore that the flow* $D_{i,j}\nabla V$ *is constant. Then the flow over the edge of* $t_{i,j}$ *that is opposing* p_i *is* $< n_j, D_{i,j}\nabla V >$*, where* n_j *is the normal of the edge opposing* p_i*. Summing the outflow over all triangles containing* p_i *and dividing by the total area of the triangles gives an approximation of* $\nabla \cdot (D\nabla V)$*.*

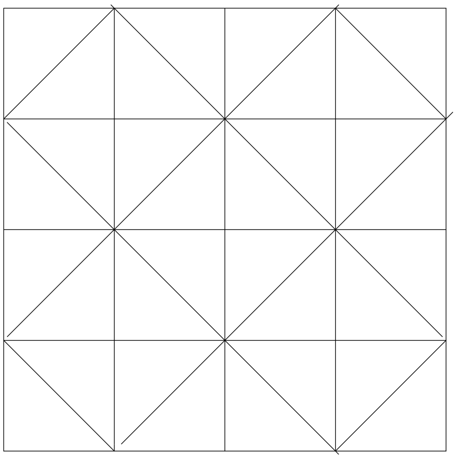

Figure 6.9: *A simple grid for which the Gauss algorithm computes significantly wrong weights. At points with 4 edges, the Gauss algorithm correctly approximates the diffusion operator by a coefficient of -4 for the central point and -1 for the neighbors. At points with 8 edges, the approximation incorrectly yields a central weight of -2.*

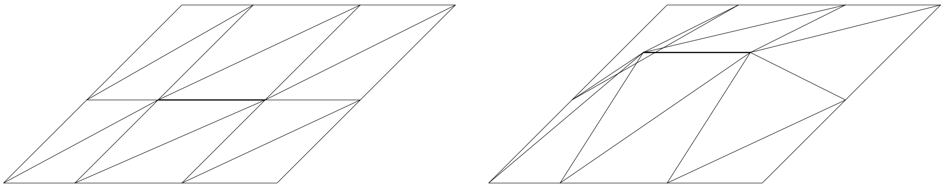

Figure 6.10: *The relation between charge inflow into an edge and the lift of that edge. If we require the transmembrane voltage V to be a linear function on our triangular mesh, the value of V along an edge may only be increased in the manner shown in the Figure. This makes possible the computation of a conversion factor between inflow and lift for a given edge.*

Noise level	Conduction velocity [cm/s]
0.0	80.3
0.1	81.9
0.2	84.0

Figure 6.11: *The effect of random displacements of grid vertices on conduction velocity for plane waves. Starting from a hexagonal grid with a grid constant of 1, we add equally distributed noise of a certain amplitude to the vertex coordinates and measure the time needed for the front to propagate over 2.25 cm. The space step used is 0.25 mm, the time step is 0.02 ms.*

vertices on wave propagation. If propagation speed is not much affected by such displacements, we have reason to believe that wave propagation on our atrial surface with irregular geometry is adequately computed as well. We simulate wave propagation in a plane rectangular sheet and an initially regular grid (where the weights of the edge flow method resemble the well-know (-4,1,1,1,1)-approximation of the Laplacian). Then we add equally distributed white noise of uniform amplitude to the coordinates of the grid and repeat the simulation. Tab. 6.11 shows the results for different noise amplitudes. Conduction velocity increases by less than 5 % for a noise level of 0.2, which leads to a grid that is less regular than our atrial mess. We also test whether isotropy in wave propagation is preserved if noise is added. For this, we induce an excitation in the middle of a quadratic excitable sheet and compare the arrival times at the different edges. The results are shown in Tab. 6.12. Once more, we see that the influence of grid irregularities is minimal.

We conclude that the edge flow method is a reasonable model of wave propagation on a triangular mesh. With the numerical method specified, our model is ready for use in simulations. The model properties are summarized in Tab. 6.13.

6.4 Results

We use our model to simulate two important rhythms of the heart. The first is the sinus rhythm, the standard rhythm of the healthy heart. It should be the first rhythm simulated in any realistic model, because there are more experimental studies on the activation sequence of the sinus rhythm than of

Noise level	Mean cond. vel. [cm/s] Upwards	Left	Right	Downwards
0.0	76.6	76.6	76.6	76.6
0.1	79.6	79.4	79.1	78.8
0.2	80.5	80.6	80.8	81.0

Figure 6.12: *The effect of random displacements of grid vertices on the isotropy of conduction velocity for plane waves. Starting from a hexagonal grid, we add equally distributed noise of a certain amplitude to the vertex coordinates and measure the time needed for a point excitation in the middle of the grid to the different edges. The space step used was 0.25 mm, the time step 0.02 ms.*

Vertices	298000
Triangles	594000
-Fiber structure-	
Average space step	0.28 mm
Time step	0.02 ms
Numerical efficiency	12s real time for 1ms model time on a Pentium IV - 2 Ghz (isotropic case)

Figure 6.13: *Overview of our atrial model.*

any other rhythm. In the second simulation, we confirm that our model supports the induction of spiral waves and spiral breakup, a possible mechanism for the most dangerous arrhythmia in the atria, atrial fibrillation. Finally, we demonstrate how our model can be used to quantify the effect of anisotropy.

6.4.1 Sinus Rhythm

Fig. 6.14 shows the excitation sequence during sinus rhythm in our model. At $t = 0$ ms, we apply a stimulus current to the sinus node, right of the vena cava superior. Within 30 ms, excitation reaches the left atrium. The end of the crista terminalis at the vena cava inferior is reached after 53 ms and the right atria are fully depolarized after 121 ms. The septum is reached after 39 ms and completely activated after 93 ms. The last part of the atria to be excited is the left appendage after 125 ms. The conduction velocity in the free atrial wall greatly varies between about 40 cm/s and 100 cm/s. In the crista terminalis, a typical value of conduction velocity is 120 cm/s.

6.4.2 Atrial Fibrillation

One of the candidate mechanisms for the development of atrial fibrillation is that a precisely timed extrasystole creates a spiral wave that later breaks up into many spirals. We tried to reproduce this phenomenon in our model, placing extrasystoles at different times and locations right after the preceding wave had passed. For most times and locations of an extra systole, we did not get reentrant waves, but the waves immediately collided and vanished, because the space available for the two developing arms to turn around was too small. With some experience, we were successful in initiating a double spiral wave, as shown in Fig. 6.15. Once a spiral wave is established, the wavelength of the excitation waves decreases because recovery time is reduced. After three rotations, we see breakup. The breakup occurs precisely where the septum meets the atrial wall, which probably means that the wave broke due to the increased efflux at this place.

6.4.3 The Effect of Anisotropy

To assess the effect of anisotropy on the activation sequence, we compare the standard version of our model to a version that has no special conduction pathways and isotropic diffusion (see Fig. 6.16). The shape of the excited

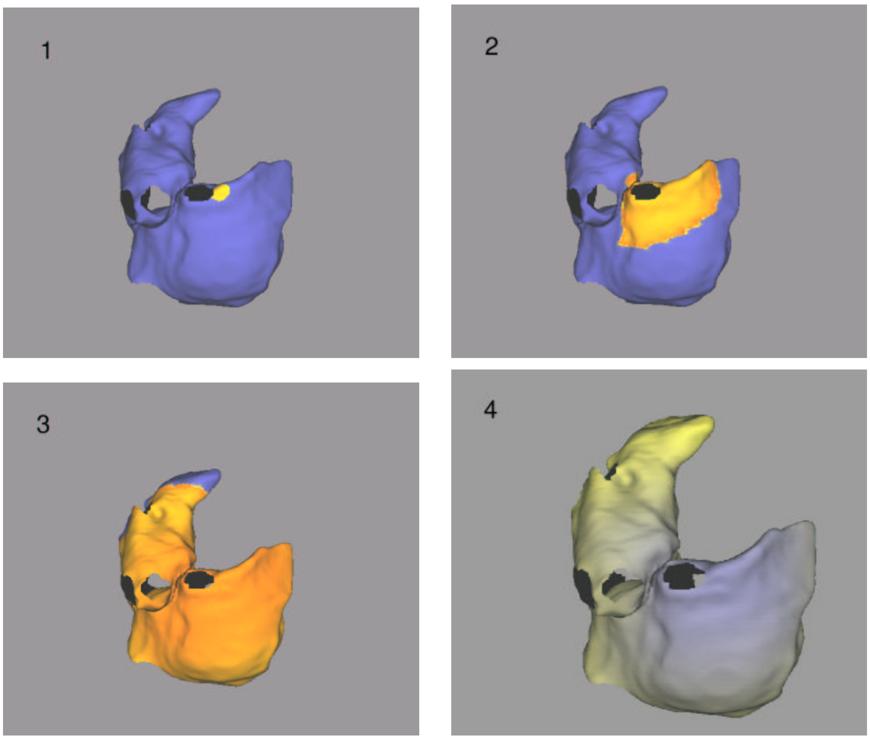

Figure 6.14: *The sinus rhythm in our atrial model. The view is from above. The hole next to the red spot in the first picture is the superior vena cava. Color encodes transmembrane voltage, blue representing resting potential and red maximal depolarization. Snapshots have been taken after 0 ms, 30 ms, 100 ms, and 220 ms.*

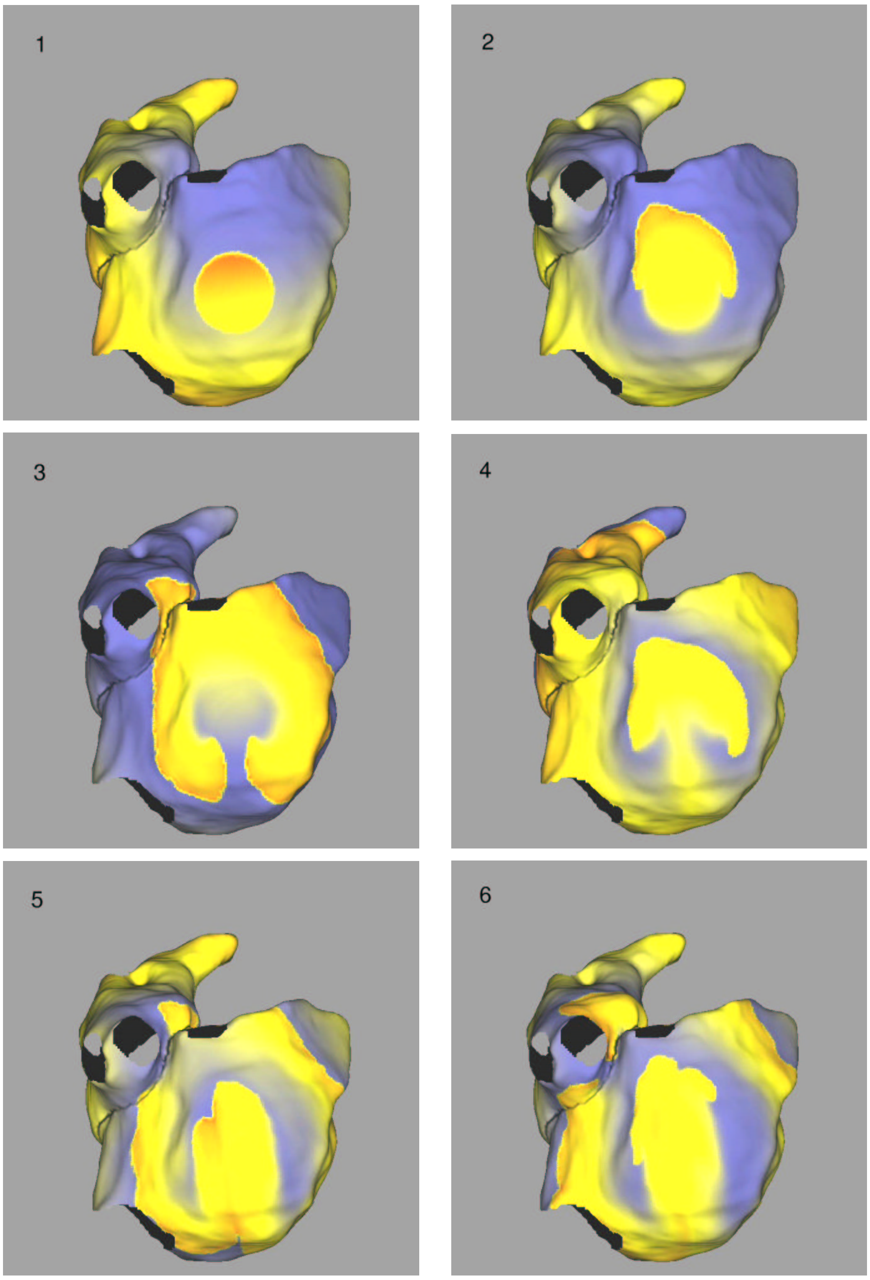

Figure 6.15: *Spiral breakup in our model. The view is from behind, slightly to the right. At* $t = 0$*ms the sinus node is excited (not shown). At* $t = 225$ *we apply an extra stimulus in the right atrial wall, such that it extends into the refractory region of the preceding wave (upper left panel). The following panels show state of the atria after* $t = 250$ *ms, 300 ms, 375 ms, 575 ms, and 600 ms (see text for details).*

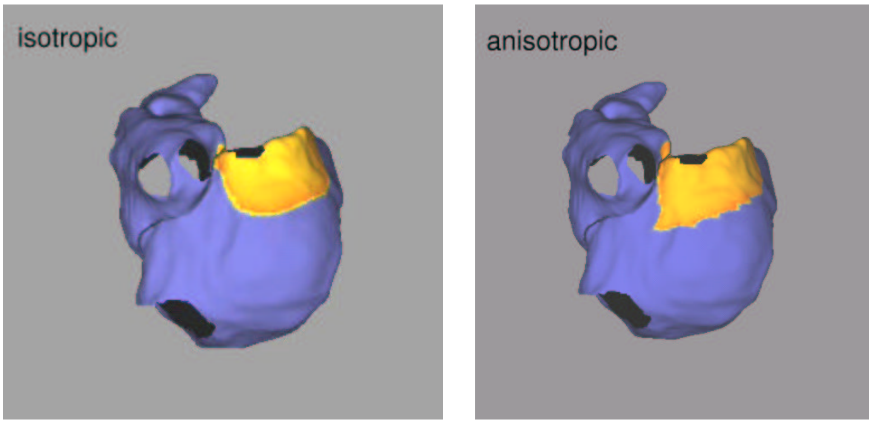

Figure 6.16: *The effect of anisotropy in our model. Left panel shows isotropic propagation of excitation (anisotropy ratio set to 1), while the right panel shows propagation with our standard anisotropy ratio of 3 and with pectinate muscles and crista terminalis. Both panels have been recorded 30 ms after stimulation.*

region loses the triangular shape typical for anisotropic excitation and key activation times change by up to 20 %.

6.5 Discussion

We have developed a realistic and efficient model of excitation propagation in the human atria from scratch. This is the first atrial model that includes both anisotropy as well as special conduction pathways.

With tissue resistivity as the only free parameter, we are able to achieve an activation sequence that is mostly consistent with experimental findings. The total activation time in experiments was between 114 ms [73] and slightly above 120 ms [14]. The completion of septum activation is reported to occur after 85 ms [14], compared to 79 ms in our model. Total activation times for the right atrium range around 80 ms [14, 24], which is significantly below the roughly 120 ms we model. We attribute this difference at least partly to the fact that the right atrium of our data set (the Visible Female) is unusually large, which prolongs excitation. The reported conduction velocities in the free wall lie in the range from 68 to 103 cm/s [50] where we found 40 to 100 cm/s. For the canine pectinate muscles, 117 cm/s 154 cm/s were measured

[52], compared to our 120 cm/s. The point of last activation has been reported to be the the left atrial appendage by Durrer [27], which agrees with our findings, while Canavan reports it is the posterior left atrium [14].

One important reason to develop realistic models is to understand the development of dangerous arrhythmias. We could show that it is difficult but possible to induce spiral waves in our atrial model by applying an adequately timed stimulus. The possibility of inducing a spiral wave is not at all obvious, considering that the wavelength of the excitation wave in quiescent medium ($\approx$ 15 -20 cm) is larger than the atria. If spirals were easily inducable in our model, this would actually draw the model quality into question, as the tachycardias associated with spiral waves do not usually occur in healthy people.

Finally we showed that our model allows us to quantify the effect of anisotropy. Removing anisotropy qualitatively changes the activation sequence. The possibility of easily eliminating model features at will is of great help in deciding whether certain simplifications can be legitimately made.

There are limitations to our model. While we deliberately chose to model the atria as two-dimensional objects, we cannot exclude the possibility that there are effects due to the non-zero thickness of the atrial wall. Also our triangle mesh does not yet have a satisfying quality. Some triangles resulting from the Generalized Marching Cubes Algorithm are not close to equilateral produce large diffusion weights, which forces us to decrease our time step. While we eliminated the worst triangles with simple algorithms, it would be significantly better to resample the surface with a higher-quality grid.

Summary

In this thesis, we made several contributions to the understanding of atrial arrhythmias. Our major goal was the development of a realistic and efficient model of wave propagation in the atria. In a number of studies, we prepared this project and then built the model in the final two Chapters.

We started with the simplest setting of arrhythmogenesis, with a single heart cell that is paced at increasing frequency. Up to a critical frequency, the cell respond with a 1:1 pattern. We studied this loss of 1:1 response for fast pacing in the Beeler-Reuter model and find that the 1:1 rhythm is replaced by either alternans or a 2:1 rhythm, consistent with experiments with heart cells. We found hysteresis and bistability in the onset of alternans/2:1 rhythms and study the possibility of avoiding alternans by blocking the different ionic currents. Finally, we develop a simple model of calcium buffers within the cell and show that these buffers promote the genesis of alternans.

We went on to study a new mechanism of genesis of instabilities in wave propagation that may be related to the development of atrial arrhythmias. In former studies, it was shown that many instabilities can be understood in terms of the restitution curve, which was universally assumed to be monotonically increasing. From experiments with atrial cells it is suggested that loss of this monotonicity is connected with the atria's susceptibility of arrhythmias. We therefore studied if there are similar connections between restitution curve and instabilities in the case of negative restitution as previously found for positive restitution. Indeed, we find that instabilities are to be expected if the restitution curve has a slope steeper than -1 (as opposed to 1 in the case of normal restitution). Under periodic forcing of a single cell, the negative restitution instability is associated with a saddle-node bifurcation, and results in successive (unbounded) increase of APD, while the alternans instability is associated with a supercritical flip bifurcation and results in APD oscillations. In a delayed integral equation model of a ring of cells,

we show that upon shortening the ring, the negative restitution instability occurs via an inifinite-dimensional bifurcation and, using linear analysis, we find that high-frequency modes grow fastest right after the loss of stability. Numerically, we show that the bifurcation has similarity with a subcritical Hopf bifurcation (opposed to a supercritical bifurcation for normal restitution). In two dimensions, we find that spiral breakup is less pronounced than in media with positive restitution This may be the consequence of an effect we found, that spiral waves in media with negative restitution tend to adapt their diastolic interval such that the slope of the restitution curve is about -1. In contrast, spiral waves in media with positive restitution tend to minimize their diastolic interval, so that the absolute value of the slope of the restitution curve becomes much higher. Our study was designed to bring out the effects of negative restitution as clearly as possible, so we chose the restitution curves studied accordingly. It will be exciting to see which of the mechanisms we describe occur in atrial tissue or with restitution curve that closely resemble atrial electrophysiology.

An important fundamental question for the study of wave propagation in general is how coupling of cells is modeled. The generally accepted way of modeling cell coupling violates charge conservation. We studied the effect of this violation on wave propagation. We show the effect is minimal for homogeneous media but may become significant around heterogeneities of the medium. We propose that each diffusion of voltage should be accompanied by a corresponding ion flow, which ensures charge conservation.

An important prerequisite for an efficient and realistic model of wave propagation in the atria is a good model of electrophysiology. Unfortunately the most accurate descriptions of any type of heart cell are excessively complicated and computationally expensive. We developed a general way to drastically decrease the complexity of such models (by a factor of 3-4) while retaining the properties important for wave propagation closely and applied it to one of the most detailed models of atrial electrophysilogy available [21]. We adiabatically eliminated most of the fast gating variables, showed a way to combine several gating variables into one, and removed the intracellular calcium buffering. With a few parameter changes we can restore with good accuracy the widely accepted characteristics of wave propagation: The restitution curve, the dispersion (or conduction velocity restitution) curve, and action potential shape. Even spiral wave characteristics (period, shape, tip trajectory) are similar. We then use our method to study the effect of atrial remodeling on spiral wave properties and find that spiral waves are more stable in remodeled tissue and have a shorter period.

Finally, we developed a model of wave propagation in the human atria, including realistic geometry and electrophyiology. We started from scratch with voxel data from the Visible Human Project, from which we constructed the atrial surface as a triangular mesh. To this mesh we added local fiber orientation, a vector for each triangle, and triangle strips describing special conduction pathways (pectinate muscles and crista terminalis). Combining this realistic anatomy with the reformulated Courtemanche model of electrophysiology developed earlier, we obtain a realistic atrial model. We find and test an efficient numerical method to solve the resulting reaction-diffusion equations and are for the first time able to compute a realistic simulation of a whole atrial excitation within hours. We show that our model yields an activation sequence that is mostly consistent with experimental findings, even though we only adjust a single free parameter. In our model, spiral waves may be induced by extrasystoles, but the timing and placing is crucial. This is consistent with the fact that atrial tachycardias are much less common than atrial extrasystoles. Finally, we demonstrate how our model can be used to quantify the effect of certain model features by comparing isotropic and anisotropic wave propagation.

All these studies are but small steps toward the greater goal of constructing a virtual heart and reaching a true understanding of the mechanism underlying the genesis of dangerous arrhythmias. Great challenges remain on the way to this goal, e.g. interaction of electrophysiology, mechanic, and fluid dynamic aspects of the heart. Yet there has been substantial progress in heart modeling over the last years, so there is hope that we can soon more effectively fight diseases of the heart.

Deutsche Zusammenfassung

Herzrhythmusstörungen sind eine der häufigsten Todesursachen in der westlichen Welt. Deshalb wurden ihre Ursachen in den letzten Jahrzehnten intensiv von Kardiologen und Physiologen erforscht. Die Ergebnisse dieser Forschung können nun mit Methoden aus Mathematik und Physik einerseits und moderner Computerleistung andererseits kombiniert werden. So wird eine *quantitative* Beschreibung des Herzens möglich, die eine wesentlich genauere Diagnose und Therapie von Herzkrankheiten erlauben würde. In der vorliegenden Arbeit wird die Entstehung von Herzrhythmusstörungen modelliert.

Die Modellierung des gesamten Herzens ist gleichzeitig eine langfristige Aufgabe und ein vielversprechender Weg, Herzkrankheiten zu bekämpfen. Das Herz besteht aus mehreren Milliarden gekoppelter Zellen in einer komplexen räumlichen Anordnung. Jede Zelle kann elektrisch erregt werden und zieht sich dann wenig später als Folge biochemischer Prozesse zusammen. Da die Zellen gekoppelt sind, können sich Erregungen ausbreiten, das ist die Grundlage für die Funktion des Herzens. Der genaue zeitliche Ablauf der Erregungsausbreitung ist entscheidend für die Effektivität des Herzens, und es gibt viele spezielle anatomische Strukturen, die die Erregungsausbreitung modifizieren. Die Mechanismen der Erregungsausbreitung stehen in Wechselwirkung mit der Mechanik und der Fluiddynamik des Herzens. Die Modellierung des gesamten Herzens ist also voller Herausforderungen, und es wird noch lange dauern, bis ein Modell vorliegt, das alle wesentlichen Aspekte des Herzens mit ihren Wechselwirkungen befriedigend beschreibt. Das Hinarbeiten auf solche Modelle ist aber notwendig, weil sie einerseits für ein quantitatives Verständnis der Funktion des Herzens unverzichtbar sind und andererseits einen Rahmen bieten, in dem therapeutische Methoden getestet werden können. Zur Zeit werden die elektrischen, mechanischen und hydrodynamischen Aspekte des Herzens allgemein noch getrennt modelliert um die Komplexität zu begrenzen. Das gilt auch für diese Dissertation: Wir betrachten das Herz und seine Zellen als elektrisch erregbar, aber weder das Herz selbst noch das Blut in ihm bewegen sich.

Die kleinsten elektrisch erregbaren Untereinheiten des Herzens sind einzelne Herzzellen. Die Rhythmen dieser Bausteine zu verstehen ist eine wichtige Voraussetzung zum Verständnis der Arrhythmien des gesamten Herzens. Die elektrischen Eigenschaften von Herzzellen sind detailliert charakterisiert worden, und die Rhythmen, die man durch verschiedene Stimulationen in ihnen erzeugen kann, wurden in zahlreichen Experimenten erforscht. Allerdings würde selbst ein voll-ständiges Verständnis der einzelnen Zelle nicht genügen, um die Arrhythmien des ganzen Herzens zu verstehen. Der Rhythmus des Herzens ist genau genommen das raumzeitliche Muster der Kontraktion des Herzens. Dieses Muster wird durch die Erregungsausbreitung auf dem Herz erzeugt und hängt stark von der räumlichen Anordnung der Zellen ab.

Erregungsmuster im Herzen können in Modellen verschiedener Komplexität untersucht werden. In einfachen Modellen kann man den Mechanismus verstehen, der der Erregungsausbreitung im Herzen zugrunde liegt. Dieser Mechanismus besteht auch in anderen Systemen als dem Herz, die dann allgemein als *erregbare Medien* bezeichnet werden. Erregbare Medien sind der theoretische Rahmen in dieser Dissertation und der Modellierung von Erregungsausbreitung im Herz im allgemeinen. Bestimmte Erregungsmuster, zum Beispiel Spiralwellen, wurden in vielen erregbaren Medien gefunden und ihre Dynamik kann inzwischen in gewissem Maße theoretisch erklärt werden. Ein großer Teil der Modellierung des Herzens beschäftigt sich mit der Frage, welche der in erregbaren Medien bekannten Erregungsmuster auch im Herzen bestehen und wie ihre Dynamik im Herz funktioniert.

Die vorliegende Arbeit beschäftigt sich mit der Entstehung von Herzrhythmusstörungen in verschiedenen Zusammenhängen, von einzelnen Herzzellen bis zu einem anatomischen Modell der menschlichen Vorhöfe.

In Kapitel 2 wird ein periodisch stimuliertes Ionenmodell für menschliche Herzzellen untersucht. Bei langsamer Stimulation generieren die Herzzellen ein Aktionspotenzial pro Stimulus, aber dieser Rhythmus kann nur bis zu einer kritischen Stimulationsfrequenz aufrecht erhalten werden. Oberhalb dieser kritischen Frequenz entsteht typischerweise ein Rhythmus der Periode 2, entweder ein 2:1-Rhythmus, bei dem nur jeder zweite Stimulus ein Aktionspotential auslöst, oder ein 2:2-Rhythmus, der auch Alternanz genannt wird, bei dem sich zwei verschiedene Aktionspotentiale abwechseln. Wir untersuchen die Entstehung von Rhythmen der Periode zwei im Beeler-Reuter-

Modell für Kammergewebe und finden Hysterese und Bistabilität beim Einsetzen von Alternanz. Wir bestimmen quantitativ, wie erfolgreich sich die Entstehung von Alternanz durch gezieltes Blocken von Ionenströmen verhindern lässt. Schließlich entwickeln wir ein einfaches Modell für die intrazellulären Kalziumspeicher, an dem wir zeigen können, dass solche Speicher die Entstehung von Alternanz begünstigen.

In Kapitel 3 untersuchen wir die Stabilität von Erregungspulsen und Spiralwellen in erregbaren Medien mit einer speziellen Eigenschaft, die negative Restitution genannt wird. Negative Restitution bedeutet, dass für bestimmte Längen des diastolischen Intervals (Ruhezeit zwischen zwei Erregungen), die Aktionspotenzialdauer für wachsende diastolische Intervalle geringer wird. Diese ungewöhnliche Eigenschaft wurde in Herzzellen gefunden, die für chronische Arrhythmien em-pfänglich sind. Wir untersuchen, wie negative Restitution zu Instabilitäten bei eindimensionaler Erregungsausbreitung und in Spiralwellen führen kann. Es zeigt sich, dass Instabilitäten auftreten, wenn die Steigung der Restitutionskurve (Aktionspotentialdauer als Funktion der Länge des diastolischen Intervals) steiler als -1 wird, analog zu Instabilitäten in Medien mit positiver Restitution, die für Steigungen der Restitutionskurve steiler als 1 auftreten.

In Kapitel 4 behandeln wir die Effekte einer Verletzung der Ladungserhaltung, die in einer beliebten Klasse von Ionenmodellen entdeckt wurde und viele abgeschlossene Studien betrifft. Wir bestimmen quantitativ den Zusammenhang zwischen der Größe der Verletzung der Ladungserhaltung und der Verschiebung des Ruhezustands der Zelle. Mit diesem Maß zeigen wir, dass der Effekt der Verletzung in homogenen Medien nur gering ist, in heterogenen Medien aber signifikant werden kann. Abschließend geben wir ein Modell für Wellenausbreitung in den betroffenen Ionenmodellen an, das die Ladungserhaltung berücksichtigt.

In Kapitel 5 entwickeln wir eine Methode zur Reduktion der Komplexität von Ionenmodellen. Mit dieser Methode formulieren wir ein detailliertes Modell für Vorhofzellen von Courtemanche et al. neu, so dass der rechnerische Aufwand stark sinkt. Durch adiabatische Elimination schneller Variabler, Zusammenfassung verschiedener Variabeln und Entfernung der intrazellulären Kalziumdynamik wird die Simulationsgeschwindigkeit etwa vervierfacht. Dennoch können wir durch Anpassen der Modellparameter die für die Wellenausbreitung wichtigen Eigenschaften gut reproduzieren. Wir benutzen das beschleunigte Modell, um die Effekte von “Remodeling”, einer langfristigen Veränderung der Elektrophysiologie von Vorhofzellen bei chronischem Vorhofflimmern, auf die Dynamik von Spiralwellen zu verstehen. Wir kommen zu dem Ergebnis, dass Spiralwellen in dem veränderten Vorhofgewebe schneller und deutlich stabiler sind als in normalem Vorhofgewebe.

Das Hauptprojekt dieser Arbeit ist die Entwicklung eines realistischem Modells der Erregungsausbreitung auf den menschlichen Vorhöfen. In Kapitel 6 rekonstruieren wir die Oberfläche der Vorhöfe aus anatomischen Daten. Wir erweitern diese Oberfläche um die lokale Faserorientierung an jedem Punkt und um das Leitungssystem der Vorhöfe für elektrische Reize. Zusammen mit dem elektrophysiologischen Modell, dass wir in Kapitel 5 entwickelt haben, ergibt dies ein realistisches und gleichzeitig numerisch effektives Modell für die menschlichen Vorhöfe. Dieses Modell benutzen wir, um die Erregungsabfolge im gesunden Herzen zu untersuchen und finden gute Übereinstimmung mit vorhandenen experimentellen Daten. Wir zeigen außerdem einen möglichen Mechanismus für die Entstehung von Kammerflimmern, der gefährlichsten Arrhythmie in den Vorhöfen, in unserem Modell. Durch genau platzierte Extrasystolen zu bestimmten Phasen der Erregungsausbreitung können Spiralwellen erzeugt werden, die dann in kompliziertere Muster aufbrechen. Schließlich zeigen wir, wie in unserem Modell die Wirkung von Anisotropie demonstriert werden kann.

Alle diese Studien sind nur kleine Schritte auf dem Weg zu dem Ziel, ein virtuelles Herz zu erschaffen und tiefes Verständnis der Mechanismen hinter gefähr-lichen Arrhythmien zu erreichen. Viele große Herausforderungen, wie etwa das Zusammenspiel von Elektrophysiologie, Mechanik und Fluiddynamik, bleiben bestehen. Dennoch hat die Modellierung des Herzens in den letzten Jahren große Fortschritte gemacht, so dass die Chance besteht, dass Herzkrankheiten mit Hilfe von Herzmodellen bald effektiver bekämpft werden können.

Bibliography

[1] S. Abboud, O. Berenfeld, and D. Sadeh. Simulation of high-resolution QRS complex using a ventricular model with a fractal conduction system. *Circ Res*, 68:1751–1760, 1991.

[2] M. Allessie, J. Ausma, and U. Schotten. Electrical, contractile and structural remodeling during atrial fibrillation. *Cardiovasc Res*, 54(2):230–46, May 2002.

[3] M. A. Allessie, F. I. M. Bonke, and F. J. G. Schopman. Circus movement in rabbit atrial muscle as a mechanism of tachycardia. *Circ Res*, 33:54–62, 1973.

[4] G. J. Anderson, K. Greenside, and C. Fisch. Electrophysiologic studies on Wenckebach structures below the atrioventricular junction. *Am J Cardiol*, 30:232–236, 1972.

[5] H. Arce, A. Xu, H. Gonzales, and M. Guevara. Alternans and higher-order rhythms in an ionic model of a sheet of ischemic ventricular muscle. *Chaos*, 268:411–426, 1977.

[6] M. Asano and Y. Nomura. Ca^{2+} movement from leaky sarcoplasmic reticulum during contraction of rat arterial smooth muscles. *Eur J Pharmacol*, 404:327–329, 2000.

[7] G. W. Beeler and H. Reuter. Reconstruction of the action potential of ventricular myocardial fibres. *J. Physiol. (Lond.)*, 268:177–210, 1977.

[8] B. P. Belousov. Periodically acting reaction and its mechanisms. *Sbornik Referatov po Radiatsionnoy Meditsine*, page 145, 1959.

[9] R. M. Berne and M. N. Levy, editors. *Physiology.* Mosby Year Book, 3rd edition, 1993.

[10] O. Bernus, R. Wilders, C. W. Zemlin, H. Verschelde, and A. V. Panfilov. A computationally efficient electrophysiological model of human ventricular cells. *Am J Physiol Heart Circ Physiol*, 282(6):H2296–308, Jun 2002.

[11] O. Blanc, N. Virag, J.-M. Vesin, and L. Kappenberger. A computer model of human atria with reasonable computation load and realistic anatomical properties. *IEEE Trans Biomed Eng*, 48:1229–37, 2001.

[12] M. E. Brandt, H. Shih, and G. Chen. Linear time-delay feedback control of a pathological rhythm in a cardiac conduction model. *Phys Rev E*, 56(2):R1334–R1337, 1997.

[13] A. J. Camm. *Nonpharmacological Treatment of Atrial Fibrillation*. Futura, 1997.

[14] T. E. Canavan, R. B. Schuessler, J. P. Boineau, P. B. Corr, M. E. Cain, and J. L. Cox. Computerized global electrophysiological mapping of the atrium in patients with Wolff-Parkinson-White syndrome. *Ann. Thorac. Surg.*, 46:223–231, 1988.

[15] T. R. Chay. Proarrhythmic and antiarrhythmic actions of ion channel blockers on arrhythmias in the heart: model study. *Am J Physiol*, 271(1 Pt 2):H329–56, 1996.

[16] P. S. Chen, P. Wolf, E. G. Dixon, N. D. Danieley, D. W. Frazier, W. M. Smith, and R. E. Ideker. Mechanism of ventricular vulnerability to single premature stimuli in open-chest dogs. *Circ. Res.*, 62:1191–1209, 1988.

[17] E. M. Cherry, H. S. Greenspan, and C. S. Henriquez. A space-time adaptive method for simulating complex cardiac dynamics. *Phys Rev Lett*, 84:1343–1346, 2000.

[18] D. R. Chialvo, R. F. Gilmour, and J. Jalife. Low dimensional chaos in cardiac tissue. *Nature*, 343:653–656, 1990.

[19] M. Courtemanche, L. Glass, and J. P. Keener. Instabilities of a propagating pulse in a ring of excitable media. *Phys Rev Lett*, 70:2182–2185, 1993.

[20] M. Courtemanche, J. P. Keener, and L. Glass. A delay equation representation of pulse circulation on a ring of excitable media. *SIAM J. App Math*, 56:119–142, 1996.

[21] M. Courtemanche, R. J. Ramirez, and S. Nattel. Ionic mechanisms underlying human atrial potential properties: insights from a mathematical model. *Am J Physiol*, 275:H301–H321, 1998.

[22] M. Courtemanche, R. J. Ramirez, and S. Nattel. Ionic targets for drug therapy and atrial fibrillation-induced electrical remodeling: insights from a mathematical model. *Cardiovasc. Res.*, 42:477–489, 1999.

[23] M. Courtemanche and A. T. Winfree. Re-entrant rotating waves in a Beeler-Reuter based model of two-dimensional cardiac activity. *Int. J. Bif. and Chaos*, 1:431–444, 1991.

[24] J. L. Cox, T. E. Canavan, R. B. Schuessler, M. E. Cain, B. D. Lindsay, C. Stone, P. K. Smith, P. B. Corr, and J. P. Boineau. The surgical treatment of atrial fibrillation, II: intraoperative electrophysiological mapping and description of the electrophysiologic basis of atrial flutter and atrial fibrillation. *J. Thorac. Cardiovasc. Surg.*, 201:406–426, 1991.

[25] J. M. Davidenko, A. M. Pertsov, R. Salomontsz, W. Baxter, and J. Jalife. Stationary and drifting spiral waves of excitation in isolated cardiac muscle. *Nature*, 355:349–351, 1991.

[26] D. DiFrancesco and D. Noble. A model of cardiac electrical activity incorporating ionic pumps and concentration changes. *Phil. Trans R. Soc. Lond. B*, 307:353–398, 1985.

[27] D. Durrer, R. T. Dam, G. E. Freud, M. U. Janse, F. L. Meijler, and R. C. Arzbaecher. Total excitation of the isolated human heart. *Circulation*, 41:899–912, 1970.

[28] R. El-Sherif, R. R. Hope, B. J. Scherlag, and R. Lazara. Re-entrant ventricular arrhythmias in the late myocardial infarction period. *Circulation*, 55:702–718, 1977.

[29] V. Elharrar, H. Atarashi, and B. Surawicz. Cycle length-dependent action potential duration in canine cardiac purkinje fibers. *Am. J. Physiology*, 247(6 Pt 3):H936–45, 1984.

[30] L. P. Endresen and N. Skarland. Limit cycle oscillations in pacemaker cells. *IEEE Transactions on Biomedical Engineering*, 47:1134–1137, 2000.

[31] D. E. Euler. Cardiac alternanns: mechanisms and pathophysiological significance. *Cardiovasc. Res*, 42:583–590, 1999.

[32] G. M. Faber and Y. Rudy. Action potential and contractility changes in Na_i^{2+} overloaded cardiac myocytes: a simulation study. *Biophys J*, 78:2392–2404, 2000.

[33] R. FitzHugh. Mathematical model of threshold phenomena in the nerve membrane. *Bull. Math. Biophys.*, 17:257–278, 1955.

[34] R. FitzHugh. Thresholds and plateaus in the Hodgkin-Huxley nerve equations. *J. Gen. Physiol.*, 43:867–896, 1960.

[35] M. Franz, J. Schaefer, M. Schóttler, W. Seed, and M. Noble. Electrical and mechanical restitution of the human heart at different rates of stimulation. *Circ Res*, 53:815–822, 1983.

[36] M. R. Franz, P. L. Karasik, C. Li, J. Moubarak, and M. Chavez. Electrical remodeling of the human atrium: similar effects in patients with chronic atrial fibrillation and atrial flutter. *J Am Coll Cardiol*, 30(7):1785–92, Dec 1997.

[37] M. R. Franz, P. L. Karasik, C. Li, J. Moubarak, and M. Chavez. Electrical remodeling of the human atrium: similar effects in patients with chronic atrial fibrillation and atrial flutter. *J Am Coll Cardiol*, 30(7):1785–92, Dec 1997.

[38] J. Freudenberg, T. Schiemann, U. Tiede, and K. H. Höhne. Simulation of cardiac excitation patterns in a three-dimensional anatomical heart atlas. *Computers in Biology and Medicine*, 30:191–203, 2000.

[39] W. H. Gaskell. On the rhythm of the heart of the frog, and on the nature of the action of the vagus nerve. *Phil. Trans R. Soc. London*, 173:993–1033, 1882.

[40] M. Gerhardt, H. Schuster, and J. J. Tyson. Cellular automaton model of excitable media including curvature and dispersion. *Science*, 247:1563–1566, 1990.

[41] L. Glass, M. R. Guevara, and A. Shrier. Universal bifurcations and the classification of cardiac arrhythmias. *Ann. N. Y. Acad. Sci.*, 504:168–178, 1987.

[42] L. Glass, P. Hunter, and A. McCulloch, editors. *Theory of Heart.* Springer-Verlag, New York, 1991.

[43] L. Glass and M. Mackey. *From Clocks to Chaos.* Princeton University Press, Princeton, 1988.

[44] A. Goldbeter. *Biochemical oscillations and cellular rhythms.* Cambridge University Press, Cambridge, 1996.

[45] M. Guevara, A. Ward, A. Shrier, and L. Glass. Electrical alternans and period doubling bifurcations. *IEEE Comp. Cardiol.*, 562:167–170, 1984.

[46] M. R. Guevara, F. Alonso, D. Jeandupeux, and A. C. G. van Ginneken. *Cell to Cell Signalling: From Experiment to Theoretical Models*, chapter Alternans in periodically stimulated isolated ventricular myocytes: Experiment and model, pages 551–563. Academic Press Limited, London, 1989.

[47] M. R. Guevara, G. Ward, A. Shrier, and L. Glass. Electrical alternans and period-doubling bifurcations. In *IEEE Computers in Cardiology*, pages 167–170. IEEE Computer Society, 1984.

[48] G. M. Hall, S. Bahar, and J. Gauthier. Prevalence of rate-dependent bevaviours in cardiac muscle. *Phys Rev Lett*, 82(14):2995–2998, 1999.

[49] K. Hall, D. J. Christini, M. Tremblay, J. J. Collins, L. Glass, and J. Billette. Dynamic control of cardiac alternans. *Phys Rev Lett*, 78:4518–4520, 1997.

[50] A. Hansson, M. Holm, P. Blomstrom, R. Johansson, C. Luhrs, J. Brandt, and S. B. Olsson. Right atrial free wall conduction velocity and degree of anisotropy in patients with stable sinus rhythm studied during open heart surgery. *Eur Heart J*, 19(2):293–300, Feb 1998.

[51] D. Harrild and C. Henriquez. A computer model of normal conductin in the human atria. *Circ Res*, 87:25–36, 2000.

[52] H. Hayashi, R. Lux, R. Wyatt, M. J. Burgess, and J. A. Abildskov. Relation of canine atrial activation sequence to anatomic landmarks. *Am J Physiol*, 242:H421–H428, 1982.

[53] H. Hege, M. Seebaß, D. Stalling, and M. Zöckler. A generalized Marching Cubes Algorithm based on non-binary classifications. *ZIB Preprint*, pages SC 97–05, 1997.

[54] J. Hescheler and R. Speicher. Regular and chaotic behaviour of cardiac cells stimulated at frequencies between 2 and 20 Hz. *Eur Biophys J*, 17:273–280, 1989.

[55] A. L. Hodgkin and A. F. Huxley. Quantitative description of membrane current and its application to conduction and excitation in nerve. *J. Physiol. (Lond.)*, 117:500–544, 1952.

[56] T. J. Hund, J. P. Kucera, N. F. Otani, and Y. Rudy. Ionic charge conservation and long-term steady state in the luo-rudy dynamic cell model. *Biophys J*, 81:3324–3331, 20001.

[57] H. Ito and L. Glass. Spiral breakup in a new model of discrete excitable media. *Phys Rev Lett*, 66:671–674, 1991.

[58] J. Jalife, O. Berenfeld, A. Skanes, and R. Mandapati. Mechanisms of atrial fibrillation: mother rotors or multiple daughter wavelets, or both? *J Cardiovasc Electrophysiol*, 9:S2–S12, 1998.

[59] J. H. Jensen, P. L. Christiansen, and A. C. Scott. Chaos in the Beeler-reuter system for the action potential of ventricular myocardial fibers. *Physica D*, 13:269–277, 1984.

[60] A. A. Kabbara and D. G. Stephenson. Ca^{2+} handling by rat myocardium exposed to ATP solutions of different $[Ca^{2+}]$ and Ca^{2+} buffering capacity. *Am J Physiol*, 273:H1347–1357, 1997.

[61] Kafer. Internodal pathways in the human atria: a model study. *Comput Biomed Res*, 24:549–563, 1991.

[62] W. B. Kannel, R. D. Abbott, D. D. Savage, and P. M. McNamare. Epidemologic features of chronic atrial fibrillation. *New Engl. J. Med.*, 306:1018–1022, 1982.

[63] A. Karma. Spiral breakup in model equations of action potential propagation in cardiac tissue. *Phys Rev Lett*, 71:1103–1106, 1993.

[64] A. Karma, H. Levine, and X. Zou. Theory of pulse instabilities in electrophysiological models of excitable tissues. *Physica D*, 73:113–127, 1994.

[65] R. Khramov. Circulation of a pulse in an excitable medium. *Biofizika*, 23:871–876, 1978. in Russian.

[66] B. S. Kim, Y. H. Kim, G. S. Hwang, H. N. Pak, S. C. Lee, W. J. Shim, D. J. Oh, and Y. M. Ro. Action potential duration restitution kinetics in human atrial fibrillation. *J Am Coll Cardiol*, 39(8):1329–36, Apr 2002.

[67] S. B. Knisley and B. C. Hill. Effects of bipolar point and line stimulation in anisotropic rabbit epicardium: assessment of the critical radius of curvature for longitudinal block. *IEEE Trans Biomed Eng*, 42:957–66, 1995.

[68] K. Krischer, M. Eiswirth, and G. Ertl. Solitary wave phenomena in excitable surface reaction. *Phys Rev Lett*, 69:945–948, 1992.

[69] L. J. Leon and B. M. Horáček. Computer model of excitation and recovery in the anisotropic myocardium. I. rectangular and cubic arrays of excitable elements. *J. Electrocardiol.*, 24:1–16, 1991.

[70] L. J. Leon and B. M. Horáček. Computer model of excitation and recovery in the anisotropic myocardium. II. excitation in the simplified left ventricle. *J. Electrocardiol.*, 24:17–31, 1991.

[71] L. J. Leon and B. M. Horáček. Computer model of excitation and recovery in the anisotropic myocardium. III. arrhythmogenic conditions in the simplified left ventricle. *J. Electrocardiol.*, 24:33–41, 1991.

[72] T. J. Lewis and M. R. Guevara. Chaotic dynamics in an ionic model of the propagated cardiac action potential. *J. Theor. Biol.*, 146:407–432, 1990.

[73] J. L. Lin, L. P. Lai, L. J. Lin, Y. Z. Tseng, W. P. Lien, and S. K. Huang. Electrophysiological determinant for induction of isthmus dependent counterclockwise and clockwise atrial flutter in humans. *Heart*, 81(1):73–81, Jan 1999.

[74] D. S. Lindblad, C. R. Murphey, J. W. Clark, and W. R. Giles. A model of the action potential and underlying membrane currents in a rabbit atrial cell. *Am J Physiol*, 271:H1666–H1696, 1996.

[75] M. Lorange and R. M. Gulrajani. A computer heart model incorporation anisotropic propagation, I: model construction and simulation of normal activation. *J Electrocardiol*, 1993:245–260, 1993.

[76] W. E. Lorensen and H. E. Cline. Marching cubes: A high resolution 3D construction algorithm. *Computer Graphics (Proceedings of SIGGRAPH '87)*, 21(4):163–169, 1987.

[77] C. H. Luo and Y. Rudy. A model of the ventricular cardiac action potential. *Circ Res*, 68:1501–1526, 1991.

[78] C. H. Luo and Y. Rudy. A dynamic model of the cardiac ventricular action potential. I. simulations of ionic currents and concentration changes. *Circ Res*, 74:1071–1096, 1994.

[79] C. H. Luo and Y. Rudy. A dynamic model of the cardiac ventricular action potential II. *Circ Res*, 74:1097–1113, 1994.

[80] E. Macchi. Digital-computer simulation of the atrial electrical excitation cycle in man. *Adv Cardiol*, 10:102–110, 1974.

[81] J.-L. Martiel and A. Goldbeter. A model based n receptor desensitization for cyclic amp signaling in dictyostelium cells. *Biophys J*, 52:807–828, 1987.

[82] R. E. McAllister, D. Noble, and R. W. Tsien. Reconstruction of the electrical activity of cardiac Purkinje fibers. *J Physiol (Lond.)*, 251:1–59, 1975.

[83] A. D. McCulloch, B. H. Smaill, and P. J. Hunter. Left ventricular epicardial deformation in the isolated arrested dog heart. *Am J Physiol*, 252:H233–H241, 1987.

[84] A. D. McCulloch, B. H. Smaill, and P. J. Hunter. Regional left ventricular epicardial deformation in the passive dog heart. *Circulation*, 64:721–733, 1989.

[85] A. S. Mikhailov. *Foundations of Synergetics I.* Springer Series in Synergetics. Springer-Verlag, 1990.

[86] A. S. Mikhailov. *Foundations of Synergetics II.* Springer Series in Synergetics. Springer-Verlag Berlin, 2nd edition, 1996.

[87] G. Moe, W. Reinhold, and J. Abildskov. A computer model of atrial fibrillation. *Am. Heart. J.*, 67:200–220, 1964.

[88] J. Morgan, D. Cunninggham, and E. Rowland. Electrical restitution in the endocardium of the intact human right ventricle. *Br. Heart J.*, 67:42–46, 1992.

[89] C. F. Murphy, S. M. Horner, D. J. Dick, B. Coen, and M. J. Lab. Electrical alternans and the onset of rate-induced pulsus alternans during acute regional ischemia in the anaesthetised pig heart. *Cardiovascular Research*, 32:138–147, 1996.

[90] R. J. Myerburg, R. Mitrani, A. I. Jr, A. L. Bassett, J. Simmons, and A. Castellanos. *Cardiac Electrophysiology, from cell to bedside.* W. B. Saunders, Philadelphia, 3rd edition, 2000.

[91] J. S. Nagumo, S. Arimoto, and S. Yoshizawa. An active pulse transmission line simulating nerve axon. *Proc IRE*, 50:2061–2071, 1962.

[92] S. Nattel and D. Li. Ionic remodeling in the heart: pathophysiological significance and new therapeutic opportunities for atrial fibrillation. *Circ Res*, 87(6):440–447, Sep 2000.

[93] D. Noble, A. Varghese, P. Kohl, and P. Noble. Improved guinea-pig ventricular cell model incorporating a diadic space, I_{K_r} and I_k, and length- and tension-dependent processes. *Can. J. Cardiol.*, 1:123–134, 1998.

[94] J. Nolasco and R. Dahlen. A graphic method for the study of alternation in cardiac action potentials. *Am J Physiol*, 25:191–196, 1968.

[95] A. Nygren, C. Fiset, L. Firek, J. W. Clark, D. S. Lindblad, R. B. Clark, and W. R. Giles. Mathematical model of an adult human atrial cell: the role of K^+ currents in repolarization. *Circ Res*, 82:63–81, 1998.

[96] A. Panfilov and J. Keener. Re-entry in an anatomical model of the heart. *Chaos, Solitons and Fractals*, 5(3-4):681–689, 1995.

[97] A. V. Panfilov. Spiral breakup as a model of ventricular fibrillation. *Chaos*, 8:57–64, 1998.

[98] A. V. Panfilov and P. Hogeweg. Spiral break-up in a modified FitzHugh−Nagumo model. *Phys Lett A*, 176:295–299, 1993.

[99] A. V. Panfilov and A. V. Holden. Self-generation of turbulent vortices in a two-dimensional model of cardiac tissue. *Phys Lett A*, 147:463–466, 1990.

[100] A. V. Panfilov and A. V. Holden, editors. *Computational biology of the heart*. John Wiley & Sons, Chichester, 1997.

[101] A. V. Panfilov and J. P. Keener. Dynamics of dissipative structures in reaction-diffusion equations. *SIAM J. App Math*, 55:205–219, 1995.

[102] A. V. Panfilov and A. M. Pertsov. Vortex ring in three-dimensional active medium in reaction-diffusion system. *Doklady AN SSSR*, 274:1500–1503, 1984. In Russian.

[103] A. M. Pertsov, J. M. Davidenko, R. Salomontsz, W. Baxter, and J. Jalife. Spiral waves of excitation underlie reentrant activity in isolated cardiac muscle. *Circ Res*, 72:631–650, 1993.

[104] C. S. Peskin. Numerical analysis of blood flow in the heart. *J. Comp. Phys*, 25:220–252, 1977.

[105] C. S. Peskin. Cardiac fluid dynamics. *Crit. Rev. Biomed Eng*, 20:451–459, 1992.

[106] W. H. Press, F. B. P., S. A. Teukolsky, and W. T. Vetterling. *Numerical recipes in C*. Cambridge University Press, Cambridge, New York, Port Chester, Melbourne, Sydney, 1992.

[107] L. Priebe and D. J. Beuckelmann. Simulation study of cellular electric properties in heart failure. *Circ Res*, 82:1206–1223, 1998.

[108] A. Pumir and V. Krinsky. Unpinning of a rotating wave in cardiac muscle by an electric field. *J. Theor. Biol.*, 199:311–319, 1999.

[109] Z. Qu, J. Weiss, and A. Garfinkel. Spatiotemporal chaos in a simulated ring of cardiac cells. *Phys Rev Lett*, 78:1387–1390, 1997.

[110] Z. Qu, J. Weiss, and A. Garfinkel. Cardiac electrical restitution properties and stability of reentrant spiral waves: a simulation study. *Am. J. Physiol.*, 276:H269–H283, 1999.

[111] M. Riccio, M. Koller, and R. Gilmour Jr. Electrical restitution and spatiotemporal organization during ventricular fibrillation. *Circ Res*, 84:955–963, 1999.

[112] D. S. Rosenbaum, L. E. Jackson, J. M. Smith, H. Garan, J. N. Ruskin, and R. J. Cohen. Electrical alternans and vulnerability to ventricular arrhythmias. *New Engl. J. Med.*, 330:235–241, 1994.

[113] J. E. Saffitz and K. J. Yamada. *Cardiac Electrophysiology*, chapter Gap junction distribution in the heart. W. B. Saunders, 3rd edition, 2000.

[114] R. F. Schmidt and G. Thews. *Human physiology.* Springer-Verlag, 1989.

[115] S.Rush and H. Larsen. A practical algorithm for solving dynamic membrane equations. *IEEE Trans Biomed Eng*, 25:389–392, 1978.

[116] J. F. Thomson and N. Weatherill, editors. *Handbook of Grid Generation.* CRC Press, 1999.

[117] A. Varghese and G. R. Sell. A conservation principle and its effect on the formulation of Na-Ca exchanger current in cardiac cells. *J. Theor. Biol.*, 189:33–40, 1997.

[118] A. Vinet, D. R. Chialvo, C. Michaelis, and J. Jalife. Nonlinear dynamics of rate-dependent activation in models of cardiac cells. *Circ Res*, 67:1510–1524, 1990.

[119] A. Vinet and F. A. Roberge. Excitability and repolarization in an ionic model of the cardiac cell membrane. *J. Theor. Biol.*, 170(2):183–199, 1994.

[120] J. von Neumann. *Theory of Self-Reproducing Automata.* University of Illinois Press, Champain, 1966.

[121] R. K. P. Wach and F. Dienstl. Three-dimensional computer model of the entire human heart for simulation of reentry and tachycardia: gap phenomenon and Wolff-Parkinson-White syndrome. *Basic Res Cardiol*, 86:485–501, 1991.

[122] Z. G. Wang, L. C. Pelletier, M. Talajic, and S. Nattel. Effects of flecainide and quinidine on human atrial action potentials: role of rate dependence and comparison with guinea pig, rabbit, and dog tissues. *Circulation*, 82:274–283, 1990.

[123] D. Wei, G. Yamada, T. Musha, H. Tsunakawa, T. Tsutsumi, and K. Harumi. Computer simulation of supraventricular tachycardia with the WPW syndrome using three dimensional heart models. *J. Electrocardiol.*, 23:261–273, 1990.

[124] J. Weiss, A. Garfinkel, H. Karagueuzian, Z. Qu, and P. Chen. Chaos and transition to ventricular fibrillation. *Circulation*, 99:2819–2826, 1999.

[125] K. Wenckebach. Zur Analyse des unregelmäßigen Pulses. II über den regelmäßig intermittierenden Puls. *Z. Klin. Med.*, 37:475–488, 1899.

[126] M. C. Wijffels, C. J. Kirchhof, R. Dorland, and M. A. Allessie. Atrial fibrillation begets atrial fibrillation. a study in awake chronically instrumented goats. *Circulation*, 92:1954–1968, 1995.

[127] A. T. Winfree. Spiral waves of chemical activity. *Science*, 175:634–636, 1972.

[128] A. T. Winfree. Rotating chemical reactions. *Scientific American*, 230:82–95, 1974.

[129] A. T. Winfree. *When Time Breaks Down.* Princeton University Press, Princeton, 1987.

[130] A. T. Winfree. Varieties of spiral wave behavior: An experimental approach to the theory of excitable media. *Chaos*, 1:303–334, 1990.

[131] A. T. Winfree. On measuring curvature and electrical diffusion coefficients in anisotropic myocardium: comments on "Effects of bipolar point and line simulation in anisotropic rabbit epicardium: assessment of the critical radius of curvature for longitudinal block". *IEEE Trans Biomed Eng*, 43:1200–1204, 1996.

[132] A. T. Winfree and S. H. Strogatz. Organizing centers for three-dimensional chemical waves. *Nature*, 311:611–615, 1984.

[133] T. J. Wu, M. Yashima, F. Xie, C. A. Athill, Y. H. Kim, M. C. Fishbein, Z. Qu, A. Garfinkel, J. N. Weiss, H. S. Karagueuzian, and P. S. Chen. Role of pectinate muscle bundles in the generation and maintenance of intra-atrial reentry: potential implications for the mechanism of conversion between atrial fibrillation and atrial flutter. *Circ Res*, 83(4):448–62, Aug 1998.

[134] F. Xie, Z. Qu, A. Garfinkel, and J. N. Weiss. Electrical refractory period restitution and spiral wave reentry in simulated cardiac tissue. *Am J Physiol Heart Circ Physiol*, 283(1):H448–60, Jul 2002.

[135] A. R. Yehia, D. Jeandupeux, F. Alonso, and M. R. Guevara. Hysteresis and bistability in the direct transition from 1:1 to 2:1 rhythm in periodically driven ventricular cells. *Chaos*, 9:916–931, 1999.

[136] J. Zeng and Y. Rudy. Early afterdeolarizations in cardiac myocytes: mechanisms and rate dependence. *Biophys J*, 68:68, 949-964.

[137] A. I. Zhabotinsky. Concentration self-oscillations. *Nauka*, 1974.

[138] V. S. Zykov. *Simulation of wave processes in Excitable Media.* Manchester University Press, 1987.

[139] V. S. Zykov and A. S. Mikhailov. Rotating spiral wavels in a simple model of excitable medium. *Sov.Phys Dokl.*, 31:51–55, 1986.

Curriculum vitae

1972	Born in Hamburg, Germany
1988-1989	Exchange student in Waldorf, Maryland
1991	Graduated from Christianeum High School in Hamburg, Germany
1991	1st prize in the German National Math Contest; study grant of the German Study Foundation “Studienstiftung” as award
1991-1992	Civilian service as paramedic
1992-1994	Basic undergraduate Studies in Mathematics and Physics at the Technical University in Berlin
1994-1995	Abroad studies at the ETH Zurich (Switzerland), Mathematics and Physics
1995	Summer student at the German Electron Synchroton (DESY) at Hamburg, Germany
1995-1997	Advanced undergraduate Studies in Theoretical Physics at the Technical University Berlin
1995-1996	Tutor for experimental physics at the Technical University Berlin
1996	Tutor for theoretical physics at the Technical University Berlin
1997-1998	Wrote diploma thesis at the Institute for Theoretical Biology, Humboldt University Berlin
1998	Diploma in Physics from the Technical University in Berlin
1998	Heraeus-Award for successful and fast completion of diploma studies
1998 - 2001	PhD student at the Humboldt-University Berlin / Utrecht University (Netherlands)
Nov 1998 - May 1999	Research visit to Prof. Panfilov, Utrecht, Netherlands
Mar 2000	Research visit to Prof. Keener, Salt Lake City, Utah
Mar 2002	Begin of postdoctoral studies at the State University of New York, Syracuse, Department of Pharmacology
Jun 2002	Graduated as PhD in Theoretical Physics at the Humboldt University Berlin

Selbständigkeitserklärung

Hiermit erkläre ich, die vorliegende Arbeit selbständig ohne fremde Hilfe verfasst zu haben und nur die angegebene Literatur und Hilfsmittel verwendet zu haben.

Christian Zemlin
27. Februar 2002